

Integer quantum Hall effect

Hideo Aoki

Department of Physics, University of Tokyo, Hongo, Tokyo 113-0033, Japan

Abstract

Integer quantum Hall effect, which is the Hall effect quantized into integer times e^2/h (e : elementary charge, h : Planck's constant) observed first in two-dimensional electron gases in strong magnetic fields, is reviewed from both theoretical and experimental standpoints. Basic physics underlying the phenomenon is explained. Specifically in this new edition we have a fresh look at how the quantum Hall effect is captured in a perspective of topological systems, since, while the quantum Hall effect is historically the first realization of the topological systems, the field has been delved into a much wider realm of physics of topological systems. We also mention diverse advances such as the quantum Hall effect (QHE) in various materials and contexts that include graphene, oxides and narrow-gap semiconductors, a relation with the fractional quantum Hall effect, and the quantum Hall effect as the resistance standard and further roles in the new SI system. We also expound the Floquet topological insulator (a light-matter coupled system) as a new paradigm in nonequilibrium topological systems, where an anomalous quantum Hall effect in zero magnetic field is realized as theoretically predicted to occur in graphene illuminated by a circularly-polarized laser and experimentally verified recently.

Key Points

- Quantum Hall effect (QHE) viewed in a perspective of topological systems,
- QHE in graphene systems including the twisted bilayer graphene,
- QHE as the resistance standard and further roles now incorporated in the new SI system,
- Relation of the integer QHE with the fractional quantum Hall effect,
- The Floquet topological insulator as a prototype of nonequilibrium topological systems.

1 Classification of topological systems by generic symmetries

Recent years have witnessed a vast widening of physics of topological systems, where IQHE is still enjoying the status of the very first one recognised. So it will be instructive to start the article with a perspective of the topological systems in terms of the classification scheme of the entire topological systems.[1] Let us first show the full classification table in Fig.1. There are altogether ten universality classes for topological quantum states, and examples are indicated in the figure.

The starting point is the essential symmetries in classifying topological systems:

- Time-reversal symmetry (TRS; operator $\equiv \Theta$).

		T-reversal Θ^2	Particle-hole Ξ^2	Chiral $\Xi\Theta$	spatial dimension		
					$d=1$	$d=2$	$d=3$
Standard (Wigner-Dyson)	A (unitary)	x	x	x	IQHE; Haldane model	Z	--
	AI (orthogonal)	+1	x	x	--	--	--
	AII (symplectic)	-1	x	x	QSHE; Kane-Mele	Z_2	Z_2 Z_2 TI
Chiral	AIII (chiral unitary)	x	x	1	Z	--	Z
	BDI (chiral orthogonal)	+1	+1	1	Z	--	--
	CII (chiral symplectic)	-1	-1	1	2Z	--	Z_2
BdG (SC)	D (p-wave SC)	x	+1	x	p SC Z_2	Z spinless p+ip SC	--
	C (d-wave SC)	x	-1	x	--	$2Z$ d+id SC	--
	DIII (p-wave TRS SC)	-1	+1	1	Z_2	Z_2	Z $^3\text{He-B}$
	CI (d-wave TRS SC)	+1	-1	1	--	--	(BW state); $2Z$ UTe_2

Figure 1: Table of topological systems. For the meaning of "x, +1, -1", see text. For spatial dimensions $d = 1, 2, 3$, topological numbers are indicated with symbols Z : integers, Z_2 : binary (-1,+1). After A.P. Schnyder, S. Ryu, A. Furusaki, and A.W.W. Ludwig, Phys. Rev. B **78**, 195125 (2008); S. Ryu et al, New J. Phys. **12**, 065010 (2010). Added red inscriptions denote examples of the quantum states and materials.

- Charge-conjugation (\sim particle-hole) symmetry (PHS; operator $\equiv \Xi$).

These can be expressed as eigenvalues of (anti-unitary) operators,

$$KU$$

for a given Hamiltonian, where K : complex conjugation, U : unitary rotation. For instance, $\Theta = K$ for class AI, $\Xi = -i\sigma_y K$ for AII. If each of the symmetries is

$$\text{absent} \rightarrow \text{"x" in the table,} \quad (1)$$

$$\text{present} \rightarrow \text{" + 1" if (operator)}^2 = \text{identity} \quad (2)$$

$$\text{" - 1" if (operator)}^2 = -\text{identity.} \quad (3)$$

So we have (3 possibilities for TRS) \otimes (3 possibilities for PHS), i.e., 9 possible cases. We can also consider a product TRS \otimes PHS (where an operator $\Theta\Xi$ represents the chiral symmetry). When (TRS, PHS) = (x, x), $\Theta\Xi$ can be either present ($\Theta\Xi = 1$) or absent ($\Theta\Xi = x$). Thus we end up with 10 cases in total. The quantum Hall effect belongs to Class A (unitary), with the time-reversal symmetry broken by an external magnetic field.

The table can be obtained mathematically in terms of Clifford algebra and dimensional reduction. Along this line, we can rearrange the table as in Fig.2, where TI and SC states appear in a bunched structure.

	d				
	1	2	3	4	...
$\Theta^2=x, \Xi^2=x$: <i>Complex case</i>					
A	0	\mathbb{Z}	0	\mathbb{Z}	...
AIII	\mathbb{Z}	0	\mathbb{Z}	0	...
otherwise: <i>Real case</i>					
AI	0	0	0	$2\mathbb{Z}$...
BDI	\mathbb{Z}	0	0	0	...
D	\mathbb{Z}_2	\mathbb{Z}	0	0	...
DIII	\mathbb{Z}_2	\mathbb{Z}_2	\mathbb{Z}	0	...
AII	\mathbb{Z}_2	\mathbb{Z}_2	\mathbb{Z}_2	\mathbb{Z}	...
CII	$2\mathbb{Z}$	0	\mathbb{Z}_2	\mathbb{Z}_2	...
C	0	$2\mathbb{Z}$	0	\mathbb{Z}_2	...
CI	0	0	$2\mathbb{Z}$	0	...

Figure 2: Another representation of the table of topological systems, after A.P. Schnyder, S. Ryu, A. Furusaki, and A.W.W. Ludwig, Phys. Rev. B **78**, 195125 (2008); S. Ryu et al, New J. Phys. **12**, 065010 (2010). Purple bands highlight TI (topological insulator) and SC (superconductor) series, orange squares ($\mathbb{Z}_2, \mathbb{Z}_2, \mathbb{Z}$) triplets, while red inscriptions denote examples of the quantum states as in the previous figure.

In subsection 'Bulk-edge correspondence' below, we shall describe the edge states beginning with the QHE system. This notion can be extended to the general topological states as described above, which is natural since the boundary states are generic in the field-theoretic picture. Figure 3 summarises, for later references, topological boundary states for various topological states on the table of topological systems.

2 QHE — Introduction

Quantum Hall effect (QHE) is undoubtedly one of the most fascinating and important phenomena not only in the condensed-matter physics, but more generally in a wider scope of physics that encompasses cold-atom systems and a multitude of topological systems on one hand, and in field theoretic aspects on the other. This can be immediately realised if one notes a vast spectrum of the quantum Hall physics ranging from fundamental physics (topology in terms of the quantum field theory) down to applicational physics as exemplified by the QHE as the resistance standard. To start with, QHE originated from quantum mechanical physics in two spatial dimensions (2D) as opposed to the three-dimensional space in which electrons usually dwell. Surprisingly, 2D is a special dimension which accommodates phenomena specific to 2D, as field theories actually note that even spatial dimensions are rather special. QHE stands out as a most remarkable one. In this sense 2D is definitely not just a reduced dimensionality. This accounts for the remarkable width and depth of the physics of QHE, which has now become as large a field as those for superconductivity/superfluidity. Interestingly, the QHE physics even

	Θ^2	Ξ^2	$\Xi\Theta$	spatial dimension			Boundary states
				$d=1$	$d=2$	$d=3$	
A	x	x	x	--	\mathbb{Z} (circled)	IQHE	2D, TR broken bulk: \mathbb{Z} (1st Chern #) boundary: 1D chiral edge states
AI	+1	x	x	--	--	--	
AII	-1	x	x	--	QSHE; Kane-Mele; \mathbb{Z}_2 (circled)	\mathbb{Z}	2D, TR invariant bulk: \mathbb{Z}_2 boundary: 1D helical edge states
AIII	x	x	1	\mathbb{Z}	--	\mathbb{Z}	
BDI	+1	+1	1	\mathbb{Z} (circled)	SSH; Creutz	--	1D, TR invariant bulk: \mathbb{Z} boundary: 0D edge states
CII	-1	-1	1	$2\mathbb{Z}$	--	\mathbb{Z}_2	
D	x	+1	x	\mathbb{Z}_2	\mathbb{Z} (circled)	p+ip-SC	2D, TR broken bulk: \mathbb{Z} (1st Chern #) boundary: 1D chiral edge states
C	x	-1	x	--	$2\mathbb{Z}$	d+id SC	
DIII	-1	+1	1	\mathbb{Z}_2	\mathbb{Z}_2	\mathbb{Z} (circled)	3D, TR invariant bulk: \mathbb{Z} boundary: 2D surface states
CI	+1	-1	1	--	${}^3\text{He-B}; \text{UTe}_2$	$2\mathbb{Z}$	

Figure 3: Topological boundary states for various topological states on the table of topological systems. TR stands for the time-reversal symmetry.

has spinoffs into topological superconductivity, QHE in higher (three) dimensions, etc.

QHE consists basically of the integer QHE discovered in 1980, which is essentially a one-body problem (but see section ‘Integer vs fractional quantum Hall effects’), and the subsequent fractional QHE discovered in 1983, which is a many-body effect. In this chapter we focus on the integer QHE. Even so, the field is so vast that here we shall describe bare essentials. (For details, see, e.g., [2, 3, 4, 5, 6, 7]).

If we just summarise the peculiar properties of the QHE system,

1. Energy spectrum: completely discrete, line spectrum (i.e., Landau levels) arises in the clean limit. This is most unusual, since the system is a bulk. This gives a starting point for the integer QHE. When an integer number of Landau levels are fully filled, then we can regard the system as a giant “closed shell” of electrons.
2. Transport properties: the closed shell is not an ordinary one, since the quantised Hall conductivity (integer times e^2/h) is given entirely in terms of physical constants (e : elementary charge, h : Planck’s constant).

One essential feature of the system is that the position coordinates, x and y , in real space become noncommutative operators. In other words, an applied magnetic field makes the position coordinates \mathbf{r} mixed with the wavenumber \mathbf{k} . On top of this, there is a fortuitous coincidence of the Hall conductivity with a topological invariant.

2.1 Two-dimensional electron gas

As a background we should start with describing the two-dimensional electron gas (2DEG). The usual electron gas is a system of electrons that move more or less freely in a 3D space, as typically realised in simple metals. In semiconductor physics we can realise 2D electron gas in metal-oxide-semiconductor field-effect transistors (MOSFET's; Fig.4(a)) mainly before ca 1970's, and subsequently QHE is observed primarily in semiconductor heterostructures (Fig.4(b))[8].

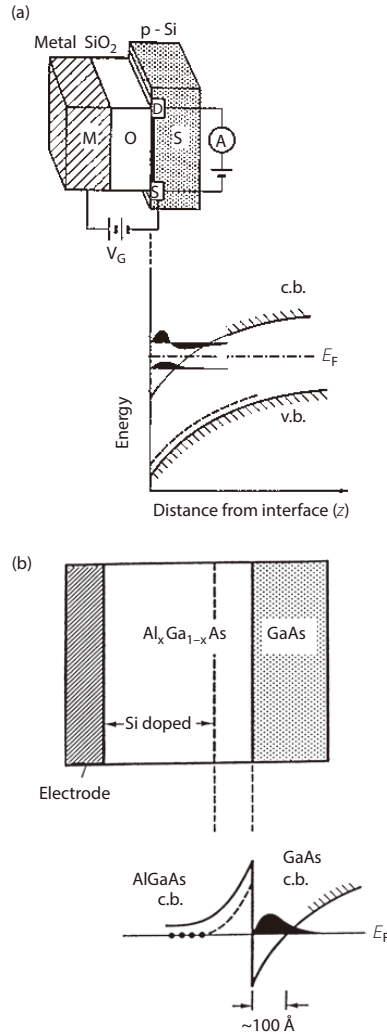


Figure 4: Structures of MOSFET (a) and semiconductor heterostructure (b). In each frame, the upper panel shows the sample structure, while the lower panel the electronic band structure around the interface. Typical wavefunctions are plotted in black against the direction perpendicular to the interface.

In these structures, electrons are confined to a 2D plane, due to a Schottky barrier between the metal and the oxide in an MOSFET, or between different semiconductors in a heterostructure. There, an electron moves in the 2D interface, with the electronic structure of the constituent materials entering only through the effective mass in the effective-mass approximation.

The wavefunction has a finite thickness in the direction perpendicular to the plane, but the motion along this direction is quantised, so that the band structure comprises 2D electronic bands labelled by the quantised levels in the normal direction, which are called subbands. When only the lowest subband is occupied by electrons (or, more precisely, if the transitions between adjacent subbands can be neglected), we can regard the motion genuinely 2D. The Schrödinger equation reads

$$\mathcal{H}\psi = \left[\frac{1}{2m^*} p^2 + U(z) \right] \psi = E\psi, \quad (4)$$

where m^* is the effective mass of the electron, \mathbf{p} is the momentum in the 2D plane along $\mathbf{r} \equiv (x, y)$, and $U(z)$ is the confining (Schottky) potential. If we ignore disorder (interface roughness, impurities, etc), the wavefunction is expressed as

$$\psi = \exp[i(k_x x + k_y y)] f_n(z) \quad (5)$$

up to a normalisation constant, where the 2D motion is described by plane waves with wavenumber $\mathbf{k} \equiv (k_x, k_y)$ and f_n is the n -th quantised wavefunction along z .

In semiconductor heterostructures, typically GaAs/AlGaAs grown with the molecular beam epitaxy (MBE), the Fermi energy is $E_F \sim 10$ meV, so that the electron system is a degenerate Fermi gas at liquid He temperature (~ 0.4 meV).

2.2 2DEG in strong magnetic fields — Classical mechanics

If we apply an external magnetic field, \mathbf{B} , normal to a 2DEG, classically an electron undergoes a circular motion (called Larmor's motion) due to the Lorentz force, $-e\mathbf{v} \times \mathbf{B}$ (e : elementary charge, \mathbf{v} : velocity of the electron). When there is an external electric field, \mathbf{E} , as well, the classical orbit is a trochoid (Fig.5(a)), where the centre of the circular motion drifts in a direction perpendicular to \mathbf{E} with a drift velocity $c\mathbf{E} \times \mathbf{B}/B^2$ (c : speed of light).

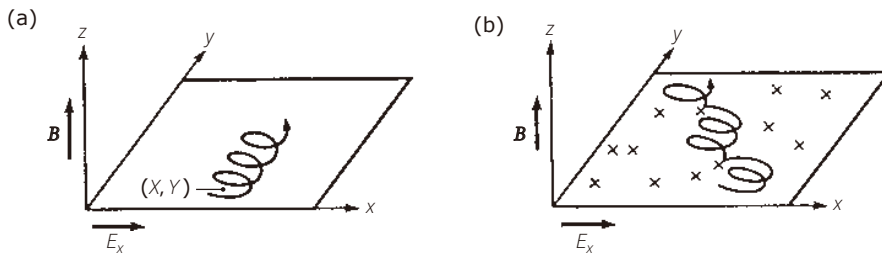


Figure 5: Classical orbits for a charged particle in a magnetic field ($\parallel z$) in an applied electric field ($\parallel x$) for a clean system (a) and in a disordered system with scatterers (crosses) (b).

This is because the electron is accelerated (decelerated) when it moves along (against) \mathbf{E} , while the Lorentz force ($\propto v$) is always balanced with the centrifugal force (\propto the radius of the circular motion), so that the circular trajectory is elongated in the accelerated part while contracted in the decelerated part. The resulting drift of the centre coordinate accounts for the classical Hall effect.

When the system is disordered, due to e.g. impurities, then an electron is scattered, and the drift velocity acquires a component along \mathbf{E} (Fig.5(b)). If we define the conductivity, the

quantity becomes a tensor in the presence of a magnetic field, where the current, \mathbf{j} , and \mathbf{E} are related as

$$\begin{pmatrix} j_x \\ j_y \end{pmatrix} = \begin{pmatrix} \sigma_{xx} & \sigma_{xy} \\ \sigma_{yx} & \sigma_{yy} \end{pmatrix} \begin{pmatrix} E_x \\ E_y \end{pmatrix},$$

$$\begin{pmatrix} E_x \\ E_y \end{pmatrix} = \begin{pmatrix} \rho_{xx} & \rho_{xy} \\ \rho_{yx} & \rho_{yy} \end{pmatrix} \begin{pmatrix} j_x \\ j_y \end{pmatrix}. \quad (6)$$

Here $\sigma_{\mu\nu}$ is the conductivity tensor and $\rho_{\mu\nu}$ the resistivity tensor. They are inverse matrices with each other, so that we have, with a symmetry $\sigma_{xx} = \sigma_{yy}$, $\sigma_{yx} = -\sigma_{xy}$,

$$\begin{pmatrix} \rho_{xx} & \rho_{xy} \\ \rho_{yx} & \rho_{yy} \end{pmatrix} = \begin{pmatrix} \sigma_{xx} & \sigma_{xy} \\ -\sigma_{xy} & \sigma_{xx} \end{pmatrix}^{-1} = \frac{1}{\sigma_{xx}^2 + \sigma_{xy}^2} \begin{pmatrix} \sigma_{xx} & -\sigma_{xy} \\ \sigma_{xy} & \sigma_{xx} \end{pmatrix},$$

$$\begin{pmatrix} \sigma_{xx} & \sigma_{xy} \\ \sigma_{yx} & \sigma_{yy} \end{pmatrix} = \frac{1}{\rho_{xx}^2 + \rho_{xy}^2} \begin{pmatrix} \rho_{xx} & -\rho_{xy} \\ \rho_{xy} & \rho_{xx} \end{pmatrix}. \quad (7)$$

If we introduce a phenomenological relaxation time, τ_0 , in zero magnetic field to describe the scattering in a classical transport theory with the equation of motion given by $m^*(d/dt + 1/\tau_0)\mathbf{v} = -e(\mathbf{E} + \mathbf{v} \times \mathbf{B})$, then we have

$$\begin{aligned} \sigma_{xx} &= \frac{\sigma_0}{1 + \omega_c^2 \tau_0^2}, \\ \sigma_{xy} &= \frac{\sigma_0 \omega_c \tau_0}{1 + \omega_c^2 \tau_0^2} = -\frac{nec}{B} + \frac{\sigma_{xx}}{\omega_c \tau_0}, \end{aligned} \quad (8)$$

where $\sigma_0 = ne^2\tau_0/m^*$ is the conductivity in zero magnetic field, and

$$\omega_c = eB/m^*c$$

is the cyclotron frequency. When $\omega_c\tau_0 \gg 1$ (for which an electron can accomplish the Larmor motion between scattering events), the leading term, $\sigma_{xy} \simeq -nec/B$, on the right-hand side of eqn(8) is the main term (the classical Hall conductivity in the clean case), while the second term a small correction. Thus we have a voltage (Hall voltage) in the direction perpendicular to the electric field when the sample has open boundaries in that direction, or we can measure the Hall current if electrodes are attached. Figure 6 depicts the sample geometry.

2.3 2DEG in strong magnetic fields — Quantum mechanics

If we go to quantum mechanics, an electron is still subject to a circular motion within the correspondence principle, but now with a quantum mechanical uncertainty. We should start from a Hamiltonian,

$$\mathcal{H}_0 = \frac{1}{2m^*}\boldsymbol{\pi}^2, \quad (9)$$

where the momentum \mathbf{p} is now an operator, which is replaced, in a magnetic field $\mathbf{B} = \text{rot}\mathbf{A}$, with the canonical momentum $\boldsymbol{\pi} = \mathbf{p} + (e/c)\mathbf{A}(\mathbf{r})$ with \mathbf{A} being the vector potential.

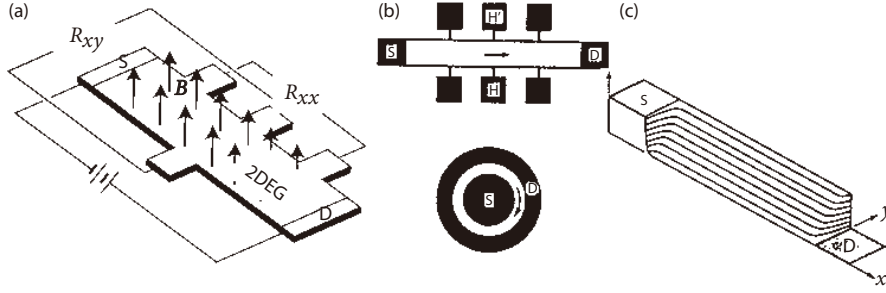


Figure 6: (a) Hall-bar sample geometry for measuring the QHE. (b) Top views of a Hall bar and a Corbino sample, with source (S) and drain (D) electrodes. (c) A birds-eye view of the equipotential lines in the QHE condition.

It is convenient to decompose the cyclotron motion into the centre $\mathbf{R} \equiv (X, Y)$ of the circular motion (“guiding centre”) and the relative coordinate $\boldsymbol{\xi} \equiv (\xi, \eta)$ to facilitate applying the correspondence principle. The relative coordinate is related to the velocity as $\mathbf{v} = \omega_c \hat{\mathbf{e}}_z \times \boldsymbol{\xi}$ with $\hat{\mathbf{e}}_z$ a unit vector normal to the 2D plane. The presence of a magnetic field thus renders a skew (i.e., vector-product) relation between $\boldsymbol{\xi}$ and \mathbf{v} .

The quantum mechanical expression for the velocity is $\mathbf{v} = (i/\hbar) [\mathcal{H}_0, \mathbf{r}] = \boldsymbol{\pi}/m^*$, which means that we have $\boldsymbol{\xi} = -(c/eB)\hat{\mathbf{e}}_z \times \boldsymbol{\pi}$, i.e.,

$$(\xi, \eta) = \frac{\ell^2}{\hbar} (\pi_y, -\pi_x). \quad (10)$$

Here

$$\ell \equiv \sqrt{\frac{c\hbar}{eB}} \quad (11)$$

is the length scale of the cyclotron motion, called the magnetic length, which does not depend on material parameters and has a typical value of 81 Å for the magnetic field of 10 T.

Thus the relative coordinate, (ξ, η) , is a quantum mechanical operator, which in turn implies the centre coordinate, $(X, Y) = (x - (\ell^2/\hbar)\pi_y, y + (\ell^2/\hbar)\pi_x)$, is a quantum mechanical operator as well. From the standard commutation relation, $[x, p_x] = [y, p_y] = i\hbar$, we obtain commutation relations,

$$[\xi, \eta] = -i\ell^2, \quad [X, Y] = i\ell^2, \quad (12)$$

namely, x coordinate does not commute with y coordinate, which implies that the relative coordinates have an uncertainty $\sim \ell$. The same applies to the centre coordinate. This is unusual, since ordinarily it is the momentum with which the real-space coordinate does not commute.

Quantum mechanical states can be derived algebraically. For this we first note that the commutation relations for (X, Y) and (ξ, η) enable us to introduce two sets of harmonic-oscillator (boson) operators,

$$\begin{aligned} a &= \frac{\ell}{\sqrt{2\hbar}} (\pi_x - i\pi_y) = -\frac{1}{\sqrt{2}\ell} (\eta + i\xi), \\ b &= \frac{1}{\sqrt{2}\ell} (X + iY), \end{aligned} \quad (13)$$

which have bosonic commutation relations,

$$[a, a^\dagger] = [b, b^\dagger] = 1. \quad (14)$$

Then the one-particle Hamiltonian, \mathcal{H}_0 for the clean system which is quadratic in $\boldsymbol{\pi}$, can be expressed as

$$\mathcal{H}_0 = \hbar\omega_c \left(a^\dagger a + \frac{1}{2} \right) \quad (15)$$

in terms of the operator a alone, which is natural since b involving (X, Y) should not appear in a translationally invariant system. Since the Hamiltonian has the same form as a linear harmonic oscillator, the energy eigenvalues are

$$E_N = \hbar\omega_c \left(N + \frac{1}{2} \right), \quad (N = 0, 1, 2, \dots) \quad (16)$$

where N is called the Landau index.

So we have here a truly abnormal situation where the energy spectrum, despite the system being a bulk, is completely discrete (Fig.7(a)). In three-dimensional systems we do have Landau's quantisation, but the extra motion along \mathbf{B} makes the density of states a continuum (Fig.7(a)). In 2D each level, called the Landau level as labelled by Landau index, has then a macroscopic degeneracy. The degeneracy, n_ϕ , can be estimated by noting that the density of states of a 2DEG, which is a constant, $D(E) = m^*/2\pi\hbar^2$ per unit area, integrated over an interval $\hbar\omega_c$ should correspond to the degeneracy per unit area,

$$n_\phi = \hbar\omega_c D(E) = 1/(2\pi\ell^2). \quad (17)$$

This number can be expressed as

$$n_\phi = B/\phi_0, \quad (18)$$

where $\phi_0 \equiv ch/e = 4 \times 10^{-7} \text{ G} \cdot \text{cm}^2$ is the flux quantum, so that n_ϕ amounts to the number of flux quanta penetrating the unit area. Alternatively, we can say that the total degeneracy, $S/2\pi\ell^2$, is of the order of the number of cyclotron orbits that cover the sample area S .

We can more precisely realise this in terms of the wavefunctions. We first note that the operator b is related with the orbit centre as $X^2 + Y^2 = 2\ell^2 \left(b^\dagger b + \frac{1}{2} \right)$. The formulation so far does not depend on the gauge (i.e., how we fix the vector potential \mathbf{A} which has an ambiguity related with the gauge transformation). The wavefunction does depend on the gauge. Let us adopt the symmetric gauge, $\mathbf{A} = \frac{1}{2} \mathbf{B} \times \mathbf{r}$. This amounts to taking, out of the degenerate wavefunctions, the set that diagonalise, simultaneously with the energy, the angular momentum, $\hat{\mathbf{L}} = \mathbf{r} \times \mathbf{p}$, which points to z when the motion is within the (x, y) plane. We can show that

$$L_z = [\mathbf{r} \times (\boldsymbol{\pi} - (e/c)\mathbf{A})]_z = a^\dagger a - b^\dagger b \quad (19)$$

with $\hbar = 1$. For the lowest $N = 0$ Landau level we have a harmonic-oscillator form for $\hat{L}_z = -b^\dagger b$, so that the eigenfunction having the eigenvalue of $L_z = -m$ is given by

$$|m\rangle = \frac{(b^\dagger)^m}{\sqrt{m!}} |0\rangle \quad (m = 0, 1, 2, \dots),$$

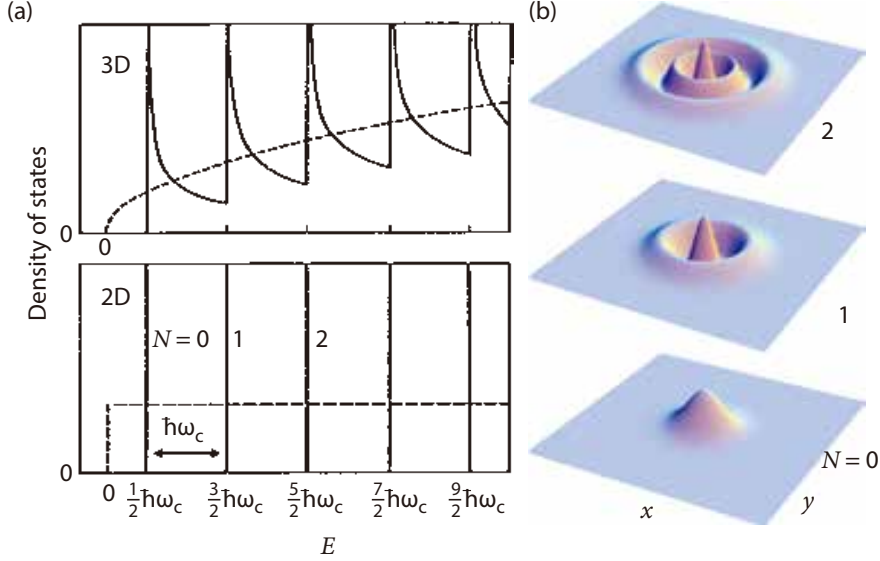


Figure 7: (a) Density of states for a clean system in the absence (dashed lines) or in the presence (solid lines) of a magnetic field in two-dimensional (lower panel) or in three-dimensional (upper) systems. (b) Wavefunctions for a 2D system in the symmetric gauge for various values of the Landau index N .

where $|0\rangle$ is the vacuum of boson b . If we go to the first-quantised form, the wavefunction is expressed, in polar coordinates (r, θ) , as

$$\psi_{Nm}(\mathbf{r}) \propto \exp(-im\theta - r^2/4\ell^2) r^m L_N^{|m|}(r^2/2\ell^2), \quad (20)$$

where $L_N^{(m)}(z)$ is the associated Laguerre polynomial. They are depicted in Fig.7(b). By restricting the radius R of these wavefunctions within a radius of a disk, we recover the degeneracy of a Landau level.

In terms of the degeneracy, we can now define the Landau level filling factor, i.e., the fraction of the occupied states for a given Landau level. If we denote the density of electrons by n_e , the Landau level filling factor ν is

$$\nu \equiv n_e/n_\phi = 2\pi\ell^2 n_e. \quad (21)$$

In other words, $1/\nu$ is the number of flux quanta per electron. The above is the essence of Landau's quantisation, formulated by Landau in 1930, and the discovery of the QHE in 1980 coincided with its half centenary.

When only the lowest (or lowest few) Landau level(s) are occupied (i.e., $\nu < \sim 1$) for strong enough magnetic fields, the situation is called the ‘‘quantum limit’’. For GaAs with a typical density of electrons $n \sim 10^{11} \text{ cm}^{-2}$, we have

$$\nu = \frac{4}{B[\text{T}]} \times n[10^{11} \text{ cm}^{-2}]$$

where B is in units of Tesla and n_e in 10^{11} cm^{-2} , so that the quantum limit is realised for $B > \sim 4 \text{ T}$.

So far we have considered a clean system. In the presence of disorder, such as a random potential $V(\mathbf{r})$, arising from impurities, interface roughness etc, cyclotron orbits that have different centre coordinates (X, Y) are no longer degenerate, but are subject to scattering. Then the equation of motion for (X, Y) are obtained from its commutator with \mathcal{H} as

$$\begin{aligned}\dot{X} &= \left(\frac{i}{\hbar}\right) [V, X] = \frac{\ell^2}{\hbar} \frac{\partial V}{\partial y}, \\ \dot{Y} &= \left(\frac{i}{\hbar}\right) [V, Y] = -\frac{\ell^2}{\hbar} \frac{\partial V}{\partial x}.\end{aligned}\quad (22)$$

The fact that $\dot{\mathbf{R}} \propto \hat{\mathbf{e}}_z \times \nabla V$ implies that $\mathbf{R} \equiv (X, Y)$ moves, classically, along equipotential contours with a velocity proportional to $|\nabla V|$. Quantum mechanically, however, the Hamiltonian, with the Landau wavefunctions as a basis, reads

$$\mathcal{H} = \sum_{NM} \left(N + \frac{1}{2}\right) \hbar \omega_c c_{NX}^\dagger c_{NX} + \sum_{NXN'X'} \langle NX|V|N'X'\rangle c_{NX}^\dagger c_{N'X'}, \quad (23)$$

where c_{NX}^\dagger creates an electron in the Landau's wavefunction $|NX\rangle$ (here in the Landau gauge, $\mathbf{A} = (0, Bx)$, rather than in the symmetric gauge), and the second term on the right-hand side represents the quantum mechanical hopping between cyclotron orbits at different positions. The ‘‘hopping’’ matrix element $\langle NX|V|N'X'\rangle$ becomes large when the random potential varies rapidly in space (on the magnetic length scale, eqn(11), since each function $|NX\rangle$ has a spatial extension $\sim \ell$).

In the presence of the hopping, each Landau level is broadened from the line spectrum. Electronic structure and transport properties of the disordered, Landau-quantised systems in 2D were theoretically studied with the self-consistent Born approximation in the 1970's by Uemura, Ando and coworkers [9, 8]. In this formalism the lifetime of an electronic state due to disorder is taken into account in a self-consistent way, which is imperative, since the unperturbed system has anomalous, delta-function spectra. Let us assume that the random potential $V(\mathbf{r}) = \sum_i 2\pi\ell^2 V_0 \delta(\mathbf{r} - \mathbf{r}_i)$ is expressed as a sum of the contributions from short-range (delta-function like) impurity potentials at position \mathbf{r}_i with the average number of impurities per unit area n_i . For dense impurities (to be more precise, for the dimensionless concentration $c_i \equiv 2\pi\ell^2 n_i \gg 1$) we can adopt the Born approximation. There, the self-energy due to the impurity scattering is given as $\Sigma(E) = c_i V_0^2 G(E)$, where the self-consistency demands that Green's function, $G(E)$, contain the effect of $\Sigma(E)$. Then each Landau level is broadened with a width, $\Gamma = 2\sqrt{c_i} V_0$.

In other words, the ratio between the Landau-level broadening Γ and the cyclotron energy is

$$\Gamma/(\hbar\omega_c) \sim 1/(\omega_c\tau_0)^{1/2}, \quad (24)$$

where $\tau_0 = (n_i V_0^2 m^*/\hbar^3)^{-1}$ is the scattering relaxation time due to the disorder in zero magnetic field. Intuitively, the quantity $\omega_c\tau_0$ gives a measure of how many times an electron can rotate on a cyclotron orbit between scattering events on average. For sufficiently large magnetic field and/or small disorder we have $\Gamma/\hbar\omega_c < 1$ (i.e., $\omega_c\tau_0 > 1$), for which Landau levels are separated, while Landau levels are merged in the opposite condition. To give an idea about the magnitudes of relevant quantities, we have

$$\hbar\omega_c = 0.12B[\text{T}](m_0/m^*) \text{ meV},$$

$$\Gamma \sim 0.15\sqrt{B[\text{T}]/\mu},$$

where B is measured in units of Tesla, the effective mass is set to $m^* = 0.067m_0$ (m_0 : bare mass of an electron) for GaAs and $\mu = e\tau_0/m^*$ is the carrier mobility here measured in units of $10^4 \text{ cm}^2/(\text{V}\cdot\text{s})$.

3 Integer quantum Hall effect — experiments

The Landau quantisation in 2DEG described above is reflected in various properties, especially in transport properties. There are prehistories for the the QHE physics that are precursors of the discovery. As early as in the 1960's Shubnikov de Haas effects were observed in Si-MOSFET's by Landwehr's group, and by groups in US and in Japan. Shubnikov de Haas effect is an oscillations (versus an external magnetic field B) in transport properties, which is general enough but the effect becomes peculiar in 2DEG, since the oscillations in σ_{xx} and σ_{xy} reflect the line-like Landau levels. In the 1970's more elaborate experimental studies did exhibit oscillatory behaviours indicative of Landau levels in 2D. Figure 8 shows a typical example[10], along with a theoretical result. It was also recognised that there are regions of vanishing σ_{xx} and flat σ_{xy} between Landau levels, which are called "plateaux".

In 1980, von Klitzing, Dorda and Pepper found an astonishing behaviour in the Hall conductivity as shown in Fig.9.[11] In a Si MOSFET in strong magnetic fields (~ 20 T), the heights of the Hall resistance R_{xy} are quantised very accurately into (integer) $^{-1}$ times $h/e^2 = 25\,813\ \Omega$, or when translated to the Hall conductivity σ_{xy} as

$$\sigma_{xy} = -N \frac{e^2}{h} \quad (N : \text{integer}). \quad (25)$$

Astonishing, because (a) the quantised value only contains the fundamental physical constants, the elementary charge e and Planck's constant h (whereas ordinarily transport properties are naturally affected by various material parameters, etc), and (b) this occurs in disordered systems. This has become known as the quantum Hall effect. A few years after this discovery the fractional quantum Hall effect was discovered, so the original effect is called the integer quantum Hall effect. Remarkably, the accuracy of the quantisation is experimentally confirmed to be better than 10^{-7} . Hall effect itself was discovered by Edwin Hall in 1879, so it was almost exactly a century later when the quantum Hall effect was discovered. Subsequently, experimental data were refined, where the quantum Hall steps are almost a series of step functions, as typically shown in Fig.10, which are then interpreted in terms of the localisation, as we shall see in the section on localisation.

3.1 Materials and sample geometry

Historically the integer quantum Hall effect was discovered in Si-MOSFET's, but subsequently studied for 2DEG's in semiconductor heterostructures, typically GaAs/AlGaAs (Fig.4). Integer QHE has also been observed in heterostructures other than GaAs/AlGaAs, which include 2D hole (as opposed to electron) gas systems in p-type GaAs, type III heterostructures such as GaSb-InAs where 2D electron and 2D hole gases coexist side by side, and Si/Si $_{1-x}$ Ge $_x$ strained heterostructures with different band structure and higher effective masses than those in Si MOSFET's.

In measuring Hall resistivity, basically two sample geometries are used — Hall bar geometry and Corbino geometry (Fig.6(b)). The former is usually adopted with a multi-terminal geometry. In the latter, where electrodes are attached to the inner and outer perimeters of an annular sample, an advantage is that we do not have to worry about the sample edges and edge transports, nor do we need to worry about "hot spots" (Fig.6(c)); see the section on real-space

imaging below). Namely, in the QHE condition, where we have $\sigma_{xy} = \text{integer} \times e^2/h$, $\sigma_{xx} = 0$ with the Hall angle $[= \tan^{-1}(\sigma_{xy}/\sigma_{xx})]$ of 90 degrees, the Hall current flows around the annulus. QHE has also been observed in Corbino geometry. In fact some of the early Shubnikov de Haas experiments were done for this geometry.

An electron has a spin 1/2, and the associated Zeeman energy in a magnetic field. The Zeeman energy is much smaller than the cyclotron energy in usual experimental situations (although the spin splitting is enhanced due to exchange interactions to be precise), so that every Landau level is almost twofold spin degenerated. Later, the effects of the spin splitting on QHE have been elaborated with various experimental techniques. In the case of Si-MOSFET, a valley degeneracy also exists, since the bulk Si has multiple valleys in the band structure.

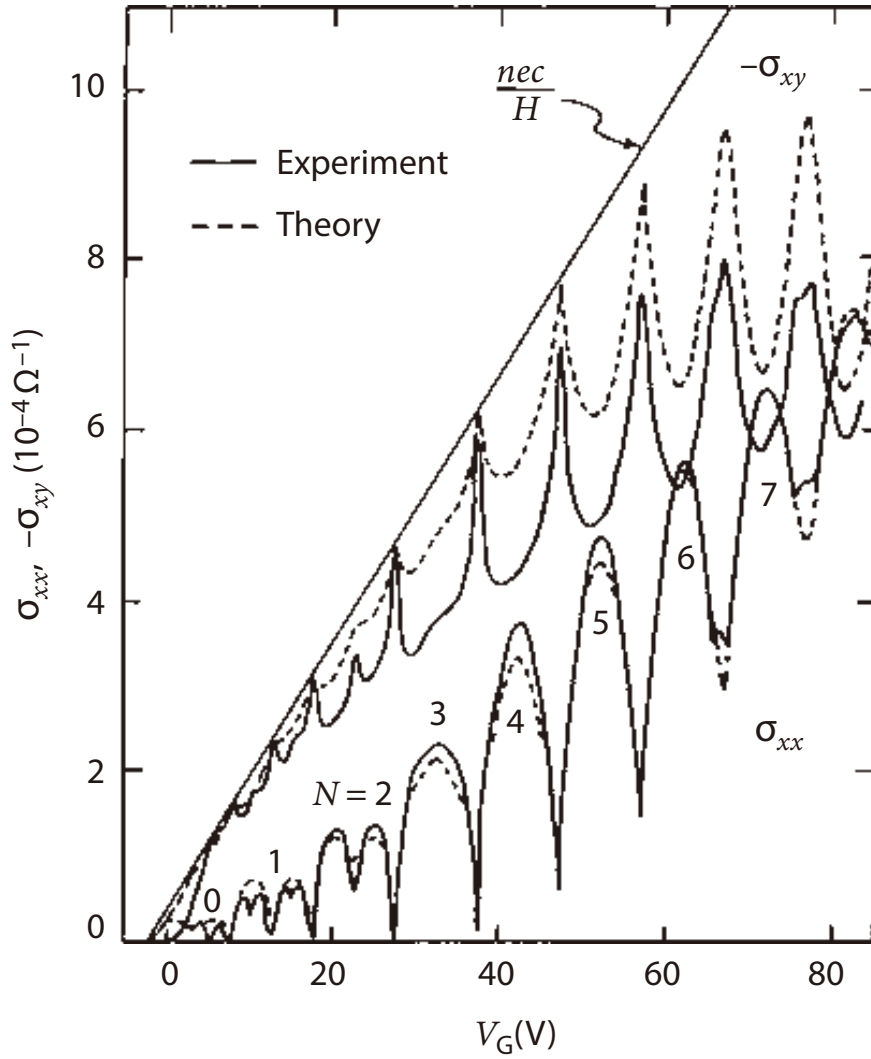


Figure 8: A typical experimental result (solid lines) with a theoretical fit (dashed) for σ_{xx} and σ_{xy} , against the gate voltage V_G which is roughly $\propto n$ in a MOSFET sample [after T. Igarashi, J. Wakabayashi and S. Kawaji, Suppl. Progr. Theoret. Phys. No.57, 176 (1975)].

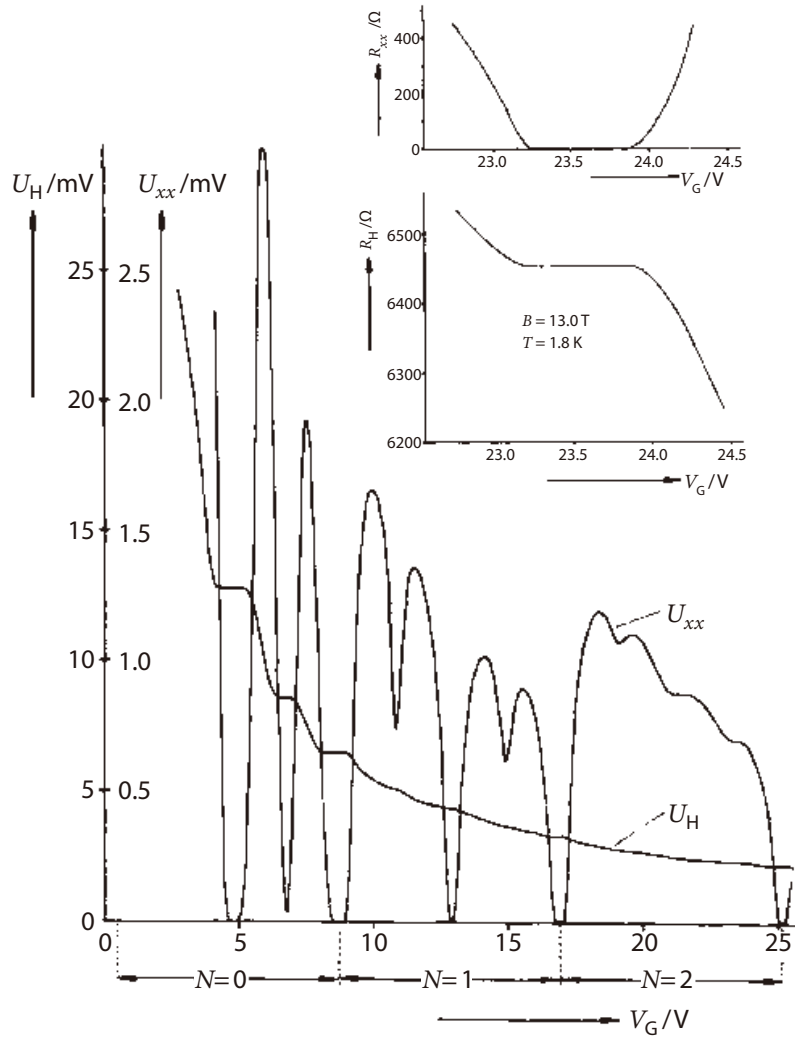


Figure 9: The original QHE result for the Hall (U_H) and longitudinal (U_{xx}) voltages against the gate voltage V_G at $T = 1.5$ K and $B = 18$ T. Inset shows a detail around the fully occupied $N = 0$ Landau level [after K. von Klitzing, G. Dorda and M. Pepper, Phys. Rev. Lett. **45**, 494 (1980)].

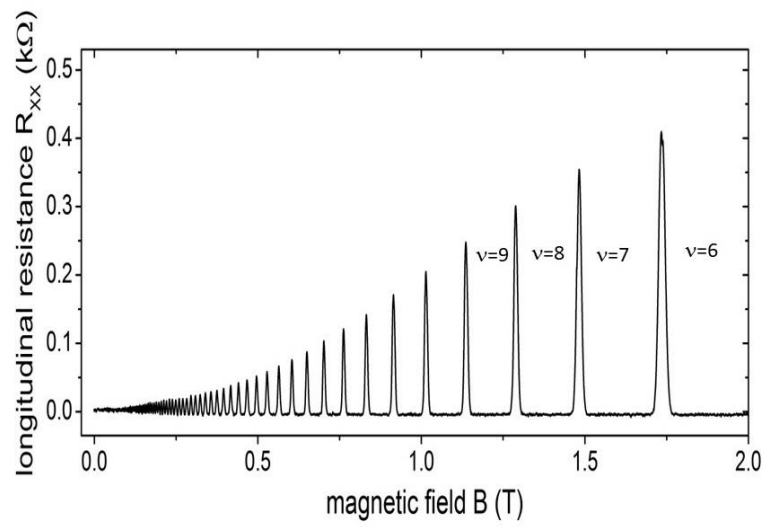


Figure 10: A typical result for the longitudinal resistance R_{xx} and Hall resistance R_H in the GaAs- $\text{Al}_x\text{Ga}_{1-x}\text{As}$ IQHE system. [after B. Friess, PhD thesis (Technische Universität München, 2014) <https://mediatum.ub.tum.de/1219842>].

3.2 Optical properties

QHE systems exhibit characteristic optical properties as well as characteristic transport properties. Optical measurements have advantages that (i) this is a contactless method, and (ii) we can probe both luminescence and absorption. In the QHE regime, luminescence spectra have been obtained for Si MOSFET's and semiconductor heterostructures. The luminescence spectra, which measures the radiative recombination of 2D electrons with photoexcited holes, reflect the Landau level structure. One feature is that the Landau-level width as deduced from the width of the luminescence spectra oscillates with magnetic field with a maximum every time a Landau level is filled. This is associated with the screening which becomes effective when the Landau levels are partially filled (i.e., an open shell). There are other properties which include spin-dependent relaxations.

Cyclotron absorption is another important experimental technique in the QHE regime. The technique can probe lower carrier-density regions than in transport measurements. Landau level structures have been probed, where oscillatory line widths, spin splitting, nonparabolicity effects, etc have been observed. Inelastic light scattering is another powerful optical method that compliments luminescence. These methods are schematically illustrated in Fig.11.

More recently, the optical Hall conductivity $\sigma_{xy}(\omega)$ is theoretically predicted to have a Hall plateau structure in the THz regime in quantum Hall systems both in 2DEG and graphene, which we shall describe in Section "Optical properties in graphene" below.

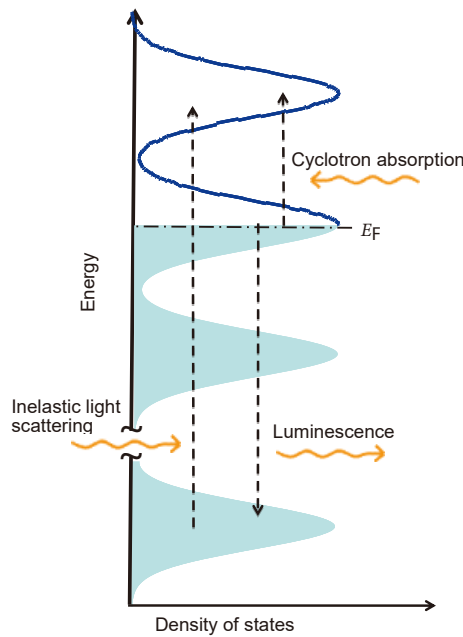


Figure 11: Various optical processes are schematically shown.

3.3 Other properties

There are host of other properties that have been measured. One is the electronic specific heat, which probes the Landau quantisation through the density of states (that include both localised

and delocalised states), while transport measurements mainly probe the delocalised states. Another method to probe the density of states is the magnetocapacitance (Fig.12). Magnetisation has also been measured, with torque magnetometers or micromechanical cantilevers, where jumps are observed as E_F traverses the Landau levels (Fig.13).

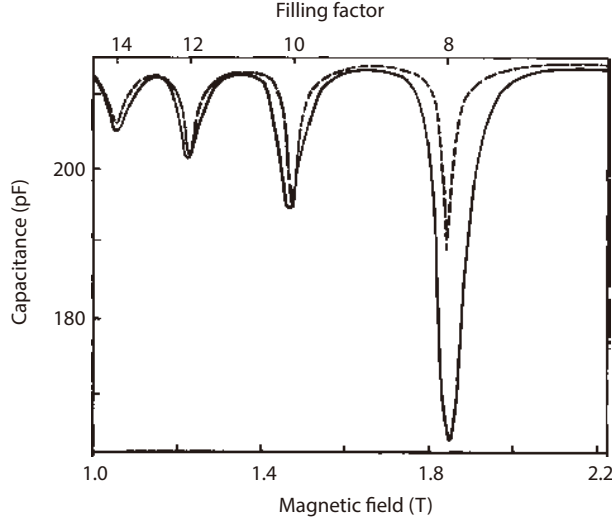


Figure 12: Experimental (solid line) and theoretical (dashed) results for the capacitance against magnetic field. Landau level filling is indicated on the upper axis [after T. P. Smith et al, Phys. Rev. B **32**, 2696 (1985)].

Various other properties have been experimentally studied, among which is the thermoelectric effect. This probes how the electrons sustain temperature gradients in 2DEG's, where the dominant mechanism for the thermopower is phonon drag. Another magneto-thermoelectric effect is a heat flow (or a temperature gradient) that is perpendicular to both the electric current and the magnetic field, known as the Nernst-Ettingshausen effect. Namely, the electric field \mathbf{E} and the temperature gradient ∇T are related as $\mathbf{E} = \mathcal{S}\nabla T$. Here \mathcal{S} is the thermopower tensor, where S_{xx} corresponds to the thermopower while S_{xy} to the Nernst-Ettingshausen coefficient (Fig.14).[12]. The effect has been studied both theoretically and experimentally in conjunction with the breakdown of QHE

3.4 QHE in other materials

There are a multitude of developments for the integer QHE in wider classes of materials. Let us here just mention the realisation of QHE in oxide heterostructures as an example. The system is zinc oxide (ZnO), which is an insulator, or a wide-gap semiconductor. When heterostructures such as ZnO/Mg_xZn_{1-x}O are grown with MBE, MgZnO layer acts as a potential barrier for the 2DEG in ZnO layer in realising a 2DEG. The carrier density (typically $\sim 10^{12}$ cm⁻²) systematically depends on the composition x and the growth temperature, where spontaneous and piezoelectric polarisation effects work to accumulate carriers at the heterointerface. The condition necessary to have QHE (i.e., $\omega_c\tau_0 > 1$) is met, and a typical result (Fig.15) exhibits a clear IQHE.[13]

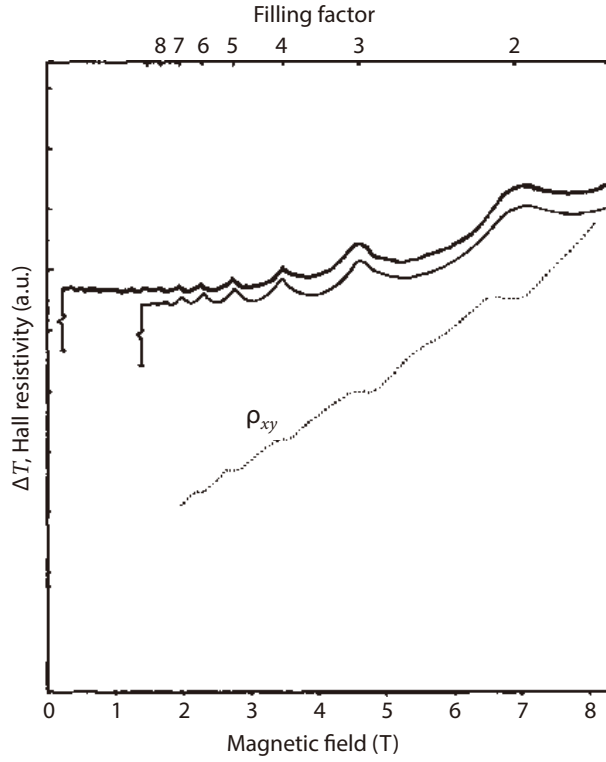


Figure 13: Experimental (thick line) and theoretical (thin) results for the magnetisation as probed by the temperature change, ΔT , in the heat-pulse method, along with ρ_{xy} against magnetic field [after E. Gornik et al, Phys. Rev. Lett. **54**, 1820 (1985)].

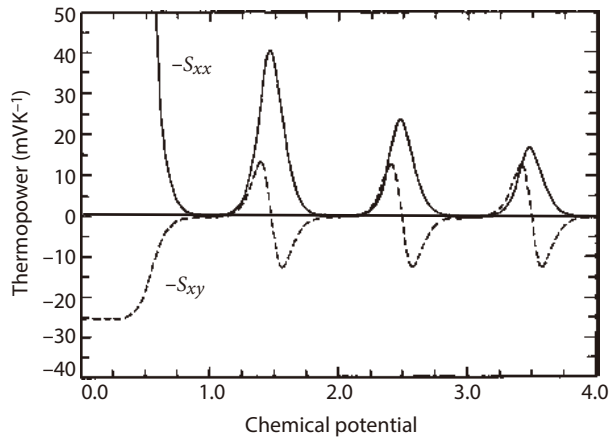


Figure 14: A typical theoretical result for the diagonal (S_{xx}) and off-diagonal (S_{xy}) components of the thermopower tensor against chemical potential [after M. Jonson and S. M. Girvin, Phys. Rev. B **29**, 1939 (1984)].

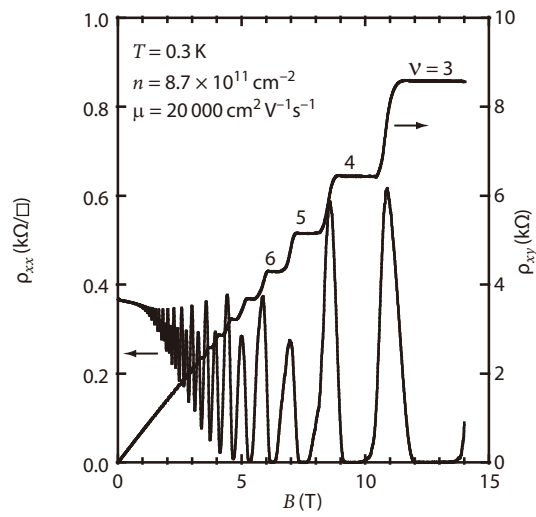


Figure 15: QHE in an oxide heterostructure $\text{ZnO}/\text{Mg}_x\text{Zn}_{1-x}\text{O}$. After A. Tsukazaki et al, Phys. Rev. B **78**, 233308 (2008).

4 Integer quantum Hall effect — theories

4.1 Localisation in Landau levels

Let us start with the localisation problem in the QHE system, since this has to do with a first essential question about the integer QHE — the presence of plateaux in σ_{xy} versus the density of electrons n (or vs $B \propto 1/\nu$ for a fixed n). Experimentally the plateau in σ_{xy} goes hand in hand with a region of vanishing σ_{xx} . This is a curious situation, since, usually σ_{xy} should be an increasing function of n while σ_{xx} as a function of n should not be zero (as opposed to the quantities as functions of energy E).

This has been explained from the Anderson localisation of the wavefunctions in the Landau levels that arises from disorder in the system. The Anderson localisation was proposed back in 1958 for general electron systems in the presence of disorder, and was subsequently culminated as the scaling theory of localisation in 1979. In a clean crystal every wavefunction is a Bloch state that extends over the entire sample. By contrast, in a disordered system wavefunctions can be spatially localised, whose spatial extension is characterised by the localisation length that depends on energy. In the presence of magnetic fields, the Anderson localisation was suggested to occur as well for wavefunctions in the Landau levels in the 1970's (Fig.16). For random potentials that vary slowly in space, an electron follows, semiclassically, an orbit that is an equipotential contour as we have shown in a section above. Quantum mechanically, however, an electron tunnel between these orbits even for a slowly-varying potential, where the quantum mechanical hopping becomes more frequent for rapidly-varying (i.e., short-ranged) random potentials (see Fig.17). So the question becomes how the localisation arises in the presence of the quantum mechanical hopping. Then the plateaux in σ_{xy} and regions of vanishing σ_{xx} have been suggested to come from the localisation.[14] A peculiarity in the localisation in the QHE system is that the disorder has a dual role: disorder causes the localisation on one hand, but it gives rise to quantum mechanical hopping of cyclotron guiding centres to contribute to transport at the same time, as pointed out by Aoki and Kamimura[15].

4.2 Linear-response theory

The most standard method to treat conductivities microscopically is the linear-response theory, or the Kubo formula. Aoki and Ando[14] have applied this to the QHE problem. While the plateaux in σ_{xy} and vanishing regions in σ_{xx} are explained by the localisation, the puzzle remains as to why the value of the plateaux in disordered systems is quantised into the universal e^2/h , which is originally the value for the clean 2DEG when the Landau level filling coincides with an integer. In other words, if a disorder makes σ_{xx} zero, why does the disorder allow σ_{xy} to stick to the quantised value.

In the linear-response theory, the conductivity is given by a current-current correlation function. In the QHE system, the current has to do with the dynamics of the cyclotron guiding centre (X, Y) , which is subject to quantum mechanical hopping. The conductivities, both longitudinal and Hall, are given as correlation functions of \dot{X} and \dot{Y} (with a dot denoting a time derivative) as

$$\sigma_{xx} = e^2 \langle\langle \dot{X} \dot{X} \rangle\rangle,$$

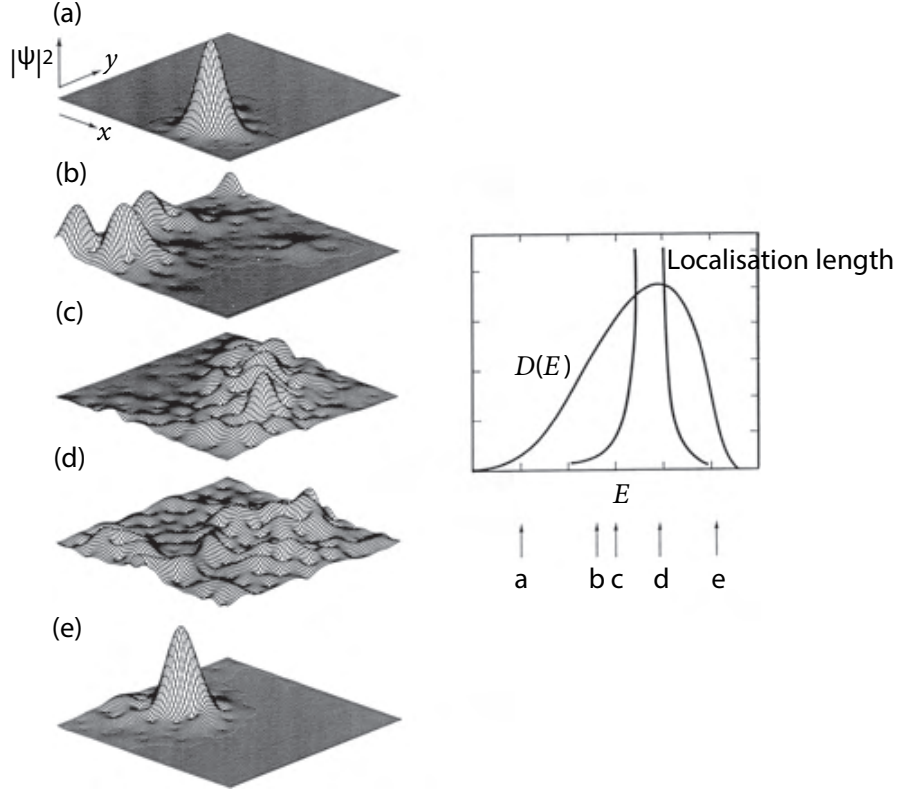


Figure 16: Typical wavefunctions in a disordered QHE system obtained in a computer simulation for various eigenenergies as indicated on the right panel, which shows the density of states and the localisation length against energy [after H. Aoki, J. Phys. C **10**, 2583 (1977)].

$$\sigma_{xy} = -\frac{ne}{B} + \Delta\sigma_{xy}, \quad (26)$$

$$\Delta\sigma_{xy} = \frac{e^2}{2} (\langle\langle \dot{Y}\dot{X} \rangle\rangle - \langle\langle \dot{X}\dot{Y} \rangle\rangle). \quad (27)$$

Here $\langle\langle AB \rangle\rangle \equiv \frac{1}{L^2} \int_0^\infty dt \exp(-\delta t) \int_0^\beta d\lambda \langle A(-i\hbar\lambda)B(t) \rangle$, where $\langle \rangle$ is the canonical ensemble average plus the average over disorder, $\beta = 1/k_B T$, δ a positive infinitesimal, and $A(t)$ the Heisenberg representation of an operator A .

$\Delta\sigma_{xy}$ is expressed as a combination $\langle\langle \dot{Y}\dot{X} \rangle\rangle - \langle\langle \dot{X}\dot{Y} \rangle\rangle$ for the following reason. For the conductivity tensor in a magnetic field B , Onsager's reciprocal theorem dictates that

$$\sigma_{\mu\nu}(B) = \sigma_{\nu\mu}(-B),$$

so that we can decompose σ into the symmetric part σ^s and the antisymmetric part σ^a . Then the current \mathbf{j} is expressed as

$$j_\mu = \sum_\nu \sigma_{\mu\nu}^s E_\nu + \sigma_{xy}^a (\mathbf{E} \times \hat{\mathbf{e}}_z)_\mu, \quad (28)$$

where the part of the current (i.e., the Hall current) that is induced by the magnetic field ($\parallel z$ and perpendicular to the applied electric field \mathbf{E}) is related to σ^a . [16]

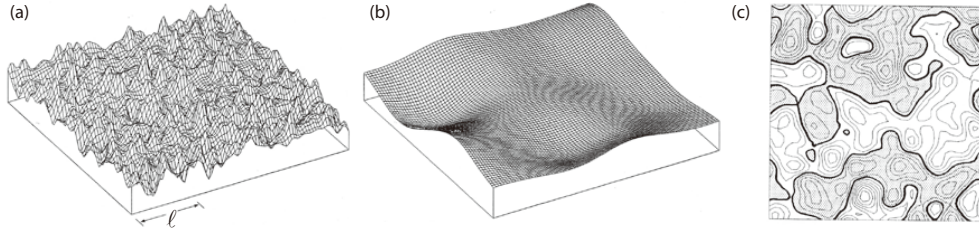


Figure 17: A random potential rapidly-varying as compared with the magnetic length ℓ (left panel), and a slowly-varying one (right) are schematically shown. (c) A typical contour plot with shaded areas indicate $E < 0$ and thick lines $E = 0$ contour [after H. Aoki, Rep. Prog. Phys, **50**, 655 (1987)].

The linear-response formula may be written in terms of Green's function as

$$\Delta\sigma_{xy} = \frac{e^2\hbar}{i\pi L^2} \int_{-\infty}^{\infty} dE f(E) \left\langle \text{Tr} \left[\dot{X} \frac{\partial}{\partial E} \text{Re}G(E) \dot{Y} \text{Im}G(E) - (\dot{X} \leftrightarrow \dot{Y}) \right] \right\rangle, \quad (29)$$

where $G(E) = (E - \mathcal{H} + i\delta)^{-1}$ is the Green's function, $f(E) = [e^{\beta(E-\mu)} + 1]^{-1}$ Fermi-Dirac distribution function, and \leftrightarrow denotes the term with \dot{X} and \dot{Y} exchanged. In this expression the Hall conductivity σ_{xy} is contributed by all the states below E_F , unlike σ_{xx} that is related to an energy-dissipating process around E_F . In terms of the eigenstates of the Hamiltonian, the Hall conductivity is expressed as

$$\sigma_{xy}(\omega) = \frac{i\hbar e^2}{L^2} \sum_{\alpha \neq \beta} \frac{f(\epsilon_\beta) - f(\epsilon_\alpha)}{\epsilon_\beta - \epsilon_\alpha} \left(\frac{j_x^{\alpha\beta} j_y^{\beta\alpha} - j_y^{\alpha\beta} j_x^{\beta\alpha}}{\epsilon_\beta - \epsilon_\alpha + i\delta} \right), \quad (30)$$

where ϵ_α is α -th eigenenergy, and $j^{\alpha\beta}$ the current matrix elements between the eigenstates.

From this formalism, we can show, in the presence of localisation arising from disorder, that (i) the Hall conductivity σ_{xy} should be rigorously flat (at $T = 0$) as a function of the density n of electrons in the region where the states are localised. This accounts for the flatness of plateaux in the QHE, as depicted in Fig.18.

We can also show that the quantised $\sigma_{xy} = -Ne^2/h$ in a plateau should hold in the limit of strong magnetic fields where adjacent Landau levels are well separated and when E_F is in the gap between them. This in turn implies that, (ii) at least in the limit of strong magnetic fields all the states cannot be localised, otherwise σ_{xy} would be zero over the whole region. This is important, since, according to the scaling theory of localisation all the states must be localised in two dimensions. The only way to go around this universal argument is to go to another universality class, either to the unitary class (e.g., systems in magnetic fields where the time-reversal symmetry is broken, see Fig.1) or to the symplectic class (e.g., systems that have spin-orbit interactions). QHE system belongs to the unitary class, which is why delocalised states are allowed to exist, which in turn makes the QHE to be realised. The theoretical picture explained here for broadened Landau levels, σ_{xx} and σ_{xy} are summarised in Fig.19.

As we shall see below, the topological picture beautifully explains the quantisation of σ_{xy} into e^2/h for finite magnetic fields, where the required condition is E_F being in a gap in the

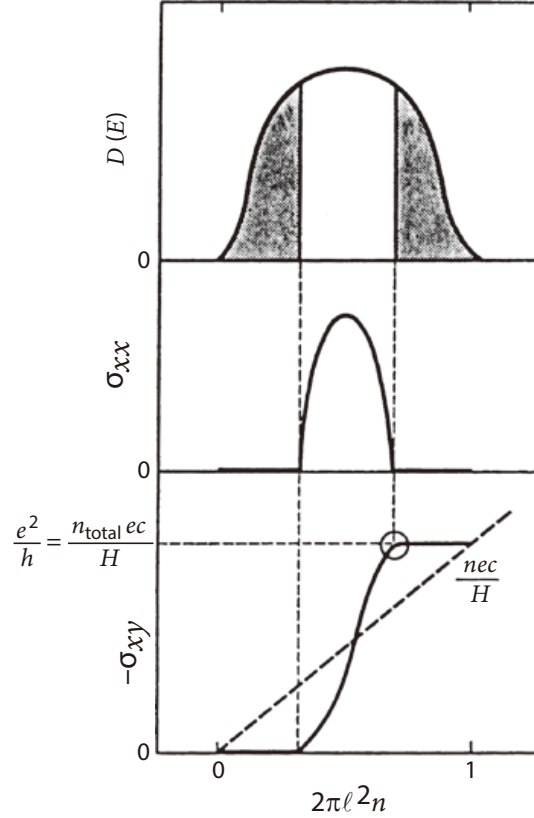


Figure 18: Schematic density of states $D(E)$ (with shaded areas indicating the localised states), the longitudinal conductivity σ_{xx} , and the Hall conductivity σ_{xy} are schematically plotted against the Landau level filling $2\pi\ell^2 n$. In the bottom panel the horizontal dashed line indicates how the quantised value is achieved despite the presence of localisation.

density of states or in a localised regime (mobility gap). Even in the treatment above, however, different Landau levels are not treated as being completely independent. As seen from the fact that the Landau's quantisation is formally equivalent to a 1D harmonic oscillator, the current operator has matrix elements between N and $N \pm 1$ levels, so the mixing between them is implicitly included (in fact, the treatment in terms of the guiding centre (X, Y) corresponds to taking this mixing to the leading order).

It may first seem counter-intuitive that σ_{xy} attains the quantised value despite the presence of localised states. Physically, we can say the following. From the equation of motion for the guiding centre the Hall current j_x in an electric field E_y is given as

$$j_x = -(1/B) \sum_{\alpha'}^{\text{delocalised}} (\langle \alpha' | \partial V / \partial y | \alpha' \rangle + eE_y).$$

There is a kind of sum rule, $\sum_{\alpha'}^{\text{all}} \langle \alpha' | \partial V / \partial y | \alpha' \rangle = 0$, which means that delocalised states move faster to just *compensate* the localised states, which has been confirmed numerically and field theoretically as well.

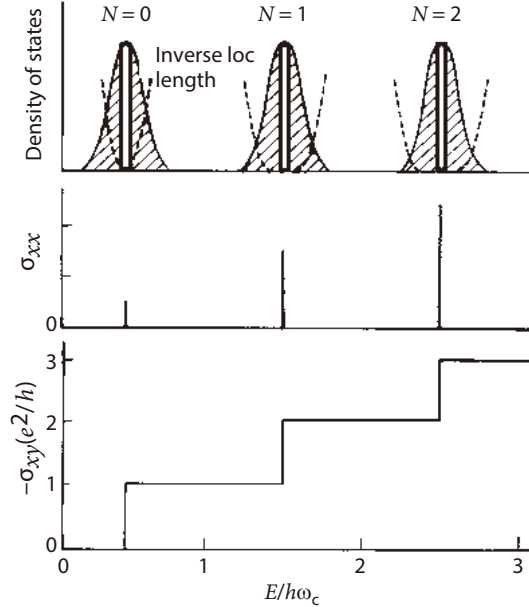


Figure 19: Theoretical density of states (with shaded areas indicating the localised states) along with the inverse localisation length, σ_{xx} , and σ_{xy} are schematically plotted against energy for a series of Landau levels. In the top panel each white region representing the delocalised states actually has zero width in the thermodynamic limit at $T = 0$ [after H. Aoki and T. Ando, Solid State Commun. **38**, 1079 (1981)].

4.3 Středa-Widom formula

As another formalism for the Hall conductivity, Středa's formula[17] is also often evoked. He showed that the Kubo formula for the Hall conductivity can be decomposed into a form, $\sigma_{xy} = \sigma_{xy}^I + \sigma_{xy}^{II}$, where σ_{xy}^I is the Drude-like part that tends to $\sigma_{xy}^I \rightarrow -\omega_c \tau_0 \sigma_{xx}$ in the relaxation time picture. The second term is expressed as

$$\sigma_{xy}^{II} = ec \left[\frac{\partial N(E)}{\partial B} \right]_{E=E_F}, \quad (31)$$

where $N(E)$ is the integrated density of states. When the Fermi energy E_F is in an energy gap, σ_{xy}^I vanishes, while we can show that $\sigma_{xy}^{II} = -(e^2/h)N$ when E_F is in a gap between the N -th and $(N + 1)$ -th Landau levels. Thermodynamically, we have the electric field, $\mathbf{E} = \nabla(\mu/e)$ with μ being the electrochemical potential, so that the Hall current $\mathbf{j}_H = c\nabla \times \mathbf{M}$ with \mathbf{M} being the magnetisation can be expressed as $\mathbf{j}_H = ec\mathbf{E} \times (\partial\mathbf{M}/\partial\mu)$. If we use, following Widom, the thermodynamic Maxwell's relation, $\partial\mathbf{M}/\partial\mu = \partial N/\partial\mathbf{B}$, which comes straight from $\mathbf{M} = -\partial\Omega/\partial\mathbf{B}$ with the grand potential Ω , we recover the formula for σ_{xy}^{II} . [17] Note that the Středa-Widom formula is applicable to the situation where the spectrum has an energy gap.

4.4 Laughlin's gauge argument

As a transparent approach to QHE, Laughlin has proposed an argument based on a gauge transformation.[18] Consider a Gedankenexperiment, in which a QHE system is wound into a cylinder (but the magnetic field is still applied perpendicular to every point on the cylinder), as in Fig.20. To this we add a magnetic flux Φ (due to, say, a solenoid) that pierces the cylinder. Through its vector potential, $A_\theta = \Phi/2\pi r$ (in cylindrical coordinates), the flux exerts an Aharonov-Bohm effect on the electrons. We can eliminate the vector potential with a gauge transformation at the cost of the boundary condition twisted to $\psi(\theta) \rightarrow \exp[i(\Phi/\phi_0)\theta]$ on the wavefunction ψ , where $\phi_0 = ch/e$ is the flux quantum.

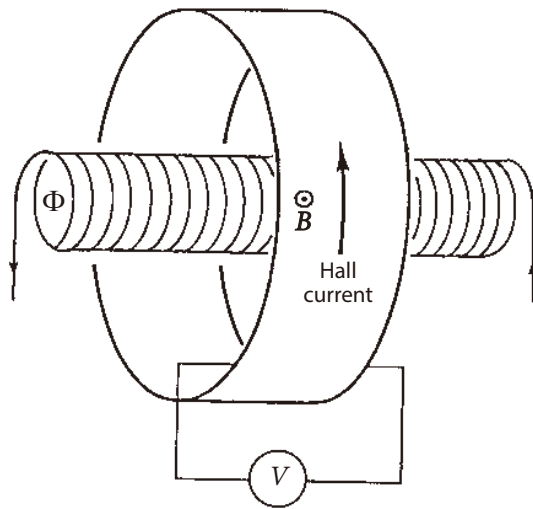


Figure 20: Geometry considered by Laughlin.

If we increase Φ with time, we recover the original periodic boundary condition every time Φ increases by ϕ_0 in a time interval Δt . When the Fermi energy E_F is in a gap in the density of states or in the energy region for localised states (as described in the previous section), the occupation of electrons must be the same when we make $\Phi \rightarrow \Phi + \phi_0$. The only change, then, should be a transfer of an integer (M) number of electrons from one electrode to another, which we assume to be attached to either edge of the cylinder as Hall probes. From the Maxwell equation, an electric field $LE_y = -(1/c)\partial\Phi/\partial t$ is induced along the cylinder of circumference L , which should result in a Hall current, $j_x = -(-e)M/(L\Delta t) = -(Me^2/h)E_y$, and we have $\sigma_{xy} = -Me^2/h$. So the derivation applies to arbitrary strength of the magnetic field as far as the Fermi energy E_F is in a gap in the density of states, or in the energy region for localised states.

4.5 TKNN's topological arguments

In Laughlin's argument we have introduced an Aharonov-Bohm magnetic flux, but subsequently it has been shown that we can go even further to express the Hall conductivity as a topological invariant, which guarantees the quantisation in a mathematically rigorous manner. Namely, Thouless, Kohmoto, Nightingale and den Nijs (TKNN)[19] have considered, for a QHE system periodic both in x and y directions with twisted boundary condition for each of x and y directions, which corresponds to introducing a vector potential, $\mathbf{A} = (A_x, A_y)$, describing fictitious fluxes. Then the Hall conductivity averaged over (A_x, A_y) reads

$$\begin{aligned} \frac{\langle \sigma_{xy} \rangle}{e^2/h} &= \frac{1}{2\pi i} \sum_j^{\text{occup}} \iint \left(\left\langle \frac{\partial u^j}{\partial A_x} \middle| \frac{\partial u^j}{\partial A_y} \right\rangle - \left\langle \frac{\partial u^j}{\partial A_y} \middle| \frac{\partial u^j}{\partial A_x} \right\rangle \right) dA_x dA_y \\ &= -i \frac{e^2}{L^2} \int \frac{d\mathbf{k}}{(2\pi)^2} \sum_{\alpha} f(\varepsilon_{\alpha\mathbf{k}}) \left[\nabla_{\mathbf{k}} \times \langle \alpha\mathbf{k} | \nabla_{\mathbf{k}} | \alpha\mathbf{k} \rangle \right]_z \\ &= \frac{e^2}{h} \sum_{\alpha} C_{\alpha}. \end{aligned} \quad (32)$$

This is the celebrated TKNN formula. In the first line u^j is the j th eigenfunction and the summation is over the occupied states, while in the second line L the sample size, f the Fermi distribution function, $\varepsilon_{\alpha\mathbf{k}}$ the energy of the Bloch wavefunction $|\alpha\mathbf{k}\rangle$ in the α th band, and $\nabla_{\mathbf{k}}$ is the gradient with respect to \mathbf{k} . The expression coincides with a topological invariant C_{α} (that always takes integer values) known as the first Chern character in the differential geometry. This is seen if we rewrite the formula as

$$\langle \sigma_{xy} \rangle \sim \sum_{\alpha} \int d\mathbf{k} \nabla_{\mathbf{k}} \times \mathcal{A}_{\alpha}(\mathbf{k}), \quad (33)$$

where $\mathcal{A}_{\alpha}(\mathbf{k}) \equiv -i \langle \alpha\mathbf{k} | \nabla_{\mathbf{k}} | \alpha\mathbf{k} \rangle$ is a fictitious gauge potential. So the Hall conductivity (in units of e^2/h) is just the topological invariant. The reason why a differential geometry is relevant is that the wavefunction in 2DEG in a magnetic field has such a property that wavefunction changes in a manner that depends on the path along which we adiabatically change (A_x, A_y) as $\rightarrow (A_x + \delta A_x, A_y) \rightarrow (A_x + \delta A_x, A_y + \delta A_y)$ or as $\rightarrow (A_x, A_y + \delta A_y) \rightarrow (A_x + \delta A_x, A_y + \delta A_y)$. The difference is related to the phase of the wavefunction, which is a kind of Berry's phase that generally arises when a quantum system is subject to an adiabatic change. When a vector (to which a wavefunction belongs in a Hilbert space) ends up with different vectors for different parallel transports, we say the space in which the vectors reside is curved. The integrand in the expression for the Hall conductivity indeed represents the curvature ("Berry's curvature" here), and Euler's theorem dictates that the curvature integrated over the surface is an integer.

Alternatively, we can express the linear-response Hall conductivity in terms of Green's function G as

$$\frac{\langle \sigma_{xy} \rangle}{e^2/h} = \frac{1}{8\pi^2} \int_{\mathcal{C}} dz \int \int_0^{\phi_0/L} dA_x dA_y \text{Tr} \left[G \frac{\partial G^{-1}}{\partial A_x} G \frac{\partial G^{-1}}{\partial A_y} G \frac{\partial G^{-1}}{\partial z} - (x \leftrightarrow y) \right]. \quad (34)$$

When E_F is in a localised regime, we can close the contour \mathcal{C} on the plane of complex energy z , and the above expression coincides with a topological invariant (Pontrjagin number). This

expression reduces, for a fixed number of electrons, to the TKNN formula if we note $\mathbf{j} = \partial\mathcal{H}/\partial\mathbf{A}$.

For clean systems, the topological expression indicates that the Hall conductivity, for arbitrary strength of B , is quantised topologically when E_F is in a gap of the energy spectrum. For disordered systems, the topological expression indicates that the Hall conductivity is quantised when E_F is in the energy region of localised states, since in that case \mathbf{A} -averaged σ_{xy} is equal to the unaveraged one. In practice, σ_{xy} is a smooth function (rather than a step function) of energy for finite samples or at a finite T . Namely, we can show that, even though σ_{xy} for each of disordered samples is individually quantised, the quantity becomes a smooth function of energy after the ensemble average over randomness (which corresponds to the observable quantity), and the latter tends to the σ_{xy} (not integrated over \mathbf{A}) in the thermodynamic limit. [20] Figure 21 shows the outline of the topological numbers for clean and random systems.

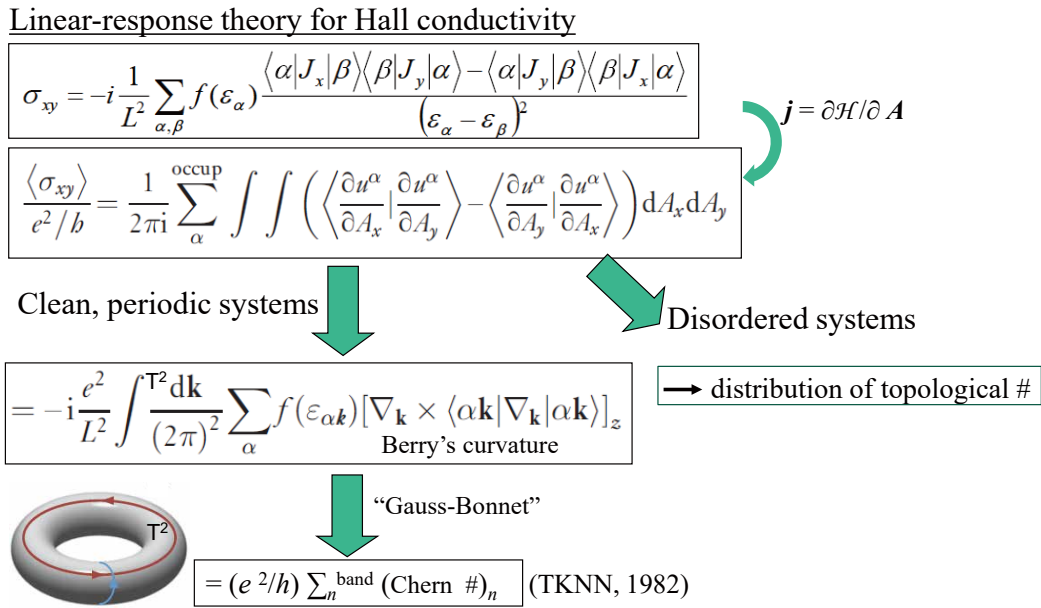


Figure 21: Topological expressions for the quantum Hall conductivity via the linear-response theory. For clean systems we arrive at the TKNN formula, while for disordered system we can consider the distribution of topological numbers. Bottom left inset is a torus representing the first Brillouin zone in k -space.

Field theoretically, we can introduce a topological term (as in the θ term in the Yang-Mills field theory) in the Lagrangian in the nonlinear σ model for the QHE system[21]. Topological phenomena abound in condensed-matter physics, as classically exemplified by vortices in superfluids and fluxoids in superconductors, but QHE thus forms an important and distinct class in the topological phenomena, which has spinoffs in the physics of topological insulator, etc. As exemplified this, QHE is a superb place for exploring field-theoretical interpretations. In addition to the Chern number as the topological quantum number, there are other views that deepen our understanding of the effect. One is related to the quantum anomaly in the field-theoretic language. Quantum anomaly, in the context of particle physics, refers to the

phenomena in which a symmetry inherent in a physical system is broken due to quantum-mechanical effects. In the context of condensed-matter physics, quantum anomaly is referred to those phenomena that can be described in terms of Feynman diagrams resembling those representing the quantum anomaly. This applies to QHE, spin Hall effect, and especially Haldane's model for anomalous QHE (QHE in zero magnetic field), which may be considered as a realisation of what is called the parity anomaly.[22]

5 Localisation problem

5.1 Scaling theory of localisation in two-dimensional systems

As we have seen, the integer QHE is intimately related with the localisation problem. We have also mentioned that the system falls upon the unitary class in 2D. Details of the localisation (which is a non-perturbative problem) has been extensively studied with numerical methods and field theoretical methods. As shown schematically in Figs. 16,19, the localisation becomes stronger towards the edges of a Landau level and the weakest at the centre. Classically, this corresponds to the fact that contours of a random potential, along which the cyclotron guiding centre drifts in the semiclassical picture, are valleys (hills) for energies well below (above) the level centre, while the contours tend to percolating paths for energies close to the centre. However, the localisation is quantum mechanical phenomenon related with interference of wavefunctions.

If we look more closely at the behaviour of the localisation length in a numerical method (finite-size scaling for the Thouless number), the localisation length, although a smooth function of E , exhibits a rather singular behaviour, in which the inverse localisation length becomes zero only at the level centre (i.e., extended states only occur at the single point on energy axis). Namely, the delocalised states, marginally allowed to appear in the presence of magnetic fields in two dimensions, has an energy region coalescing into a single point E_0 (the centre of each Landau level). The localisation length, denoted here as ξ , behaves around this point as

$$\xi \sim 1/|E - E_0|^s, \quad (35)$$

where s (numerically shown to be $\sim > 2$) is the localisation critical exponent.[23] This value may be compared with the exponent $s = 7/3$ for the percolation problem. The effect of quantum mechanical tunnelling has also been extensively studied in terms of a network model due to Chalker and Coddington, who have modelled the quantum mechanical tunnelling across the paths (see Fig.17(c)).[24, 25]

The critical exponent s is shown to depend on the Landau level (larger for $N = 1$ than for $N = 0$). A mapping onto the nonlinear σ model gives an estimate $\xi \sim \ell \exp(\sigma_{\text{SCBA}}^2)$ with $\sigma_{\text{SCBA}} \sim (N + 1/2)e^2/h$ being σ_{xx} in the self-consistent Born approximation[9] and ℓ the magnetic length. So the localisation length increases with N , so does the critical exponent. The localisation length also depends strongly on whether the randomness is rapidly varying or slowly varying in real space as compared with the magnetic length.

5.2 Quantum criticality and $\sigma_{xx} - \sigma_{xy}$ diagram

One way to display the critical behaviour is the $\sigma_{xx} - \sigma_{xy}$ diagram. Namely, while at $T = 0$ σ_{xy} is a step function and σ_{xx} nonzero at discrete points, at finite temperatures not only the Fermi distribution is smeared by $k_B T$, but we have also a finite inelastic scattering length L_ϵ . This can be summarised as the $(\sigma_{xx}, \sigma_{xy})$ flow diagram when T is varied for various values of E_F , as originally evoked in the nonlinear σ model (Fig.22(a)). Namely, we can map the QHE system onto a field-theoretic model called the nonlinear σ model, for which the renormalisation into larger sample sizes can be discussed.[26]

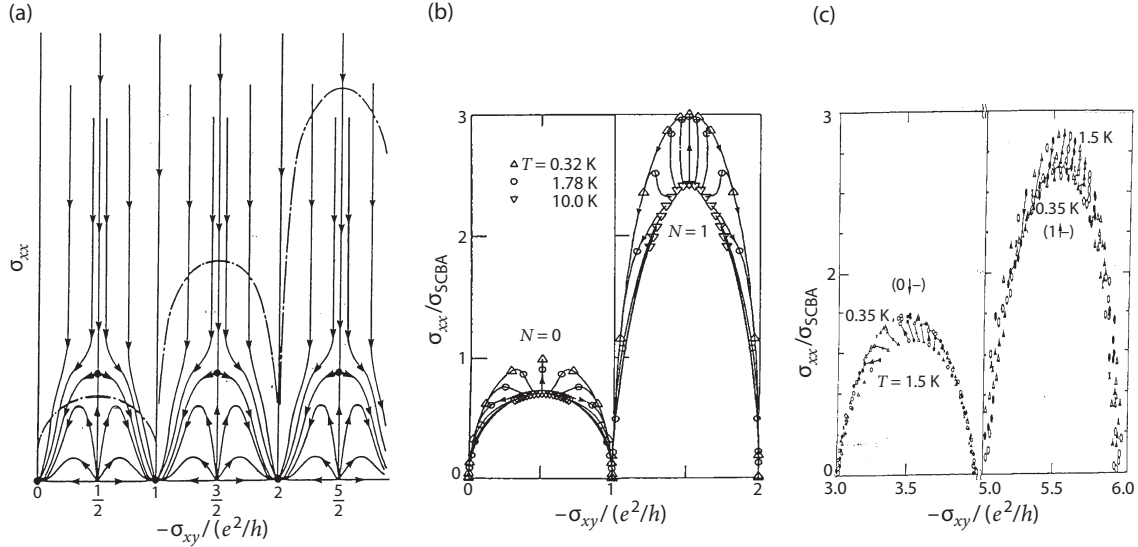


Figure 22: Results for the $\sigma_{xx}-\sigma_{xy}$ diagram: (a) Renormalisation flow lines obtained in the nonlinear σ model [after A. M. M. Pruisken, Phys. Rev. Lett. **61**, 1297 (1988)]. (b) A numerical result [after H. Aoki and T. Ando, Surf. Sci. **170**, 249 (1986)]. (c) An experimental result for $(N, \text{spin}, \text{valley})$ indices indicated [after M. Yamane et al, J. Phys. Soc. Jpn **58**, 1899 (1989)].

We can also vary the sample size for numerical works on the QHE system to look at the renormalisation flow. Alternatively we can change the temperature, which changes the inelastic scattering length, hence effectively changes the sample size (Fig.22(b)). This implies that experimental $(\sigma_{xx}, \sigma_{xy})$ flow lines can be obtained by varying the temperature (Fig.22(c)).

We can also discuss the so-called "plateau-to-plateau transition", which is the energy interval over which one plateau crosses over to another. In terms of the localisation, the states that satisfy $L_\epsilon < \xi(E)$ are effectively delocalised, where L_ϵ is the inelastic scattering length and ξ the localisation length (Fig.23(a)). If we assume the inelastic scattering time behaves like $\tau_\epsilon \sim T^{-p}$ with $p = 2$ in the diffusive regime, the energy region whose width is $\sim T^{p/2s}$ behaves as delocalised, since the localisation length has a critical behaviour $\xi \sim |E - E_0|^{-s}$ while $L_\epsilon \propto 1/T^{p/2}$. If the magnetic field is varied instead, the plateau transition width against B has the width $\Delta B \sim T^{p/2s}$ with the same exponent. Figure 23(b) displays an experimental result.

One important question is how the QHE plateaux vanish as the degree of disorder is increased, where for a large enough disorder the Landau quantisation, along with QHE, should go away. Kivelson et al[27] have considered the problem in terms of what is called the global phase diagram on a $\rho_{xy} - \rho_{xx}$ plane. In this diagram ρ_{xx} is regarded as a measure of the strength of disorder, while ρ_{xy} reflects the Landau level filling. As shown in Fig.24(a), the midpoints, $\sigma_{xy} = (N + 1/2)e^2/h$, between the plateaux in the Hall conductivity are bifurcation points in the $\sigma_{xx} - \sigma_{xy}$ flow lines, so that we can take the points, $\sigma_{xy} = 1/(\rho_{xx}^2 + \rho_{xy}^2) = (N + 1/2)e^2/h$, as boundaries up to which the QHE effect survives when the strength of disorder is increased (Fig.24(b)).

It is also important to consider how the QHE in strong magnetic fields crosses over to the situation of weak magnetic fields, since all the states should become localised in the limit of

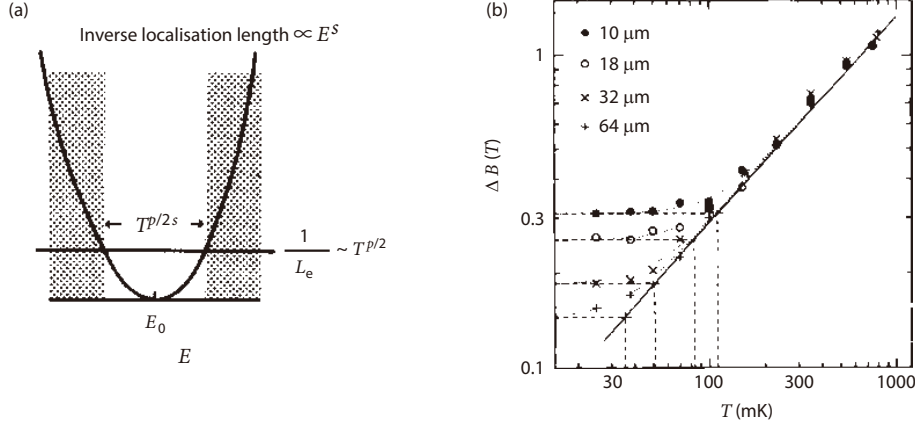


Figure 23: (a) In a theoretical plot for the inverse localisation length against energy, the effectively extended states (white region) is shown for the inelastic scattering length L_e at a given temperature T [after H. Aoki and T. Ando, Surf. Sci. **170**, 249 (1986)]. (b) An experimental result for the plateau-to-plateau transition width ΔB on the B axis plotted against T for various values of the sample size [after S. Koch et al, Phys. Rev. Lett. **67**, 883 (1991)].

$B \rightarrow 0$, so that the fate of the delocalised states is quite nontrivial. It has been suggested that the energies corresponding to the delocalised states go up in energy, which is called the “floating”.

Another question of heuristic interest is what is the classical limit (i.e., Planck’s constant $\hbar \rightarrow 0$). In this limit the Landau level filling $2\pi\ell^2 n = (h/eB)n$ vanishes for a fixed n . The measure of the Landau level mixing, on the other hand, is the Landau level broadening divided by the cyclotron energy, $\Gamma/\hbar\omega_c \sim 1/\sqrt{\omega_c\tau_0}$. Since $\Gamma/\hbar\omega_c$ diverges like $1/\sqrt{\hbar}$ for $\hbar \rightarrow 0$ with fixed B and τ_0 , the classical limit amounts to a regime of dilute filling $\nu(\propto \hbar)$ in weak magnetic fields.

5.3 Fractal wavefunctions and dynamical scaling

It is an intriguing question to ask whether a transition between localised and extended states, in general, is similar to phase transitions in statistical mechanics. A suggestion came in 1983 by Aoki to the effect that the wavefunction at the Anderson transition, where a characteristic length scale is absent with the diverging localisation length, should be self-similar (fractal), [28] just as the critical point in a phase transition is characterised by scale-invariant states with a diverging correlation length.

For the QHE system in particular, the transition point occurs at the centre of each Landau level, so that the delocalised states at the centre of a Landau level are just not the usual extended states, but fractal (or sometimes called critical) wavefunctions $\psi(\mathbf{r})$ that have a fractal dimensionality, $d^* < 2$. In other words, the density autocorrelation decays with a power law, $\langle |\psi(\mathbf{r})\psi(\mathbf{r} + \mathbf{R})|^2 \rangle \sim 1/R^{2-d^*}$. Typical wavefunctions in Fig.25, which are obtained numerically for larger sample sized than in Fig.16, show that the wavefunction is indeed scattered both in amplitude and spatial extent.

To be more precise, the self-similarity in critical wavefunctions extends beyond a single scale

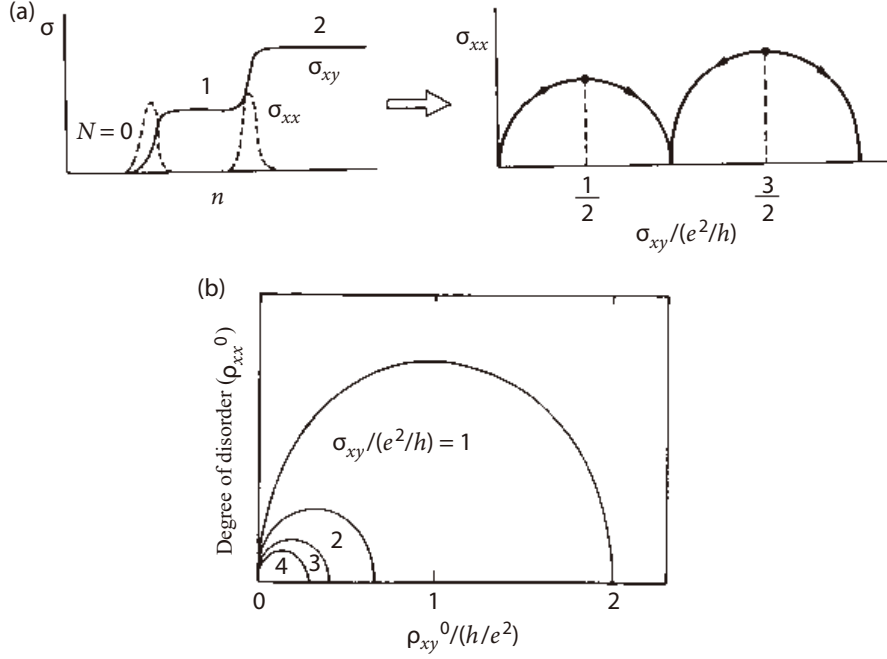


Figure 24: (a) How a σ_{xx} - σ_{xy} diagram is obtained from their n -dependence is schematically shown, with the flow lines bifurcating at $\sigma_{xy}/(e^2/h) =$ half integer indicated. (b) The global phase diagram, against the Hall resistivity ρ_{xy} and the longitudinal resistivity ρ_{xx} (the latter being a measure of the degree of disorder).

transformation, so the idea has been subsequently developed into the multifractal analysis, with which we can analyse the delocalised states around the Landau level centre.[26, 29] As described in the section below, real-space imaging such as STM can visualise such states.

Among the physical quantities that are affected by the fractality of the wavefunctions is the “anomalous diffusion” in transport. Namely, the dc conductivity σ obeys, in ordinary systems, Einstein’s relation, $\sigma = \lim_{\mathbf{q}, \omega \rightarrow 0} \mathbf{q}, \omega \sigma(\mathbf{q}, \omega) = e^2 D(E_F) \mathcal{D}_0$ where \mathcal{D}_0 is the diffusion constant. For the \mathbf{q}, ω -dependent conductivity $\sigma(\mathbf{q}, \omega)$, the dynamical scaling ansatz asserts that the ac conductivity should depend on $\omega\tau$, where the relaxation rate goes to zero like $1/\tau \sim 1/\xi^z$ around the transition. Here z is the dynamical critical exponent, which is usually 2 in noninteracting systems. If we combine this with the sample size scaling in L/ξ , the \mathbf{q}, ω -dependence should take a form,

$$\sigma(\mathbf{q}, \omega) \sim e^2 D(E_F) \mathcal{D}(q/\omega^{1/z}). \quad (36)$$

At the criticality the fractality of the states is shown to lead to $\mathcal{D}(q/\sqrt{\omega}) \sim \mathcal{D}_0/(q/\sqrt{\omega})^\eta$ with $\eta = 2 - d^*$. For a dynamical scaling for graphene, see [30]

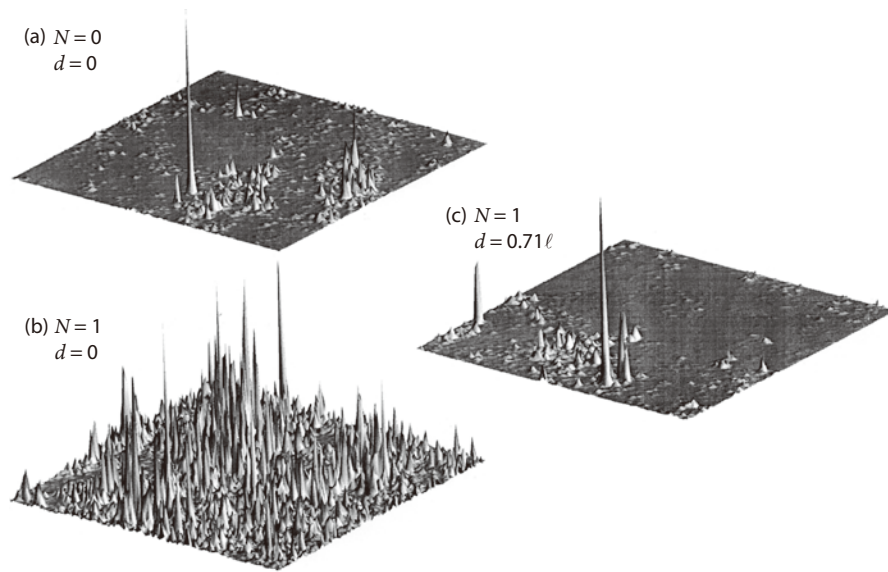


Figure 25: Typical wavefunctions (represented as their squared amplitude) around the centre of each Landau level obtained in a computer simulation for a disordered QHE system with a system size of $300\ell \times 300\ell$ for (a) $N = 0$ and (b) $N = 1$ Landau levels with short-range scatterers, and for (c) $N = 1$ with long-range ($d \neq 0$) scatterers [after T. Terao et al, Phys. Rev. **54**, 10350 (1996)].

6 QHE edge states and edge transport

6.1 Bulk-edge correspondence

The role of sample edges in the QHE transport has been an issue of interest from an early stage when the problem was raised by Halperin in the 1980's.[31] Classically, there are edge currents that correspond to cyclotron motions skipping along the edges (Fig.26(b)). Quantum mechanically, edge states also exist (Fig.26(a)). The energy diagram plotted against the real-space position across the sample width will look like Fig.27(a). Edge states (or, in a broader context, boundary states in field theory) are ubiquitous in quantum mechanics, but the peculiarity in the QHE is that the edge currents flow in a definite direction dictated by the direction of the applied magnetic field (hence they are dubbed chiral edge currents), with no backscattering even when the edge is e.g. rugged. When one takes the electron-electron interaction into account, the edge states may be regarded as special, incompressible electronic states called the chiral Tomonaga-Luttinger liquid, as discussed in the context of the fractional QHE.

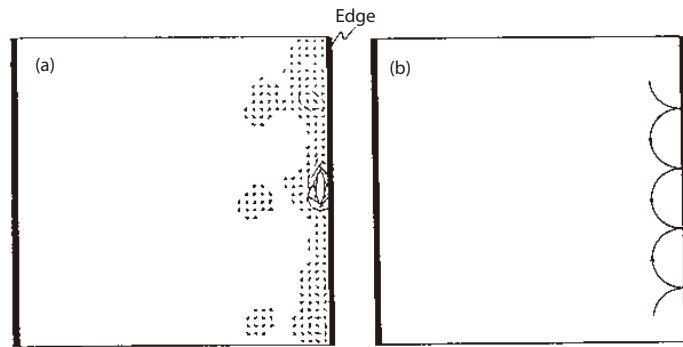


Figure 26: Typical edge states in (a) a QHE system in quantum mechanics in a simulation for a finite system, here represented by the current distribution $\mathbf{j}(\mathbf{r})$ with arrows, and (b) in classical mechanics [after H. Aoki, in G. Landwehr (ed.): *Application of High Magnetic Fields in Semiconductor Physics* (Springer, 1983), p.11].

In terms of the topological nature of the QHE, the appearance of edge states is a prime example of a general concept of the “bulk-edge correspondence” as introduced by Hatsugai,[32] i.e., in topological systems, the nature of edge states are dictated by the nature of bulk states, as in the boundary states in field theories. In a finite QHE sample, the edge states appear on the energy spectrum as the edge modes that cross from one Landau level to another in a Landau gap. These modes have to exist, as sometimes called “topologically protected”, in QHE systems. In a broader context, topological boundary states arise as we have displayed on the classification of topological systems in Fig.3.

The topological nature of the QHE edge states manifests itself, as shown by Hatsugai, in the properties that (i) the edge Hall conductivity is also expressed as a topological invariant (Chern number), and (ii) this quantity exactly coincides with the topological Chern number for the bulk Hall conductivity.[32] Alternatively we visualise, in Fig.27(b), that we can continuously change the situation from the edge-picture limit (where currents exist only at edges) to the bulk-picture (where a bulk potential gradient exists) when the current distribution is deformed, but there is

always the total current conservation, $I^{\text{bulk}} = I^{\text{leftedge}} - I^{\text{rightedge}}$, which implies $\sigma_{xy}^{\text{bulk}} = \sigma_{xy}^{\text{edge}}$. [33]

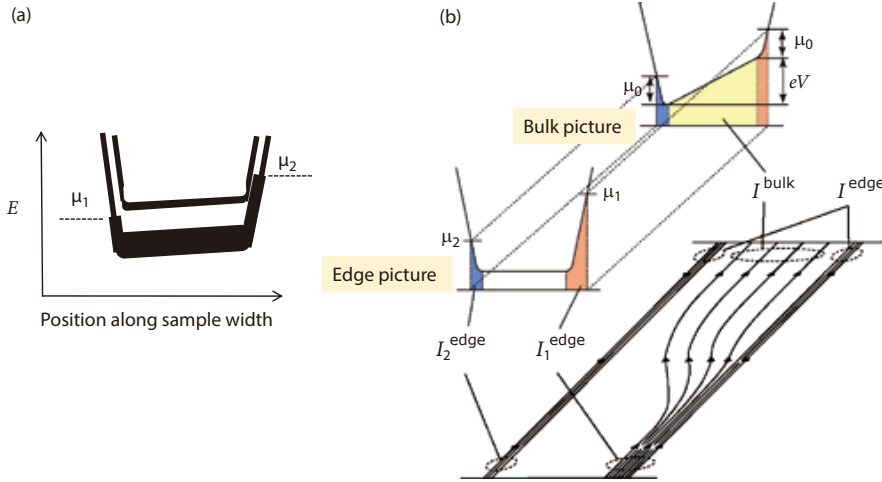


Figure 27: (a) Energy spectrum against the position along the width is schematically shown for a sample with edges with the chemical potential at the left edge (μ_1) and at the right (μ_2). (b) How the edge picture (in which all the currents are carried by edge states) continuously crosses over to the bulk picture (where a bulk contribution exists) is schematically shown [after M. Koshino, H. Aoki and B.I. Halperin, Phys. Rev. B **66**, 081301(R) (2002)].

One way to describe the edge transport is Büttiker's formula [34], which is an extension of Landauer's formula for transport processes in terms of an S matrix for transmission and reflection channels in ballistic transports. Büttiker's formula can explain some of the experimental results, including the quantisation of the Hall conduction. However, this does not mean that all the QHE currents are carried by edges. In general there exist both bulk and edge Hall currents. Bulk and edge states can even be hybridised. The details have been studied experimentally and theoretically, which largely indicate that there are contributions from both bulk and edges, whose proportions depend on the width of the sample, T -dependent σ_{xx} , etc.

Physically, a macroscopic system may be regarded as comprising subsystems each having a linear dimension of the phase coherence length L_ϕ . The transport is described by the Kubo-formula σ_{xx}, σ_{xy} if the sample size is much greater than L_ϕ where the Hall field and Hall current distributed over the sample, while the edge transport ala Büttiker starts to dominate when the size is shrunk to $\sim L_\phi$.

One of the characteristic features in the edge transport is that highly nonlocal phenomena can arise that extend over length scales far exceeding the bulk mean free path. This can be probed in multi-terminal Hall-bar samples by injecting currents from some contacts, where the conductance can strongly depend on which terminals to select for its measurement.

The width of edge states in real space have experimentally been measured with various methods including transport (e.g. QHE breakdown), magnetocapacitance, and magnetoplasmon measurements. We can also utilise the nuclear spins. Usually, the nuclear spins are irrelevant to electron systems, since the nuclear Zeeman energy is as small as 1/2000 of the electronic counterpart. When there are almost degenerate electronic states, however, nuclear spins can affect the electron system via the hyperfine interaction. This occurs in the fractional

QHE systems close to a spin-polarisation transition, but also in the integer QHE where left and right edge states are degenerate in energy, so that the nuclear spin is probed via the scattering between the left and right edge channels.

In semiconductor superlattices, which realises a stack of 2DEG's, an application of a strong magnetic field along the growth direction makes the system a stack of IQHE systems. There, the edges states are also stacked along the edge surfaces, which is called 'sheath currents' and have been experimentally observed.

6.2 Real-space imaging

Experimentally, there have been a body of studies for real-space imaging of the QHE systems, including the Hall field. Fontein et al[35] have studied a potential profile imaging with the electro-optical effect (which utilises the birefringence (Pockels effect) where the phase difference between different polarisations probes the potential) to show that an electric field exists over the whole sample although the field becomes stronger towards the edges as shown in Fig. 28.[36] There are various other methods as well, including scanning capacitive, force and polarisation optical microscopies,[37] the imaging with a metal single-electron transistor (SET)[38], and the microwave impedance microscope[39] .

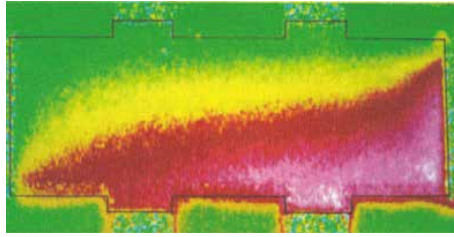


Figure 28: A typical real-space image for the potential distribution (colour-coded from blue to red with increasing potential) obtained with the electro-optic imaging for $B = 10.8$ T that corresponds to the centre of a plateau. Black line delineates the Hall bar system [after R. Knott et al, *Semicond. Sci. Tech.* **10**, 117 (1995)].

One such probing, that is particularly suited to examine nonequilibrium carriers around the “hot spots”, is the imaging of cyclotron emission due to Komiyama and coworkers.[40] In a Hall-bar sample in the QHE condition (with $\sigma_{xx} = 0, \sigma_{xy} \neq 0$), the electric lines of force are forced to be distorted to make the rectangular sample geometry compatible with the Hall angle of 90 degrees, which results in singularities appearing around two corners across the opposite electrode (Fig.29(a)). These are called the hot spots. In imaging the cyclotron emission (Fig.29(b)), the QHE detector, which is itself an IQHE system having by nature sensitive photoresponses at the cyclotron resonance frequency, is used to scan the QHE system. The imaging captures the hot spots clearly, with edge channel also visible for the Landau level filling \neq integer. The imaging of cyclotron emission has also been used to examine the breakdown of QHE (see Section ‘Breakdown of QHE’).

Scanning tunnelling microscopy (STM) and scanning tunnelling spectroscopy (STS) are also performed, for a special kind of adsorbate-induced 2DEG with e.g. Cs atoms deposited on cleaved n-InSb that makes STM/STS feasible. The STS imaging can also directly observe the quantum Hall transition from one localised regime to another via the delocalised states that have a fractal character as shown in Fig.30.[41]

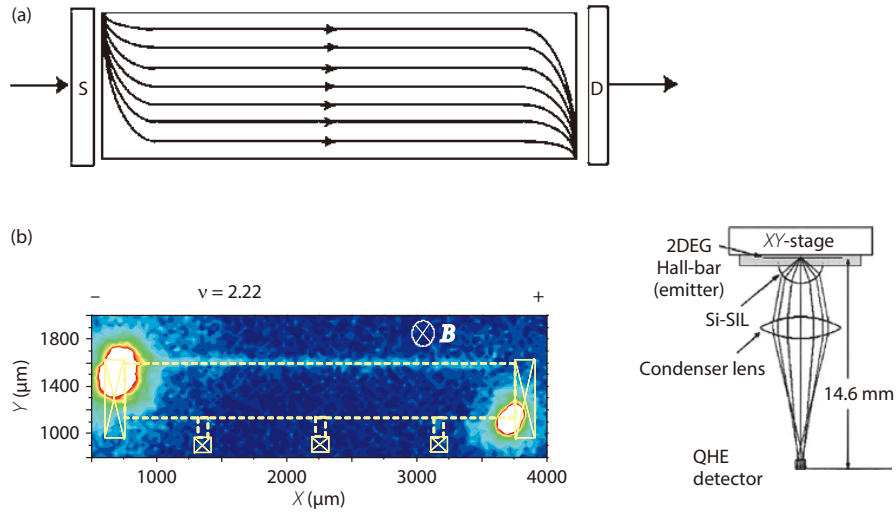


Figure 29: (a) The electric lines of force are schematically shown for the QHE condition, with source (S) and drain (D) electrodes. (b) A real-space imaging for a Hall bar sample (delineated by yellow lines) obtained with the cyclotron emission as detected by the QHE device (inset) [after K. Ikushima et al, Phys. Rev. Lett. **93**, 146804 (2004)].

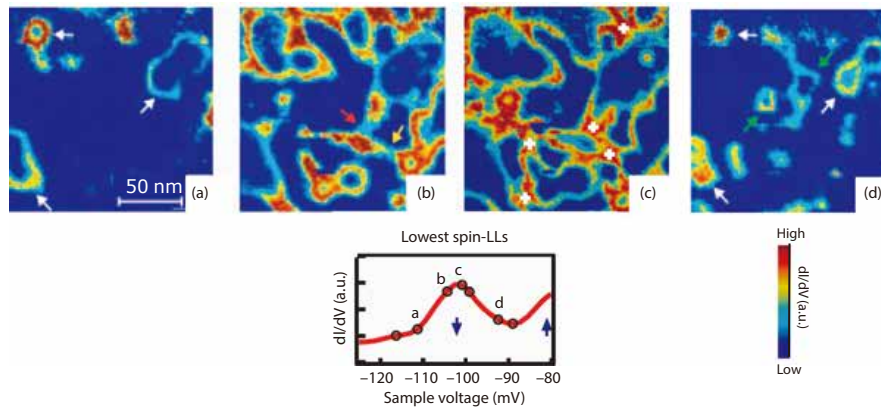


Figure 30: A real-space image obtained by STS for 0.01 monolayer of Cs on a cleaved n-InSb(110) at $T = 0.3$ K for various values of the Landau level filling, (b)-(f), as indicated in inset [after K. Hashimoto et al, Phys. Rev. Lett. **101**, 256802 (2008)].

7 QHE resistance standard, the fine-structure constant and new SI

After the recognition that the accuracy of the QHE quantisation is experimentally better than 10^{-6} initially and even refined to 10^{-7} , it was decided, in 1990 by CIPM (Comité International des Poids et Mesures), that the QHE be adopted as the electrical resistance standard, with which ohm is defined via the QHE resistance as

$$R_K(\equiv h/e^2) = 25\,812.807\,\Omega, \quad (37)$$

where R_K is called the von Klitzing constant.

The constant, now adopted as the resistance standard, has a profound significance related with a fundamental physical constant. Namely, the fine-structure constant (in cgs),

$$\alpha = \frac{e^2}{\hbar c} \simeq 1/137.036, \quad (38)$$

which is the coupling constant in the QED (quantum electrodynamics) [42] and one of the most basic physical constants, is directly related with R_K via $\alpha = 2\pi/R_K c$. Here $c = 2.99792\dots \times 10^8$ m/s, the speed of light in vacuum, is, in SI, a defined value. Figure 31(a) displays the measured values of α obtained by various methods including that from R_K obtained in various institutes. If we combine R_K with the Josephson constant, $K_J = 2e/h$, we can deduce the value of Planck's constant via $h = 4/K_J^2 R_K$ (Fig. 31(b)). For a review, see[43].

Recently, BIPM (Bureau International des Poids et Mesures) decided that the International System of Units (Système International d'Unités, abbreviated as SI) are defined, from 20 May 2019, in terms of designated fixed numbers as:

- $\Delta\nu$: The ground-state hyperfine transition frequency of ^{133}Cs is 9192631770 Hz.
- c : The speed of light in vacuum is 299 792 458 m/s.
- h : The Planck constant is $6.62607015 \times 10^{-34}$ J·s.
- e : The elementary charge is $1.602176634 \times 10^{-19}$ C.
- k : The Boltzmann constant is 1.380649×10^{-23} J/K.
- N_A : The Avogadro constant is $6.02214076 \times 10^{23}$ mol $^{-1}$.
- K_{cd} : The luminous efficacy of monochromatic radiation of frequency 540×10^{12} Hz is 683 lm/W.

Kibble balance (formerly known as Watt balance) can make a connection between the Planck constant and the kilogram, since we have

- h/e^2 from QHE,
- h/e from Josephson effect,

- $m_e = 2R_\infty h / (c\alpha^2)$: electron mass, where R_∞ : Rydberg constant, $\alpha = e^2 / (2\varepsilon_0 h c) = \mu_0 c e^2 / (2h)$: fine-structure constant with a CODATA-recommended value of $1/[137.035999084(21)]$, and ε_0 : permittivity of vacuum, $\mu_0 = 1/(\varepsilon_0 c^2)$: permeability of vacuum.

The kilogram, for instance, can be expressed as $[\text{kg}] = [\text{Hz}][\text{J} \cdot \text{s}]/[\text{m/s}]^2$, which can be defined in terms of $\Delta\nu, c, h$ defining respectively Hz, m/s, and J·s. For the von Klitzing constant, $R_K = h/e^2 = \mu_0 c / (2\alpha) = 25812.807 \ \Omega$, μ_0 (with dimension $[\text{N}/\text{A}^2]$) and c [m/s] have fixed values in the new SI, so that a measured uncertainty in R_K translates to the uncertainty in α . Experimentally, the universality (relative accuracy in sample and material dependence) of the constant has been experimentally shown to be as small as $\sim 10^{-10}$. The inset of Fig.26 is the logo for the new SI by BIPM. See an article, K. von Klitzing, Nature Phys. **13**, 198 (2017).

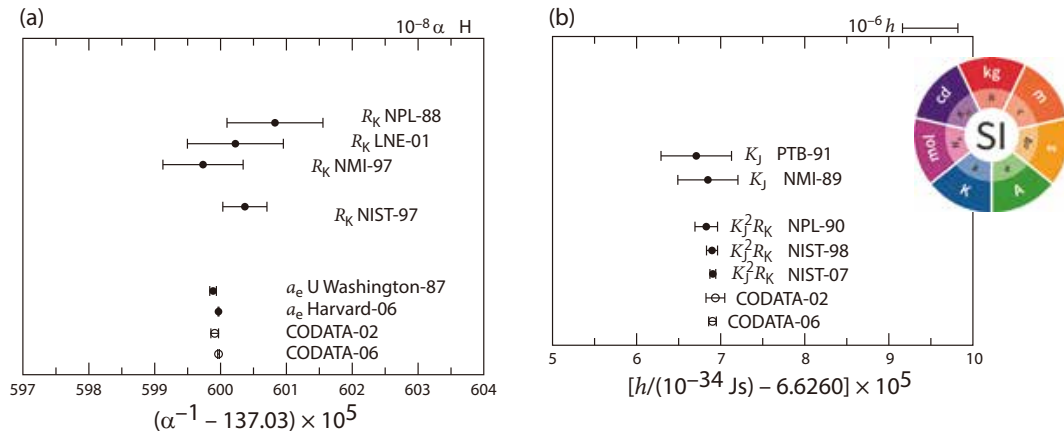


Figure 31: (a) Values of the fine-structure constant α obtained with various methods. Those marked with R_K are from the QHE measurements in various institutes, while a_e from the electron magnetic moment anomaly. (b) A similar plot for Planck's constant h . CODATA-recommended values are also indicated. After P. J. Mohr et al, Rev. Mod. Phys. **80**, 633 (2008). The inset is the logo for the new SI (the International System of Units) by BIPM (from <https://www.bipm.org/en/measurement-units>).

8 Breakdown of QHE

When we increase the source-drain voltage to increase the source-drain current in Hall measurements in the Hall-bar geometry, the longitudinal resistance R_{xx} , which is close to zero in the QHE plateau region, abruptly increases for sufficiently large voltages, as typically shown in Fig.32. This is accompanied by disrupted plateau structures in R_{xy} . Thus the Hall current, which is originally dissipationless in the QHE condition, becomes dissipative for large enough voltage, and this phenomenon, known from an early stage of the QHE studies, is called the breakdown of QHE. The breakdown is important from both applicational aspects (since it affects the accuracy of the QHE), and fundamental aspects since this is an interesting nonequilibrium phenomena. Several factors can be involved, among which are tunnelling between different Landau orbits or Landau levels, and/or electron heating effect. Also relevant is how the breakdown is related with the current profile in real space in a Hall bar. A review on experimental and theoretical results may be found, e.g., in [44]. Sometimes metastable or bistable states are observed around the breakdown regime, which is also of interest. As for nonequilibrium phenomena, we can mention that the microwave-induced magnetoresistance oscillation, although this occurs in a weak magnetic field regime rather than in the QHE regime.[45]

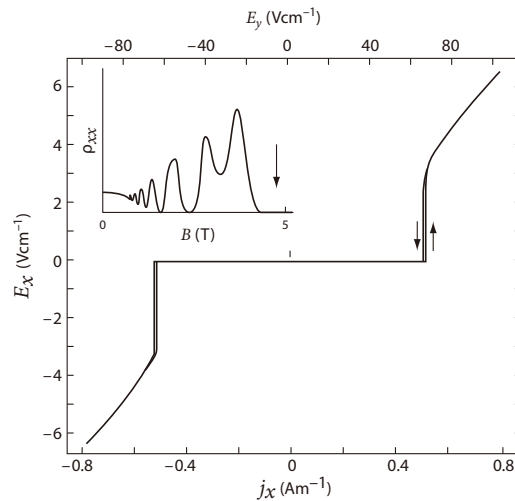


Figure 32: A typical current-voltage characteristics at $\nu = 2$ (thick arrow in the inset) [after G. Nachtwei, Physica E **4**, 79 (1999)].

9 Quantum dots and periodically modulated systems in strong magnetic fields

9.1 Quantum dots in magnetic fields

Semiconductor quantum dot is a nanostructure that confines a small number of electrons. The physics of quantum dots is a very wide area, so here we only mention its relevance to QHE. Quantum dots are usually fabricated by applying a lateral confining potential to a 2DEG system. This can be realised either by an electrode that exerts an electrostatic confining potential, or alternatively we can mesa-etch the system to have a finite system (Fig.33(a)). The confining potential is usually cylindrically parabolic to a good approximation.

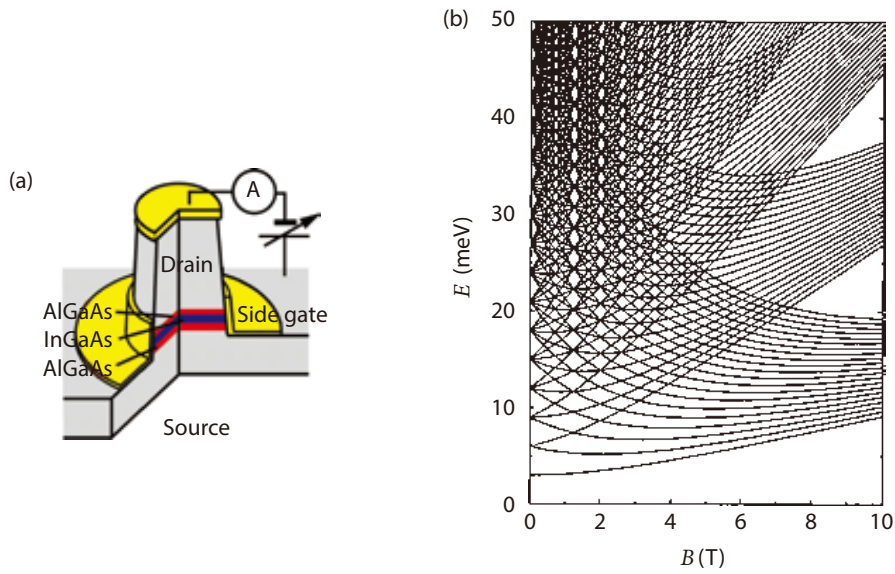


Figure 33: (a) A typical mesa-etched quantum dot structure [after P. A. Maksym et al, Phys. Rev. B **79**, 115314 (2009)]. (b) Energy levels of the Fock-Darwin states against magnetic field for a harmonic confinement [after P. A. Maksym et al, J. Phys. Condensed Matter **12**, R299 (2000)].

Quantum dots are investigated in strong magnetic fields as well. In a magnetic field, $\mathbf{B} = \text{rot}\mathbf{A}$, applied perpendicular to the dot plane the Hamiltonian in the one-body problem reads

$$\mathcal{H} = \frac{1}{2m^*} [\mathbf{p}_i + (e/c)\mathbf{A}(\mathbf{r})]^2 + \frac{1}{2}m^*\omega_0^2r^2, \quad (39)$$

where $\hbar\omega_0$ is the confinement energy for a parabolic potential, and we have ignored the Zeeman energy.

The exact eigenstates of this Hamiltonian are known as the Fock-Darwin states, since they were first investigated by Fock and Darwin in the 1920's. They are given, up to a normalisation constant, as

$$\psi_{nm}(\mathbf{r}) = r^{|m|} L_n^{|m|}(r^2/2\lambda^2) \exp(-r^2/4\lambda^2) e^{-im\theta} \quad (40)$$

in 2D polar coordinates with eigenenergies given by $E_{nm} = (2n + 1 + |m|)\hbar\Omega - m\hbar\omega_c/2$. Here m is the angular momentum, n a radial quantum number, $L_n^{|m|}$ the associated Laguerre polynomial, $\Omega^2 = \omega_0^2 + \omega_c^2/4$ with the cyclotron frequency $\omega_c = eB/m^*$. Thus the wavefunction is almost the usual Landau's wavefunction when the confinement potential is parabolic, where the difference is in the length parameter, $\lambda = \sqrt{\hbar/(2m^*\Omega)}$. In Fig.33(b) depicting the energy levels we can indeed see that a crossover from the states of a 2D harmonic oscillator in the zero magnetic field limit to the Landau states in the strong field limit. When we consider the electron-electron interaction, a variety of states emerge, which include the maximum-density droplet that corresponds to the Landau level filling $\nu = 1$, and the electron-molecule states. [46]

So the dots in strong magnetic fields are a kind of confined QHE systems, or artificial atoms in magnetic fields. Their properties have been extensively studied with various methods. For instance, dot wavefunctions have been probed experimentally with techniques such as magneto-tunnelling spectroscopy. Other properties include magnetocapacitance, electron addition spectra and transport spectra in magnetic fields, from which the ground-state quantum numbers are deduced. Dot arrays have also been studied in the QHE regime, where resonant scattering effects etc have been reported.

9.2 Hofstadter spectrum

What happens to QHE when we have periodic systems rather than a translationally invariant 2DEG? Condensed-matter physics tells us that in a periodic system we have Bloch's theorem, which dictates that electronic states for periodic systems are dominated by Bragg's reflection, resulting in band structures and Bloch states. So, when we apply an external magnetic field, we are talking about Landau's quantisation in the presence of Bragg's reflection. We can realise that Bragg's reflection and Landau's quantisation interfere with each other, since the application of a magnetic field, $\mathbf{B} = \text{rot}\mathbf{A}$, gives rise to, semiclassically, the Peierls phase, $\exp(-i\frac{e}{\hbar} \int^{\mathbf{r}} \mathbf{A}(\mathbf{r}') \cdot d\mathbf{r}')\psi(\mathbf{r})$, in the wavefunction ψ . Landau's quantisation in periodic and lattice systems was first considered by Wannier and by Hofstadter[47]. It has been shown that the energy spectrum plotted against magnetic field is a curious fractal (sometimes called Hofstadter's butterfly). Fractal, because each Landau level splits into p levels when the magnetic flux within a unit cell in units of flux quantum equals to a rational number q/p .(Fig.34)

When E_F is in one of these gaps, we should have IQHE, for which σ_{xy} in units of e^2/h , the Chern number, can be calculated with the topological TKNN formula.

Recent advances in the electron beam lithography has made it possible to fabricate 2DEG's with 2D periodic modulations, and the butterfly was observed.[48]

Hofstadter's problem has been examined not only in condensed-matter systems, but also in cold-atom systems with greater experimental controllability[49, 50]. The bulk-edge correspondence (as described in that Section) in the Hofstadter problem has in fact been confirmed in cold-atom systems.[51]

A recent important addition to the Hofstadter-butterfly systems is the superstructures realised as the Moiré pattern in twisted bilayer graphene[52], and the butterfly was actually observed in 2021 in twisted bilayer graphene at a magic twist angle.[53] . We shall describe this in Section 'Twisted bilayer graphene' below.

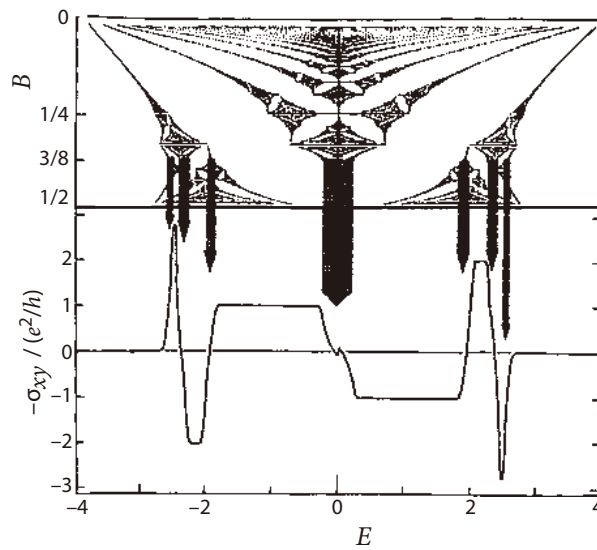


Figure 34: Top: Hofstadter butterfly (energy spectrum, against magnetic field B measured by the flux penetrating a unit cell) for a square lattice. Bottom: QHE for a square lattice exemplified for a magnetic flux in a unit cell of the periodic system being $3/8$ in units of the flux quantum [after H. Aoki, in G. Landwehr (ed.): *Application of High Magnetic Fields in Semiconductor Physics III* (Springer, 1991), p.17].

9.3 QHE in three dimensions

While usually the QHE is inherent in two-dimensional (2D) systems, we can raise a question: can we conceive a similar effect in three-dimensional (3D) systems, and, if so, how? If we recall the adiabatic argument for topological properties, we essentially exploit the presence of inter-Landau-level gaps in the energy spectrum. This implies that, if there exist, for some reason, energy gaps in 3D systems in magnetic fields, we may have a quantisation when E_F is in a gap, as pointed out already in the 1980s and 1990s by Avron et al, and by Halperin et al.[54] Note that for 3D we are talking about the Hall conductance R_{xy}^{-1} rather than the Hall conductivity, since for d -dimensional systems of size L the conductance R^{-1} and conductivity σ are related as $R_{xy}^{-1} = L^{d-2}\sigma_{xy}$, so that only in 2D do they happen to coincide with each other.

Usual wisdom, however, is that gaps do not tend to appear in 3D. One possibility is to use 3D systems that have periodic structures or potentials. Koshino et al have shown that 3D Hofstadter spectra can appear in periodically modulated structures in the energy spectrum against the tilting angle in tilted magnetic fields, where an interference of Landau's quantisations due respectively to the components B_y and B_z of the magnetic field is responsible (as compared with 2D where Hofstadter's butterfly comes from an interference between Bragg's reflection and Landau's quantisation).[55] Then each of σ_{xy} and σ_{zx} are quantised when E_F is in each gap with the current $\mathbf{j} = -\boldsymbol{\sigma} \times \mathbf{E}$ where $\boldsymbol{\sigma} = (\sigma_{yz}, \sigma_{zx}, \sigma_{xy})$ (Fig. 35).

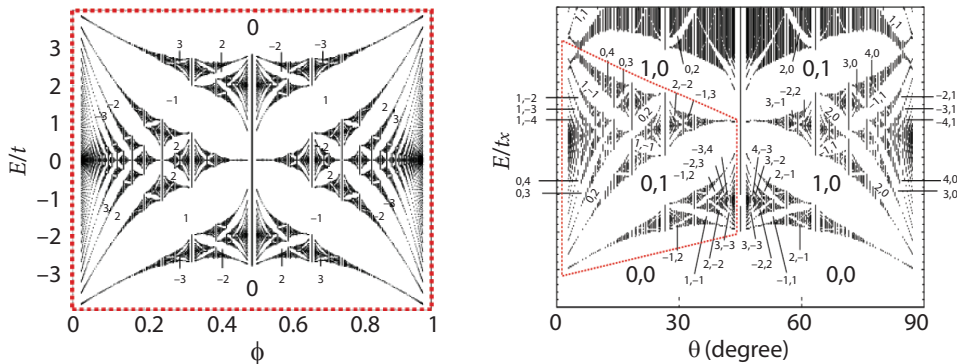


Figure 35: Right: Energy spectrum against the tilting angle, θ , of the magnetic field applied to a three-dimensional, periodic system. The QHE values (in units of e^2/ah with a : lattice constant) for $(\sigma_{xy}, \sigma_{zx})$ are indicated by a pair of numbers attached to each gap in the spectrum. The region indicated by a dashed line has a one-to-one correspondence to the Hofstadter butterfly (E vs magnetic flux ϕ within a unit cell) in 2D (left panel) [after M. Koshino et al, Phys. Rev. Lett. **86**, 1062 (2001)].

A kind of Landau quantisation has been known to occur in an anisotropic organic conductor (TMTSF in the Bechgaard salt family). This occurs for the field-induced spin-density wave (SDW) in strong magnetic fields with a many-body origin. Namely, the Landau quantisation takes place within the pockets formed by incompletely-nested Fermi surfaces, which gives rise to a series of gaps around the main SDW gap, and an associated QHE in 3D.[56]

10 Anomalous quantum Hall effect and spin quantum Hall effect

QHE has close relatives in the anomalous Hall effect and the spin Hall effect (Fig.36), so let us briefly describe them in relation to the IQHE. While the QHE is a topological phenomenon generic to 2DEG, the anomalous Hall effect (Hall effect in ferromagnetic materials) and the spin Hall effect (Hall effect for the spin degrees of freedom in materials that have strong spin-orbit interactions) arise from system's magnetic structure, band structure and interactions, so they occur in three-dimensional systems as well.

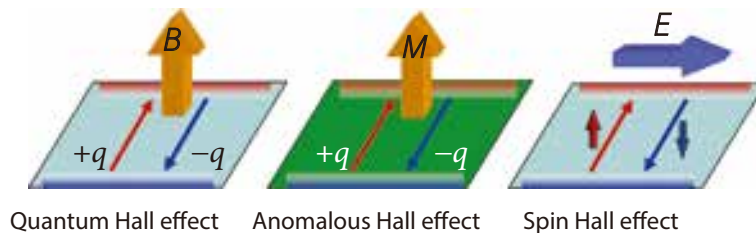


Figure 36: Quantum Hall effect, anomalous Hall effect, and spin Hall effect are schematically shown. $\pm q$ stands for the charge of a carrier.

In the anomalous Hall effect in metallic ferromagnets, the Hall resistivity is expressed as

$$R_H = R_{\text{normal}}B + R_{\text{anomalous}}M \quad (41)$$

with R_{normal} being the normal Hall resistivity, B the external magnetic field, $R_{\text{anomalous}}$ the anomalous Hall resistivity and M the magnetisation of the material. In this effect, the Hall current flows even in zero external magnetic fields. Theoretical analysis was initiated in the 1950's by Karplus and Luttinger as a (multi-)band effect in the presence of spin-orbit interaction. To be more precise, two mechanisms have been identified, one (called extrinsic) is the skew scattering + side jump by impurities when both of spin-orbit interaction and magnetisation are present, and the other (called intrinsic) is Berry's-curvature contribution to the Hall conductivity as in the QHE, which is included in the linear-response formula. Experimentally, the anomalous Hall effect has been observed in various materials, typically $\text{Nd}_2\text{Mo}_2\text{O}_7$ with non-collinear spin configurations and $(\text{Sr,Ca})\text{RuO}$ compounds.

In the spin Hall effect, which also occurs in zero magnetic field, \uparrow spins and \downarrow spins flow in the opposite directions in an electric field (as opposed to the ordinary Hall effect in which opposite charges flow in the opposite directions in a magnetic field). This effect, which also comes from the spin-orbit interaction, is another topological effect. The effect, predicted in the 1970's, is later experimentally observed with e.g. Kerr rotation microscopy in both n- and p-type GaAs-based semiconductor heterostructures.

QHE, anomalous Hall effect and spin Hall effect are related in that they are manifestations of the phase of the wavefunctions in magneto-transport properties. An intimate relation between QHE and the spin Hall effect has been brought home by a more recent "quantum spin Hall effect" (QSHE)[57, 58] which was predicted originally for graphene. The idea starts as follows. Graphene is described, as we shall describe in Section 'QHE in graphene', by a Dirac equation

for two spatial dimensions around each of K and K' valleys in the Brillouin zone, where the two valleys are distinguished by a pseudospin τ_z . In the presence of a spin-orbit interaction, we have an extra term that couples the real spin and the pseudospin, and this gives rise to an energy gap (a mass gap in the language of the Dirac theory), as proposed by Kane and Mele,[59]. The coupling between the real and pseudospins is related, as mentioned by Kane and Mele, to a model introduced by Haldane in 1988[105] for the quantum anomalous Hall effect (QHE in zero external field), for spinless electrons but with spatially structured magnetic fluxes. The gap is a topological gap, where the gapped state cannot indeed be reached by an adiabatic change of the system, so that the insulator is called a topological insulator. Since the bulk is topological, the edge states have to exist and called topological edge states. In this respect the QSHE is distinct from the spin Hall effect, and the whole situation is rather similar to the IQHE, where an essential difference is that the edge states carry charges in IQHE while edge states carry spins in the QSHE. The energy dispersion (Fig. 37) of the edge states in a QSHE system, which may be thought of as arising from Kramers' doublets, is gapless with the two dispersion crossing at a point in the Brillouin zone. The conductivity calculated with the linear-response theory for each of the spin-up and spin-down electrons gives a quantised (Chern number) conductivity, where the directions of the current are opposite between the up and down spins, with a quantised spin Hall conductivity shown to be $\sigma_{xy}^{\text{spin}} = e/2\pi$. QSHE belongs to Class AII (symplectic) in Figs.1,2. We shall come back to Haldane's model(Fig.56) in Section 'Floquet topological insulator'.

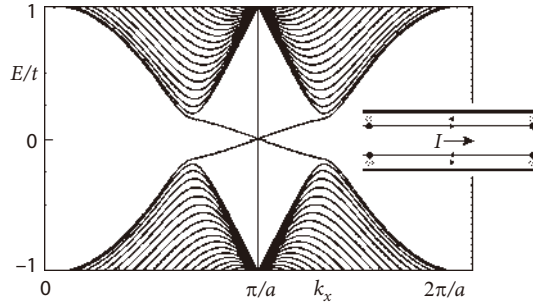


Figure 37: Energy spectrum for a system that exhibits quantum spin Hall effect. Bunch of lines represent bulk states, while a pair of isolated lines the edge states. Inset shows how the spin-up and spin-down electrons flow in real space. [after C. L. Kane and E. J. Mele, Phys. Rev. Lett. **95**, 226801 (2005).]

While the original proposal due to Kane and Mele[59] was made for graphene, the material has too small a spin-orbit interaction. Subsequently, the effect was shown to be realised in quantum wells with narrow-gap semiconductors, HgTe/CdTe.[60] While both of HgTe and CdTe have zinc-blende crystal structure, their band structures are affected by the spin-orbit interactions in significant ways. Namely, the bulk HgTe has a band structure called “inverted”, since a band that usually forms the valence band is pushed above another band that usually forms the conduction band, where the former consists of two (heavy- and light-mass) bands that touch with each other at a point in the Brillouin zone with opposite curvatures (i.e., the bulk system is a semimetal). While IQHE (Fig.38) was observed in HgTe/CdTe quantum wells and superlattices grown by MBE, the QSHE itself was then detected. The band structure behind

this is, when HgTe is sandwiched between CdTe to make a quantum well, the bands in HgTe well remain inverted for wide wells, while the bands become normal for thin enough wells. So the well thickness can act to control the presence or otherwise of a mass gap, and the system should be a quantum spin Hall insulator above a critical thickness. With the spin Hall effects we can electronically manipulate the spin degrees of freedom, so that applications are explored, which is called the spintronics.

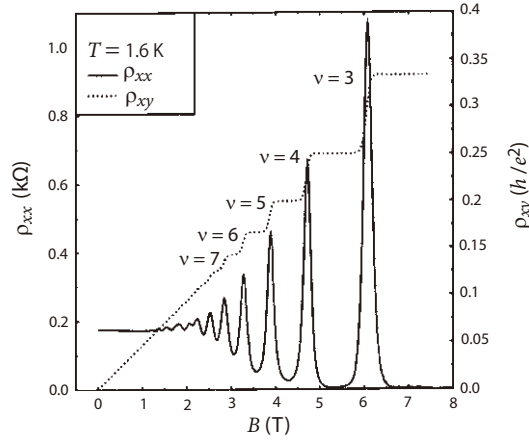


Figure 38: QHE in a HgTe quantum well [after A. Pfeuffer-Jeschke et al, Physica B **256-258**, 486 (1998).]

11 Integer vs fractional quantum Hall effects

The integer QHE has subsequently been developed into the fractional QHE (FQHE). In FQHE the Hall conductivity is quantised into $\sigma_{xy} = \nu e^2/h$ for fractional Landau level fillings $\nu = 1/3, 2/3, 3/5, \dots$ as opposed to the IQHE for $\nu = \text{integer}$. Let us compare the IQHE with FQHE in this section. Physically, the integer QHE is primarily understood in terms of a one-body problem as described in this chapter, while FQHE is inherently a many-body effect, and this is a customary way to distinguish the integer quantum Hall effect and FQHE. It is natural that the IQHE was originally discovered in Si-MOSFET, while the FQHE effect in GaAs-AlGaAs heterostructures, where the latter system is atomically much cleaner with typical mobility exceeding $\mu \simeq 10^6 \text{ cm}^2/\text{V} \cdot \text{s}$ against the former's $\sim 10^4 \text{ cm}^2/\text{V} \cdot \text{s}$. The FQHE has also been observed in clean enough SiMOSFET's.

One clear way to realise that the FQHE, a many-body effect, emerges as the degree of disorder is lowered is to look at the historical developments from IQHE to FQHE in Fig.39, which shows how the fractional effect appears as the sample quality (as characterised by the carrier mobility) becomes higher. In 2002 $\mu = 10 \times 10^6 \text{ cm}^2/\text{V} \cdot \text{s}$ is attained, where fractions observed include 6/25.[61] In the clean limit, the system is indeed in the limit of strong electron correlation in that the kinetic energy is quenched due to Landau's quantisation so that the ratio of the interaction energy to the kinetic energy is infinite (although more rigorously we have to consider the inter-Landau level matrix elements). While the FQHE is a new class of many-body states, the electron-electron interaction exists for integer fillings as well. In fact, an integer is a kind of fraction in that Laughlin's wavefunction for the FQHE liquid for clean systems, allowed for $\nu = 1/m$ with m an odd integer, also accommodates $m = 1$. So the real question is the nature of the energy gap: in the integer QHE the excitation gap is primarily the one-body gap between the adjacent Landau levels (or between the mobility edges in disordered systems), while the excitation gap in the FQHE has a many-body origin.

The relative weight of the one-body and many-body natures depends on the degree of disorder (and the g-factor in the case in which the adjacent Landau levels are Zeeman-split ones). To quantify this, we can examine the relevant energy scales. Figure 40 plots

(i) $\hbar\omega_c$ (the cyclotron energy),

(ii) $e^2/\epsilon\ell$ (typical size of the electron-electron Coulomb interaction),

where e is the elementary charge, ϵ (= 13 for GaAs) the dielectric constant of the material and ℓ the magnetic length, and

(iii) $g\mu_B B$ (the Zeeman energy),

where g is Landé's g-factor, $\mu_B = \hbar e/(2mc)$ the Bohr magneton. We can see that for $B \sim \text{few tesla}$ the Zeeman energy is relatively negligible, while the cyclotron energy and the Coulomb energy are comparable. For disordered systems we have to compare these with the Landau level broadening Γ , which is roughly estimated in the self-consistent Born approximation as $\Gamma/(\hbar\omega_c) \sim 1/(\omega_c\tau_0)^{1/2}$, where τ_0 is the scattering relaxation time in zero magnetic field. So the energy scale of disorder (Landau level broadening) becomes comparable with the cyclotron energy (\sim the Coulomb energy for $B \sim 10 \text{ T}$) for $\omega_c\tau_0 > \sim 1$.

While the two-dimensionality in IQHE appears in the fact that the Hall conductivity represents a topological quantum number (Chern number) in terms of the Berry's curvature, in FQHE the spatial dimensionality of two is essential in allowing, and indeed accommodating, such novel concepts as anyon quasi-particles with fractional statistics, and a description in

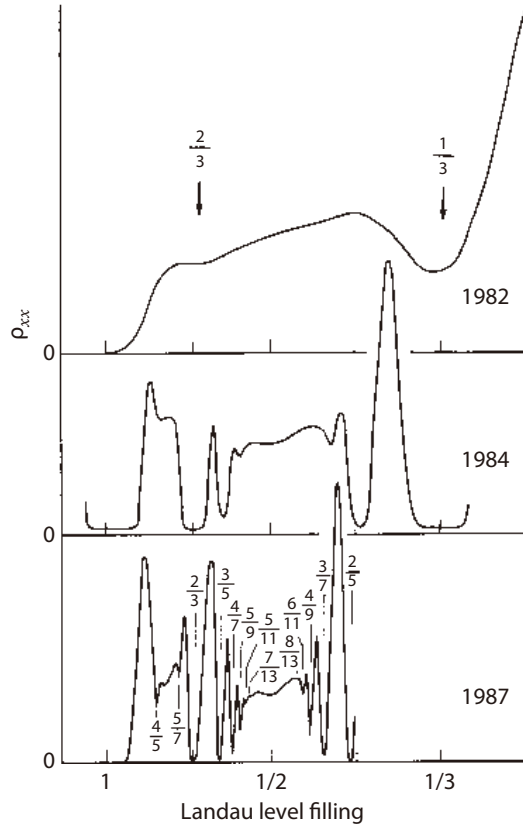


Figure 39: Developments of the fractional structure in samples of progressively higher quality [after D. C. Tsui et al, Phys. Rev. Lett. **48**, 1559 (1982), A. M. Chang et al, *ibid* **53**, 997 (1984), R. Willett et al, *ibid* **59**, 1776 (1987)].

terms of the composite fermion picture (i.e., a Chern-Simons gauge field theoretic treatment) of the many-body quantum liquid.

The relevant chapter should be referred to for the FQHE, so suffice it to mention here that FQHE can be regarded as an IQHE of composite fermions in the composite fermion picture. The Landau level filling is expressed as $\nu = N_e/N_\phi$, for N_e electrons in N_ϕ flux quanta, so that an odd fraction, say, $\nu = 1/3$ implies that there are three flux quanta per each electron on average. In the composite fermion picture we attach two flux quanta to each electron (in a kind of gauge transformation), and we are left with one flux quantum. So the $\nu = 1/3$ state can be mapped to a $\nu = 1$ state of composite fermions in a mean-field sense. One application of this correspondence is the “global phase diagram” in Fig.24.[62] We have explained the $\sigma_{xx} - \sigma_{xy}$ diagram above for the IQHE. If we combine this with the composite particle transformation, we can, again in a mean-field sense, a phase diagram for the integer and fractional QHE phases against the Landau level filling and the degree of disorder.

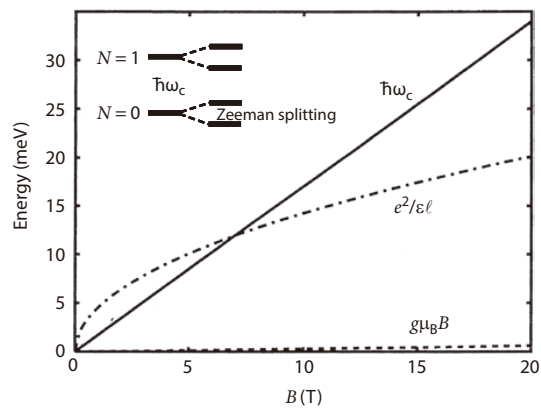


Figure 40: Various energy scales (cyclotron, Coulomb and Zeeman) against magnetic field, here plotted for GaAs. Inset schematically shows the Landau levels with Zeeman splitting.

12 QHE in graphene

One fascinating aspect of the condensed-matter physics is that we can have various field theories effectively realised on low-energy scales. Recent emergence of the physics of massless Dirac particles (or Weyl particles in the language of field theoretic textbooks) in graphene is a prime example. While the three-dimensional graphite has long been studied extensively, experimental fabrication of graphene had to wait for the accomplishment by Geim's group around 2004. IQHE then received a strong impetus when seminal series of works on graphene were launched for graphene after around 2005.[63, 64, 65]

12.1 Monolayer graphene

Graphene is a monolayer graphite with a honeycomb array of carbon atoms (Fig.41(a)), while graphite is a stack of graphene sheets (in a staggered manner called Bernal stacking). Electrons on a single layer of honeycomb lattice, despite its simplicity, provide rich problems in condensed matter physics. Specifically, it has long been known that its band dispersion (for carbon's π orbitals) is composed of a pair of k -linear conical electron and hole dispersions that touch with each other at $E = 0$ (Fig.41(b)), so that the graphene is a condensed-matter realisation of massless Dirac fermions in two spatial dimensions around $E = 0$ (at which E_F usually resides). This was noted by Wallace as early as in 1947. Subsequently the reason why honeycomb symmetry implies the massless Dirac dispersion was revealed group-theoretically by Lomer and by Coulson in the 1950's. Band analysis in terms of the $k \cdot p$ perturbation was also done by Slonczewski and Weiss. Three-dimensional graphite, by contrast, has a band structure of a semimetal with a Fermi surface comprising small electron and hole pockets.

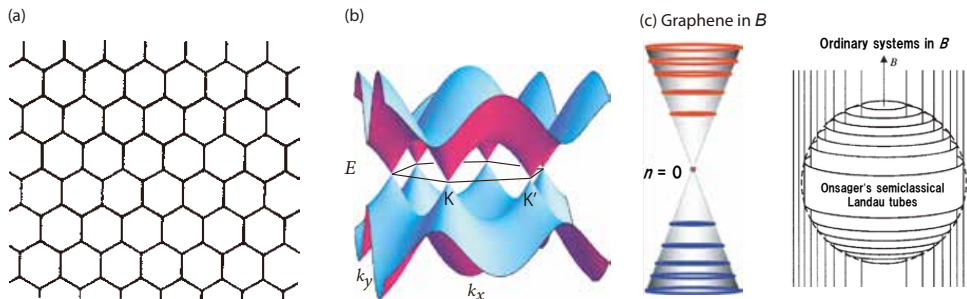


Figure 41: Crystal structure (a) and the band dispersion (b) of graphene. (c) Landau levels around each Dirac cone in a magnetic field B , with $n = 0$ Landau level highlighted. An attached panel on the right schematically shows Onsager's semiclassical Landau quantisation in terms of Landau tubes on the Fermi surface for ordinary systems.

An inherent aspect of graphene is that it has two, inequivalent Dirac cones at K and K' points in the first Brillouin zone (Fig.41(b)). The region around each of K and K' is called a "valley". To see this we should go back to the honeycomb lattice, which is a non-Bravais lattice that contains two (A and B) sublattice sites in a unit cell. Such a lattice is called bipartite, where the energy spectrum is shown to be electron-hole symmetric about $E = 0$ if we only consider nearest-neighbour hopping. The tight-binding model (for π electrons that is relevant

to conduction) on a honeycomb lattice reads, in k -space,

$$\begin{aligned}\mathcal{H} &= t \sum_{\mathbf{k}} \begin{pmatrix} 0 & D(\mathbf{k}) \\ D^*(\mathbf{k}) & 0 \end{pmatrix}, \\ D(\mathbf{k}) &= 1 + e^{-ik_1} + e^{-ik_2},\end{aligned}\tag{42}$$

where the 2×2 matrix is spanned by the AB sublattices, k_1, k_2 are the wavevectors along the primitive vectors in the reciprocal space for the honeycomb lattice. The eigenenergies are $\pm |D(\mathbf{k})|$, giving us the Dirac-cone dispersion.

In the vicinity of K and K' in the Brillouin zone, we can use the $k \cdot p$ perturbation to show that the Hamiltonian is linearised in p as

$$\mathcal{H} = v_F (\sigma_x \tau_z p_x + \sigma_y p_y),\tag{43}$$

where $v_F \simeq 10^8$ cm/s is the Fermi velocity, and σ_μ is the Pauli matrix for the 2×2 Hamiltonian, while τ_z is another Pauli matrix representing the valley (K and K') degrees of freedom with $\tau_z = 1(-1)$ for K (K'). So the equation (for each value of τ_z) has the same form as the Dirac equation for a massless particle in two spatial dimensions, although the equation here does not refer to a relativistic one. The Hamiltonian anticommutes with σ_z (which plays the role of a Dirac operator γ_5 in (3+1) dimensional Dirac field), and this symmetry is called the chiral symmetry, again borrowing from the Dirac-electron nomenclature.

In a more general framework, we can generically express the Hamiltonian for two-band systems as

$$\mathcal{H}(\mathbf{k}) = \mathbf{R}(\mathbf{k}) \cdot \boldsymbol{\sigma} = \begin{pmatrix} R_3 & R_1 - iR_2 \\ R_1 + iR_2 & -R_3 \end{pmatrix},$$

where $\mathbf{R} = {}^t(R_1, R_2, R_3)$ is a three-dimensional real vector with $R_1(\mathbf{k}) = \text{Re} D(\mathbf{k})$ and $R_2(\mathbf{k}) = -\text{Im} D(\mathbf{k})$, while $\boldsymbol{\sigma} = (\sigma_1, \sigma_2, \sigma_3)$ is again the Pauli matrix. In this representation, the eigenenergies are given as $E(\mathbf{k}) = \pm |\mathbf{R}(\mathbf{k})|$. From the $k \cdot p$ perturbation, we have

$$\mathcal{H}(\mathbf{k}) \approx [(\partial_{k_x} \mathbf{R}) \cdot \boldsymbol{\sigma}] k_x + [(\partial_{k_y} \mathbf{R}) \cdot \boldsymbol{\sigma}] k_y\tag{44}$$

around each valley.

This formalism answers the question: Is the Dirac cone an accident for the honeycomb lattice? and when and how Dirac cones actually appear? The answer is that we have Dirac cones when the chiral symmetry exists. When there exists a (Hermitian) operator $\boldsymbol{\gamma}$ (with $\boldsymbol{\gamma}^2 = 1$) that anticommutes with the Hamiltonian as $\{\mathcal{H}, \boldsymbol{\gamma}\} = 0$, the Hamiltonian is called ‘‘chiral-symmetric’’. Equation (42) has the chiral symmetry with $\boldsymbol{\gamma} = \sigma_z$. In more general terms with Eq(44), the Hamiltonian is chiral-symmetric if $\mathbf{R}(\mathbf{k}) \perp \mathbf{n}_\gamma$ everywhere in k -space with a certain vector \mathbf{n}_γ , for which the chiral operator is given as $\boldsymbol{\gamma} = \mathbf{n}_\gamma \cdot \boldsymbol{\sigma}$. Then we can designate the value of the chirality χ as $\chi = +1$ when the three vectors $(\partial_{k_x} \mathbf{R}, \partial_{k_y} \mathbf{R}, \mathbf{n}_\gamma)$ are right-handed, or $\chi = -1$ when left-handed. See Ref[66] for details.

In the presence of a magnetic field, we can replace \mathbf{p} with $\boldsymbol{\pi} = \mathbf{p} + (e/c)\mathbf{A}$ in the $k \cdot p$ Hamiltonian. Then the Landau levels become, as shown by McClure in 1956, $E_N = \sqrt{N} \hbar \omega_c$ with $\omega_c = (\sqrt{2}/\ell) v_F = (2ev_F/c\hbar) \sqrt{B}$, ℓ the magnetic length as usually defined (Eqn(11)), and

$N = 1, 2, \dots$ ($N = -1, -2, \dots$) correspond to electron (hole) Landau levels. The Landau levels are $\propto \sqrt{N}$ and not uniformly spaced in sharp contrast to the usual, uniformly-spaced Landau levels. In particular, there is the $N = 0$ Landau level right at the Dirac point $E = 0$. The cyclotron energy $\propto \sqrt{B}$ is also unusual. The $N = 0$ Landau level is quite peculiar, which is brought home by noting that the level is completely outside the Onsager's semiclassical quantisation scheme in magnetic fields (because the Landau tube, which is the set of cylinders of varying radii for the semiclassical quantisation, cannot be defined around the Dirac point). In fact the $N = 0$ Landau level is an outcome of a topological property of the massless Dirac cone, so that its presence is 'topologically protected'. If we go back to the original honeycomb lattice in magnetic fields, the problem becomes a Hofstadter butterfly for the honeycomb lattice (Fig.42(b)), which was first obtained by Rammal in 1985.

Incidentally, it is heuristic to look at the Landau's quantisation in the (massive) relativistic particles. From the Dirac equation for a Dirac particle in a magnetic field, the energy levels are $E_N = [m^2c^4 + mc^2(\hbar\omega_c(2N + 1 \pm 1))]^{1/2}$, [67] which contains the non-relativistic limit, $E_N = mc^2 + \hbar\omega_c(N + 1 \pm 1/2)$, as the leading term in $\hbar\omega_c/mc^2$ expansion. The massless limit, $m \rightarrow 0$, can be taken by taking care of $\omega_c = eH/mc$ that also contains the mass if we want to recover the graphene Landau levels.

Soon after the fabrication of graphene samples, an anomalous IQHE was observed by Geim's group, and by Kim's group. [63, 64, 65] The IQHE in graphene has

$$\sigma_{xy} = -2\frac{e^2}{h}(2N + 1) \quad (45)$$

as contrasted with the usual $\sigma_{xy} = -2\frac{e^2}{h}N$ when the carriers are filled up to the N -th Landau level. The prefactor of 2 in these equations is for the spin degeneracy. The peculiarity of the Dirac cone appears as the factor $(2N + 1)$ replacing the ordinary N as shown by [68, 69]. There are K and K' valleys that contribute equally to the Hall conduction, so that if we factor out the valley degeneracy of 2 along with the spin degeneracy, we can write

$$\sigma_{xy} = -4\frac{e^2}{h}(N + 1/2),$$

where, remarkably, a fraction $(1/2)$ appears in the valley-resolved contribution.

The situation around the $N = 0$ Landau level is indeed unusual. Let us compare the situation with the ordinary one where we have a (massive) conduction band and a (massive) valence band in Fig.43. In the latter case, we have an ordinary IQHE sequence, $0 \rightarrow 1 \rightarrow 2 \rightarrow \dots$, for electrons (in the conduction band) and another, $0 \rightarrow -1 \rightarrow -2 \rightarrow \dots$, for holes (in the valence band). For a Dirac cone, the IQHE step across $N = 0$ at the Dirac point (i.e., an electron-hole symmetric point) cannot be $0 \rightarrow +1$ nor $-1 \rightarrow 0$, which would be incompatible with the electron-hole symmetry. Instead, the step changes from $-1/2$ to $+1/2$ at $N = 0$. The quantum Hall step are observed to remain robust even at room temperature, which is distinct from the usual QHE.

Topologically, the appearance of $1/2$ in the graphene QHE is actually natural, since, in the representation Eq.(44), we can express the TKNN formula adapted for the two-band model that has a chiral symmetry as

$$C = -\frac{1}{8\pi} \int \hat{\mathbf{R}} \cdot (d\hat{\mathbf{R}} \times d\hat{\mathbf{R}}) = -\frac{1}{2} \text{sgn}(m\chi), \quad (46)$$

where $\hat{\mathbf{R}} \equiv \mathbf{R}/R$, m is the mass of the Dirac electron, and χ is the chirality. The Hall conductivity is then given by $\sigma_{xy} = (e^2/h)C$. This is the most concise expression for the graphene quantum Hall number. The massless limit $m \rightarrow 0$ to resume the Dirac cone has to be taken carefully as shown in Fig.44. See Ref.[70, 66] for details.

So far we have mainly dealt with the Dirac field formalism, where the honeycomb lattice structure is only considered in a $k \cdot p$ formalism in the very vicinity of the Dirac points. Then an interesting question is: what if we fully take account of the lattice structure? Will the Dirac-field result, particularly the QHE, be washed away soon after we go away from the Dirac point? Hatsugai et al [70] have looked into this problem, and found that the massless Dirac particle behaviour with the QHE $\sigma_{xy} \propto \pm(n + 1/2)$ persists, surprisingly, up to a significantly high energies, at which the usual finite-mass fermion behaviour abruptly takes over. The boundary energies are just the van Hove singularities, seen in the full band dispersion as the positions at which the Dirac cones are rounded off. A technique developed in the lattice gauge theory enabled them to calculate the behaviour of the topological number. This result indicates a robustness of the topological quantum number, and should be observable if the chemical potential can be varied over a wide range in graphene. The result is summarised in Fig.42.

As for the effect of disorder and its effect on localisation, graphene samples themselves are atomically clean (although there are extrinsic source of disorder such as charged impurities), so that graphene can have a very high mobility. One intrinsic disorder is corrugations of the graphene sheet, called ripples. As for the Landau quantisation in magnetic fields, ripples as represented as random hopping energies or random components in the magnetic field, both of which respect the chiral symmetry, shown to exert anomalously small effect on the broadening of the $N = 0$ Landau level.[71] The spatial correlation length of the disorder, on the other hand, dominates the scattering between K and K' points, where the longer-ranged the disorder the K-K' scattering becomes less effective.

There are other materials that accommodate Dirac cones. A typical example is an organic metal α -(BEDT-TTF)₂I₃ [BEDT-TTF stands for bis(ethylenedithio) tetrathiafulvalene], which comprises a stack of 2D layers and the Dirac cones are tilted and do not sit at the corner of the Brillouin zone. Subsequently, Landau quantisation characteristic of 2D and QHE are reported for this material.[72] Theoretically, the notion of the chiral symmetry, and the associated QHE are constructed for the tilted Dirac cones.[71] In this case, we can generalise the chiral symmetry by introducing a generalised chiral operator γ (which is non-Hermitian in general) with a chiral commutation relation $\gamma^\dagger H + H\gamma = 0$ with the Hamiltonian H . The generalised chiral operator is definable as far as the Hamiltonian is elliptic as a differential operator. We can thus realise that this is a topological effect, related with Atiyah-Singer's index theorem for elliptic differential operators. In magnetic fields, we have QHE, where the peculiarity of the tilted Dirac cone appears as a chirality-protected "zero-mode", i.e., $n = 0$ Landau level at $E = 0$ which remains sharp even with disorder, again as far as the disorder is not too rapidly-varying in real space. The zero-mode Landau level has experimentally been detected in the α -(BEDT-TTF) system.[72]

12.2 Optical properties in graphene

Graphene QHE offers ample opportunities in photonics as well. Let us touch upon them. An example is a proposal of Landau-level laser. For the ordinary 2DEG in magnetic fields,

Aoki proposed that, if we can pump the electrons in lower Landau levels to higher ones, then a cyclotron emission may realise a laser, where the emitted frequency (Landau level spacing $\hbar\omega_C \propto B$) can be tuned with the magnetic field.[73] However, a difficulty is that the Landau levels in 2DEGs are equally spaced, so that a photon energy tuned to the spacing would incur a ladder of excitations rather than a simple population inversion. Then, Morimoto et al[74] suggested that, if we go over to graphene, the Landau levels are not equally spaced, so that this problem is evaded as in Fig.45. Still, dynamics of electrons, which involve phonons and photons for relaxation processes such as Auger processes, have to be examined. For recent references, see [75]. A zinc-blende crystal HgCdTe, which has a cone and an almost flat band in the band structure [76] may also be interesting.

One conceptually interesting question is: can we observe the QHE without attaching electrodes to the sample? If we can accomplish this, this will provide a new avenue for manipulating optical properties through QHE physics. Morimoto et al[77] have proposed that when a (linearly-polarised) light is illuminated to a QHE system, the optical Hall conductivity $\sigma_{xy}(\omega)$ against photon frequency ω should exhibit a characteristic feature typically in THz regime, as shown in Fig.46. Namely, the optical Hall conductivity, measured through the Faraday rotation, should have plateaux, both in the ordinary 2DEG and in graphene in the quantum Hall regime, although the plateau height is no longer rigorously quantised in ac. In graphene, the optical conductivity $\sigma_{xy}(\omega)$ reflects the unusual Landau level structure. The optical QHE remains robust against the significant strength of disorder according to a theoretical result, which is attributed to an effect of the mobility gap due to localisation. The estimated Hall angle in ac regime is of the order of the fine-structure constant α (i.e. ~ 7 mrad). This has subsequently been experimentally detected by Shimano's group for a 2DEG[78] and for graphene.[79]

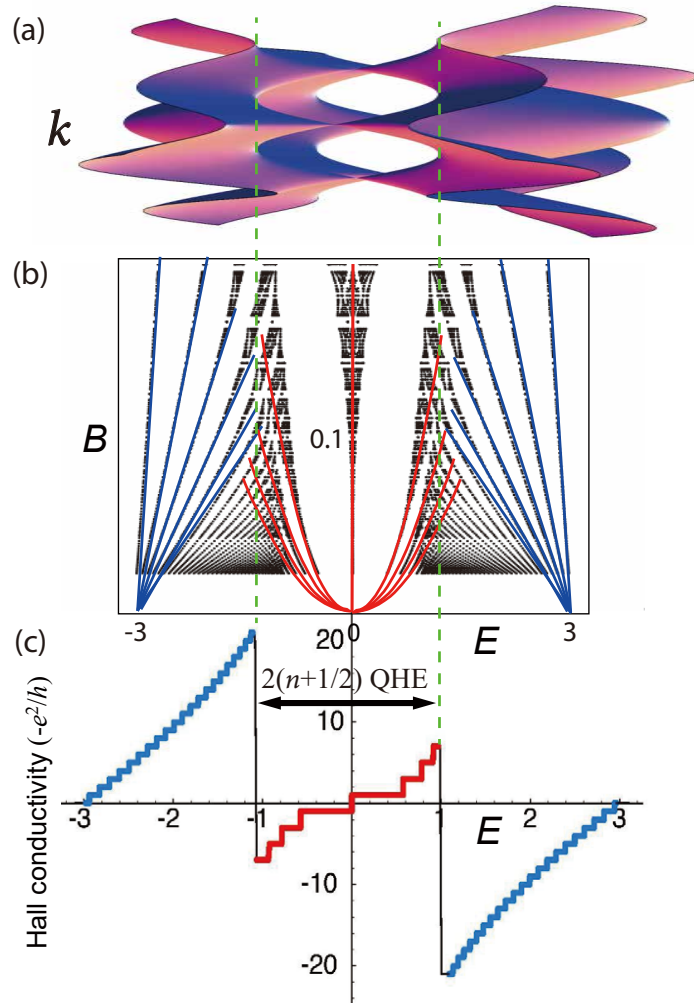


Figure 42: For the honeycomb tight-binding model for graphene, we show (a) the full band dispersion over the entire energy range E , (b) the energy spectrum (black) against E and external magnetic field B , and (c) the quantum Hall conductivity in units of $-e^2/h$. The unit of energy is the absolute value of the nearest-neighbour hopping in the tight-binding model, and vertical green lines mark the position of the van Hove singularities. In (b) Dirac-electron Landau levels are superposed in red, while the usual massive-fermion Landau levels, starting from the band edges, are superposed in blue. The magnetic field B is measured by the magnetic flux $\phi \equiv BS/(2\pi)$ penetrating each unit hexagon of area S in the honeycomb lattice. In (c) the Chern number is plotted for a magnetic field $\phi = 1/31$ here. The red lines indicate the graphene QHE with $\sigma_{xy} = \pm 2[n + (1/2)]e^2/h$, n : integer and factor of 2 coming from the valley degeneracy), while the blue lines the usual QHE with step of one ($\sigma_{xy} = \pm ne^2/h$).

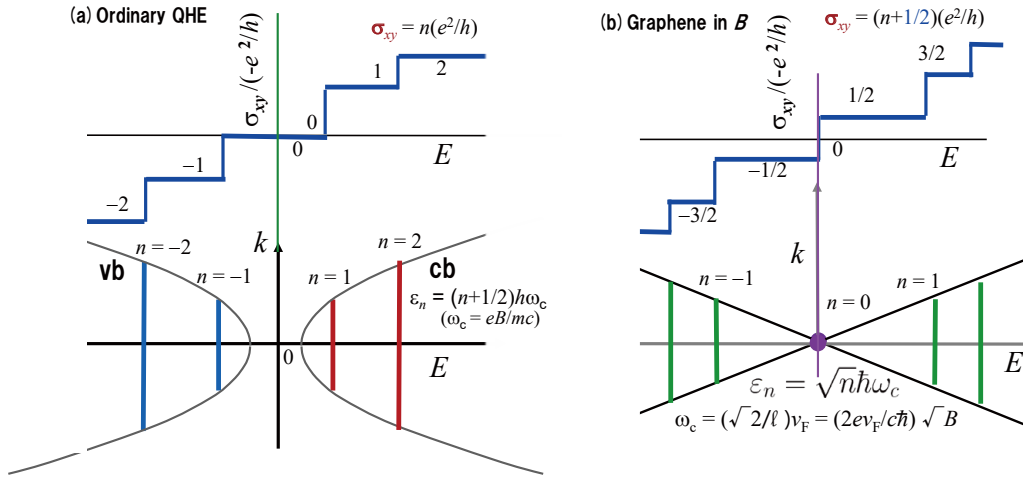


Figure 43: Band dispersion and Landau levels (lower panels) and the QHE steps (upper) are compared between the ordinary 2D system with valence and conduction bands (a) and graphene with k -linear, Dirac-cone dispersion (b).

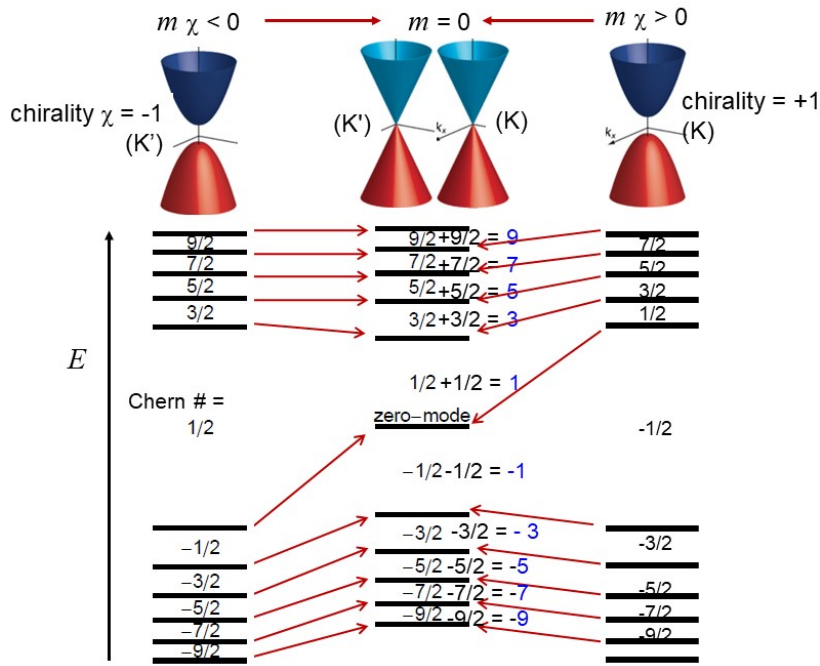


Figure 44: The way in which the Landau levels of a massive Dirac fermion with chirality $\chi = -1$ (valley K'; left column) or $+1$ (K; right) cross over (red arrows) to those for the massless Dirac cones. The numbers in black represent the Chern numbers for each valley, while the numbers in blue the sum of K and K' contributions. Top insets depict the dispersions. After Y. Hatsugai and H. Aoki in H. Aoki and M.S. Dresselhaus (eds.): *Physics of Graphene* (Springer, 2014), Ch.7.

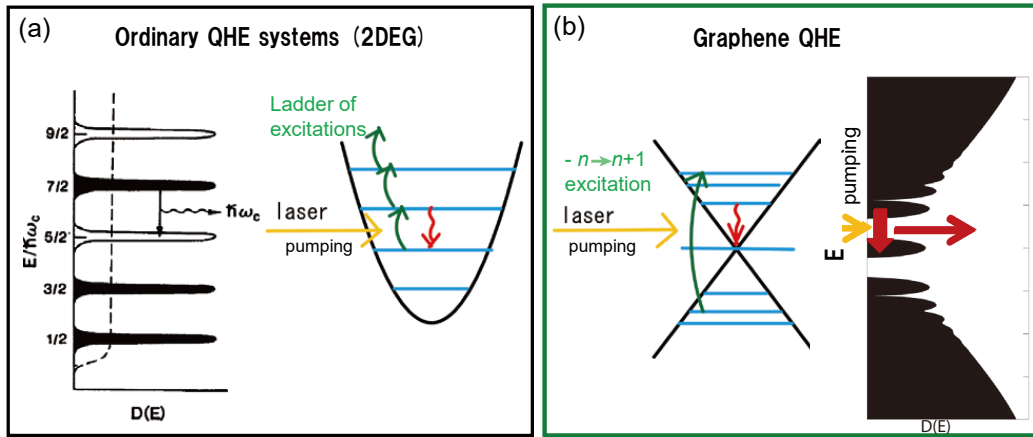


Figure 45: (a) Landau levels and optical pumping are schematically shown. After H. Aoki, Appl. Phys. Lett. **49**, 559 (1986). (b) Graphene Landau levels and optical pumping. After T. Morimoto et al, Phys. Rev. B **78**, 073406 (2008).

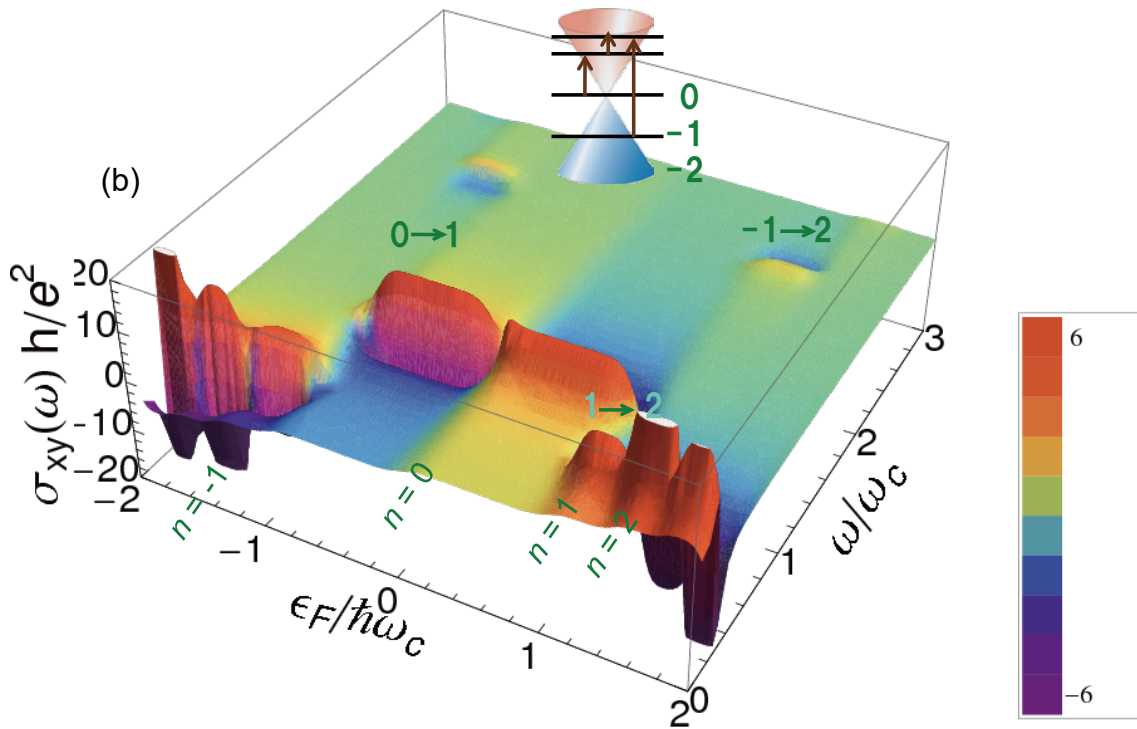


Figure 46: Theoretical result for the optical Hall conductivity $\sigma_{xy}(\epsilon_F, \omega)$ plotted against photon frequency ω and the Fermi energy ϵ_F for the graphene QHE system. Associated Landau level index n is indicated, with the inset depicting the levels and optical transitions on a Dirac cone. After T. Morimoto et al, Phys. Rev. Lett. **103**, 116803 (2009).

12.3 QHE and superconductivity

As reviewed in Section 1, there is a whole spectrum of topological systems, which includes the topological superconductivity (BdG class in the classification table, Fig.1). So it may be heuristic to have a brief look at the analogy between QHE and superconductivity (SC), because the 2×2 Hamiltonian for graphene has a similarity with 2×2 Hamiltonian for superconductors in the Nambu's spinor and Bogoliubov-de Gennes representations. Naively, the correspondence between QHE and SC would be

	IQHE	SC
bulk	gapped (Landau levels)	gapped (SC gap)
edge	chiral edge states	Andreev bound states

However, the analogy is not so simple: Only for the topological SC (time-reversal broken SC such as p+ip, d+id that belong to class D and C with spatial dimension $d = 2$ in the classification table, Fig.1)) does the analogy hold. Those SCs are described by a 2×2 Hamiltonian,

$$\mathcal{H} = t \sum_{\mathbf{k}} \begin{pmatrix} \epsilon_{\mathbf{k}} - \mu & \Delta(\mathbf{k}) \\ \Delta^*(\mathbf{k}) & -\epsilon_{\mathbf{k}} + \mu \end{pmatrix} = \mathbf{R}(\mathbf{k}) \cdot \boldsymbol{\sigma}, \quad (47)$$

in the BdG formalism, where $\mathbf{R} = {}^t(\text{Re } \Delta(\mathbf{k}), -\text{Im } \Delta(\mathbf{k}), \epsilon_{\mathbf{k}} - \mu)$. The off-diagonal element, Δ , represents the gap function, while $\epsilon_{\mathbf{k}}$ is the band dispersion, and μ is the chemical potential. The two-dimensional SC with broken time-reversal symmetry such as p+ip pairing is sometimes called a chiral SC. We have e.g. $\Delta(\mathbf{k}) \sim k_x + ik_y$ for p+ip, which is complex, signifying the broken time-reversal. Then the topological number for the topological SC is given by

$$C = \frac{1}{4\pi} \int \hat{\mathbf{R}} \cdot \left(\frac{\partial \hat{\mathbf{R}}}{\partial k_x} \times \frac{\partial \hat{\mathbf{R}}}{\partial k_y} \right) d\mathbf{k}, \quad (48)$$

where $\hat{\mathbf{R}} \equiv \mathbf{R}/R$. This formula corresponds to the TKNN expression for the QHE Chern number, namely Eq.(33) for 2DEG, or more directly to Eq.(46) for graphene which is a two-band system as in the Nambu representation for SC. As for the edge currents, we can also compare them between the QHE and topological SC states as shown in Fig.47. See also Fig.3.

We can also mention that, if we go over to Floquet physics, which is described in Section "QHE in light-matter coupled systems - Floquet topological insulator" below, we can realise a topological SC (d+id pairing) when we illuminate a d-wave SC with a circularly-polarised light. This is not as straightforward as in the realisation of Floquet topological insulator described in that section, since the light field does not directly couple with the gap function (where a pair is electrically neutral). We can evade this difficulty, however, by going to the strong electron correlation, where the Floquet physics generates photon-induced many-body interactions (multi-site pairing interactions) rather than a modification of one-band structure, as shown by Kitamura et al.[80] This provides a realisation of class C in the classification table.

12.4 QHE in bilayer graphene

There has been an upsurge of developments in bilayer and multilayer graphene systems. In particular, this has opened a seminal avenue towards twisted bilayer graphene, which has turned

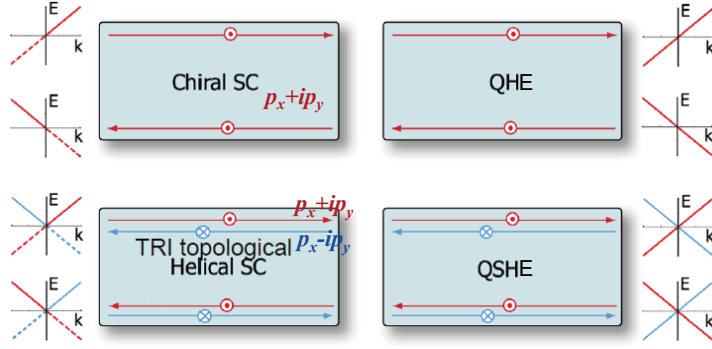


Figure 47: Edge currents (arrows) in various QHE and topological SC states. Top row: A comparison of a 2D chiral superconductor with QHE, where, in both cases, the time-reversal (TR) symmetry is broken and chiral edge states appear. Bottom row: A comparison of a 2D TR-invariant topological superconductor with QSHE insulator, where, in both cases, TR symmetry is preserved and helical pairs of edge states appear for up (red, \odot) and down (blue, \otimes) spins. Band dispersions are attached. After X.L. Qi et al, Phys. Rev. Lett. **102**, 187001 (2009).

out to accommodate interesting physics and phenomena, encompassing QHE and superconductivity. So let us look at them in this section, starting with the (untwisted) bilayer graphene.

12.4.1 Untwisted bilayer graphene

An untwisted bilayer graphene consists of two graphene sheets coupled by interlayer hoppings as shown in Fig.48, where a B sublattice in the top sheet is located just above an A sublattice of the bottom sheet (called AB stacking or Bernal stacking). A unit cell thus contains four carbon atoms (A1, B1 in the top layer; A2, B2 in the bottom). Main hoppings are the intralayer nearest-neighbour hopping (γ_0), and the vertical interlayer hopping (γ_1). An oblique interlayer hopping (γ_3) also exists, which causes a three-fold (trigonal) warping of the Dirac cone around the Brillouin zone corners, K_{\pm} . The magnitudes of these are $\gamma_0 \simeq 3$ eV, $\gamma_1, \gamma_3 \simeq 0.3$ eV.

In a basis with components $(\psi_{A1}, \psi_{B1}, \psi_{A2}, \psi_{B2})$, the Hamiltonian for the bilayer graphene is given as

$$H_{AB} = \begin{pmatrix} 0 & v\pi^\dagger & 0 & v_3\pi \\ v\pi & 0 & \gamma_1 & 0 \\ 0 & \gamma_1 & 0 & v\pi^\dagger \\ v_3\pi^\dagger & 0 & v\pi & 0 \end{pmatrix}, \quad (49)$$

where $\pi = \xi\pi_x + i\pi_y$, $\boldsymbol{\pi} = \mathbf{p} + e\mathbf{A}$, with \mathbf{A} being the vector potential arising from the applied magnetic field, and the valley index $\xi = \pm 1$ for K_{\pm} points. Here $(v, v_3) \equiv (\sqrt{3}a/2\hbar)(\gamma_0, \gamma_3)$ are the hopping elements expressed in terms of velocities with $a \simeq 0.23$ nm being the distance between the nearest A sites.

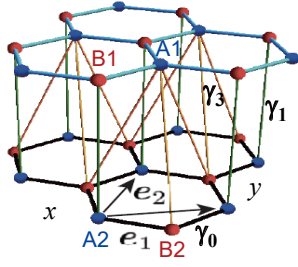


Figure 48: The lattice structure of an (untwisted) bilayer graphene. A lattice site on B sublattice (red) in the top sheet is located just above an A sublattice site (blue) of the bottom sheet, and a unit cell contains four carbon atoms (A1, B1 in the top layer; A2, B2 in the bottom). Main hoppings are the intralayer nearest-neighbour hopping (γ_0), the vertical interlayer hopping (γ_1), and an oblique interlayer hopping (γ_3).

The low-energy physics of bilayer graphene, for an energy region with $\varepsilon \ll \gamma_1$, is captured in the leading order in ε/γ_1 by a 2×2 Hamiltonian in a basis of (A1,B2) carbon sites as

$$H_{\text{AB}}^{(\text{eff})} = \frac{1}{2m} \begin{pmatrix} 0 & (\pi^\dagger)^2 \\ \pi^2 & 0 \end{pmatrix} + v_3 \begin{pmatrix} 0 & \pi \\ \pi^\dagger & 0 \end{pmatrix}, \quad (50)$$

with an effective mass $m = \gamma_1/(2v^2)$. In the absence of magnetic fields, the first term on the right-hand side gives a pair of parabolic bands, $E = \pm p^2/(2m)$, touching with each other. The second term coming from γ_3 causes the trigonal warping, and makes each Dirac cone reshaped into four small cones, where the Lifshitz transition (change of the topology of the Fermi surface from four pockets to a single one as the Fermi energy is varied) occurs at $E_{\text{Lifshitz}} = (1/2)mv_3^2 \sim 1$ meV.

The Landau level spectrum in a uniform magnetic field $\mathbf{B} = \text{rot}\mathbf{A}$ may be obtained with a standard procedure of introducing boson creation and annihilation operators, a^\dagger and a , as $(\pi, \pi^\dagger) = (\sqrt{2}\hbar/\ell)(a^\dagger, a)$ for valley K_+ , or $(\pi, \pi^\dagger) = (\sqrt{2}\hbar/\ell)(a, a^\dagger)$ for K_- . The eigenenergies are then given by[81]

$$\varepsilon_{n,s} = s\hbar\omega_c\sqrt{n(n+1)}, \quad (51)$$

where states are labeled by the Landau index $n = \dots, -1, 0, 1, \dots$, and the band index $s = \pm$ labeling the conduction ($s = +$) and valence ($s = -$) bands, and the cyclotron energy is $\hbar\omega_c = (\hbar eB/m) \simeq 3.5(B/1\text{Tesla})$ meV. Two zero-energy Landau levels appear ($n = 0, -1$) in each valley.

12.4.2 Twisted bilayer graphene

Bilayer graphene physics witnessed an unexpected new impetus in what is called the “magic-angle twisted bilayer graphene”, which has turned out to accommodate rich physics. A technical

breakthrough is that it became possible to put a second graphene layer on top of another with a designated twist angle, namely, the crystallographic axis of the top layer is rotated with some angle, θ from that of the bottom one. The top view of the bilayer honeycomb lattices forms what is generally known as “Moiré pattern”, and is quite sensitive to θ .

For the honeycomb bilayer, this strongly affects the electronic structure including the formation of Dirac cones. For small θ s, the period of the Moiré pattern is large in real space, which implies there are a lot of band foldings with the enlarged unit cell, resulting in a lot of Moiré subbands. Specifically, at the magic angle, $\theta \sim 1^\circ$, the lowest subband exhibits a dispersion that has almost completely flat portions. This hosts various quantum phases, such as QHE as well as superconductivity.[82]

If we denote the reciprocal lattice vectors of the bottom layer as $(\mathbf{b}_1, \mathbf{b}_2)$, the top layer has reciprocal vectors $\hat{R}\mathbf{b}_i$ ($i = 1, 2$) with \hat{R} being the rotation matrix. Then the primitive lattice vectors, \mathbf{A}_i ($i = 1, 2$), of the twisted bilayer graphene (TBG) satisfy $\mathbf{A}_i \cdot \mathbf{B}_j = 2\pi\delta_{ij}$, where $\mathbf{B}_i = (1 - \hat{R})\mathbf{b}_i$ is the reciprocal lattice vectors for the Moiré pattern. We can readily see that

$$|\mathbf{A}_i| = \frac{a}{2 \sin(\theta/2)} \simeq a/\theta, \quad (52)$$

where $a \simeq 0.246$ nm is the graphene lattice constant. Thus the size of the unit cell in the Moiré system for decreasing θ blows up like $1/\theta$, which extends to 14 nm at the magic angle ($\theta \sim 1^\circ$). Not only does the structure have a long period, but the double honeycomb system’s top view comprises a periodic array of AA-, AB-, and BA-stacked patches. The Dirac points of a single-layer graphene reside at the Brillouin zone corners K_+ and K_- separated from the Γ point by $K = 4\pi/(3a)$ as described in sections above, while the TBG has the valleys displaced by

$$\Delta K = 2K \sin(\theta/2) \approx K\theta. \quad (53)$$

Now, K_+ and K_- do not in general fall upon the K_+ and K_- points after the band folding. In other words, the bilayer system is an incommensurate system for general rotation angles. So we have to take care of the band hybridisation caused by the folding for each of K_+ and K_- valleys, while we can ignore the hybridisation across K_+ and K_- when $K \gg \Delta K$.

Figure 49(a) shows an atomic structure of TBG with AA, AB and BA stackings indicated. Panel (b) displays the Brillouin zone folding from the original ones (coloured large hexagons) for layers 1 and 2 into the Moiré Brillouin zone (black small hexagons). Wannier orbitals then reflect the Moiré structure, as typically displayed in panel (c).[83] Panel (d) shows a theoretical band dispersion which exhibits flat parts.[84] The narrow bands, especially flat bands, accommodate a Mott-insulator behaviour[85] arising from strong electron correlation in the flat band.

Since the AA, AB, and BA patches, hence the Wannier functions, form a long-period hexagonal lattice, this realises a Hofstadter problem (described in Section on that) when we apply an external magnetic field to a TBG. Koshino and coworkers have examined this problem to theoretically obtain the Hofstadter butterfly for TBG, Fig.50.[86] They have obtained the Chern numbers, including the case where the bands are partially flat.

This reminds us of the Hofstadter problem for flat-band systems that accommodate flat bands (that are flat over the entire Brillouin zone), as considered in Ref.[87]. An interesting point is the flat band either remain flat or proliferates into a butterfly according as the mechanism which produces the flat band: flat bands that are dictated by space group, as in Lieb’s

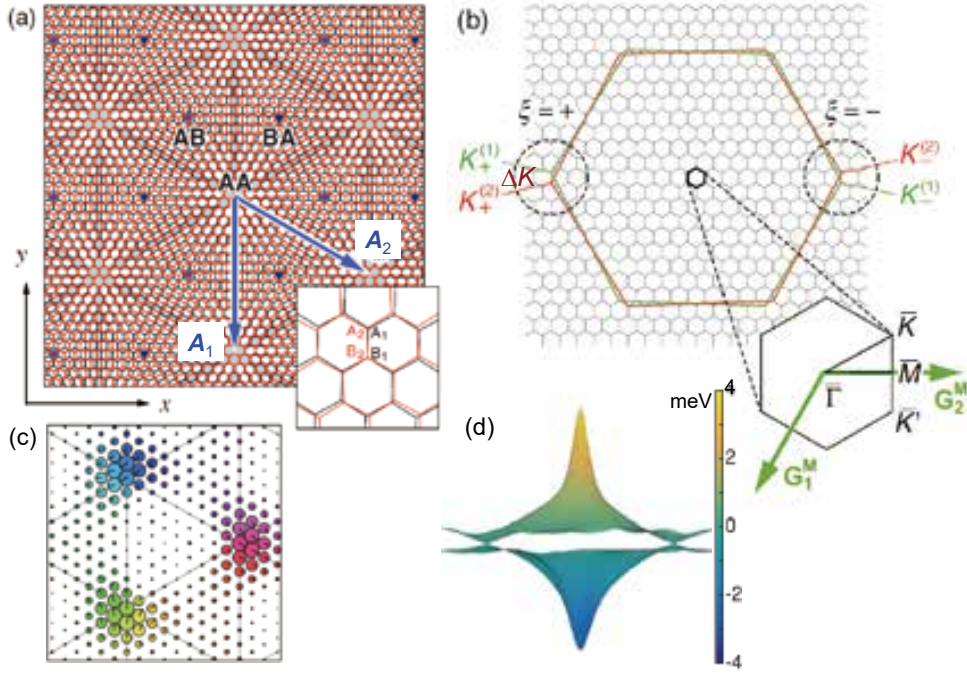


Figure 49: (a) Atomic structure of the twisted bilayer graphene (TBG) with twist angle $\theta (= 3.89$ degrees here). AA, AB and BA stackings are marked, and inset is a blowup. The primitive lattice vectors of the Moiré structure are denoted as \mathbf{A}_i ($i = 1, 2$). (b) Brillouin-zone (Bz) folding with green (red) large hexagon representing the first Bz of layer 1 (2), and black small hexagons the Moiré Bz. (c) An example of maximally localised Wannier wavefunction in a flat band of valley $\xi = +$ of TBG with $\theta = 1.05$ degrees here. The wavefunction amplitude is indicated by the radius of each circle, while its phase by arrows and colours. After M. Koshino et al, Phys. Rev. X **8**, 031087 (2018). (d) An example of theoretical band dispersion in the first Bz with $\theta = 1.05$ degrees here. After H.C. Po et al, Phys Rev. B **99**, 195455 (2019).

model, remain flat in magnetic fields, while the flat bands that arise from quantum interference of wavefunctions, as in Mielke's and Tasaki's models, split into butterflies.

The TBG has turned out to harbour versatile quantum phases that include superconductivity. In a typical example of experimentally obtained phase diagram against carrier density n and temperature T , [88] we can see superconducting states, along with metal, band insulator, and correlated insulating states that occur around integer values of the Moiré band filling.

Since the electronic state in TBG is extremely sensitive to the twist angle θ , it is desirable to explore the inhomogeneity and disorder in the angle in a sample. Uri et al [89] have employed a nanoscale on-tip scanning superconducting quantum interference device (SQUID-on-tip) to obtain tomographic images of the Landau levels in the quantum Hall state along with the local variations in θ . Landau levels, superconducting state and correlated states are shown to be significantly affected by local variations in θ and its gradients. One finding is that the gradients of θ generate large in-plane electric fields, which alter the quantum Hall state by forming edge channels in the bulk. The authors suggest that this may be important in device applications.

The bilayer graphene [90] is also extended to multilayer (e.g. trilayer) graphene systems.

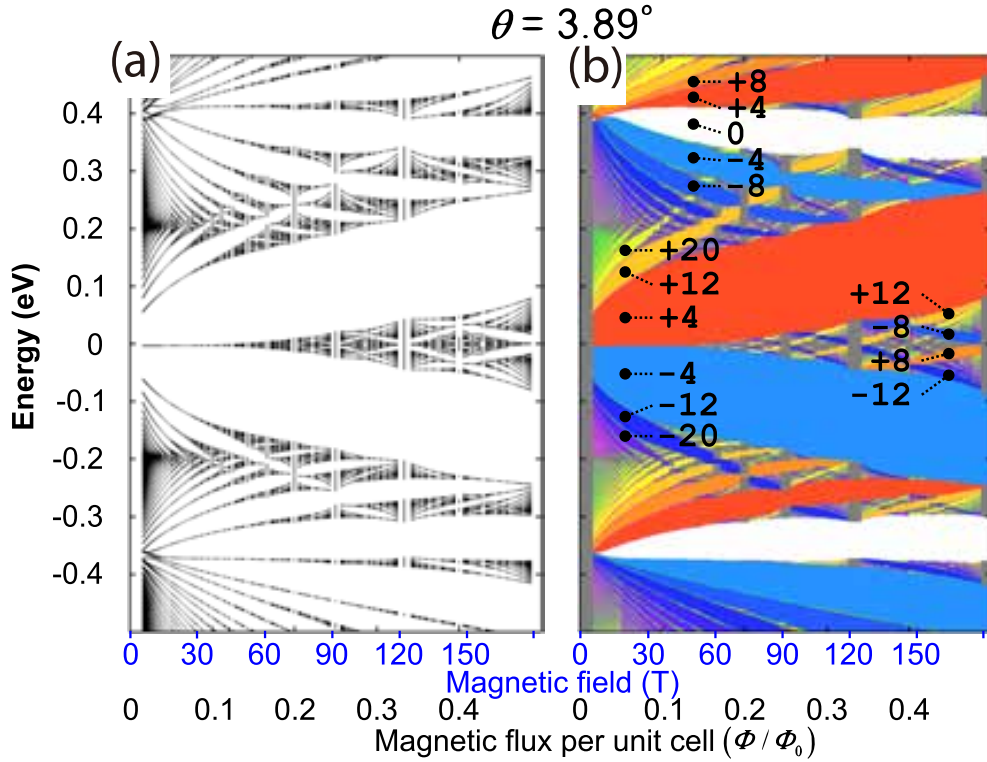


Figure 50: Energy spectrum (a) and the quantum Hall effect (b) against magnetic field in the twisted bilayer graphene with a twist angle of 3.89 degrees here. In (b), the quantised values of the Hall conductivity in individual energy gaps are indicated by numbers and colours. After P. Moon and M. Koshino, Phys. Rev. B **85**, 195458 (2012).

Another avenue of interest in materials is 3D porous graphene. Namely, a class of graphene structures shaped into three-dimensional periodic curved surfaces (“graphitic zeolites”) has been considered. For experiments, refer to Ref.[91]; For theories, refer to Ref.[92]

12.5 Edge states in graphene QHE

We have described above how the graphene QHE is viewed topologically. The topological analysis also leads to another topological character, namely edge states (Fig.51) that appear for a finite graphene having edges in strong magnetic fields (which should not be confused with the graphene edge states in zero magnetic field, an interesting issue in its own right). We have also mentioned earlier that the bulk and edge topological numbers are equal in usual QHE, i.e., $\sigma_{xy}^{\text{edge}} = \sigma_{xy}^{\text{bulk}}$, which can be identified by connecting the topological integers for the bulk and for the edge states. The same applies to the graphene IQHE. Energy spectrum against real-space position also differs in graphene from the usual QHE system as depicted in Fig.52.

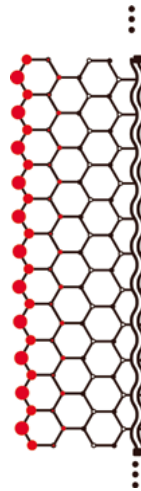


Figure 51: A typical edge states in graphene in a strong magnetic field (here for the flux $\phi = 1/5$) obtained numerically, with the charge density represented by the radius of each circle [after H. Aoki et al, *Int. J. Modern Phys. B* **21**, 1133 (2007)].

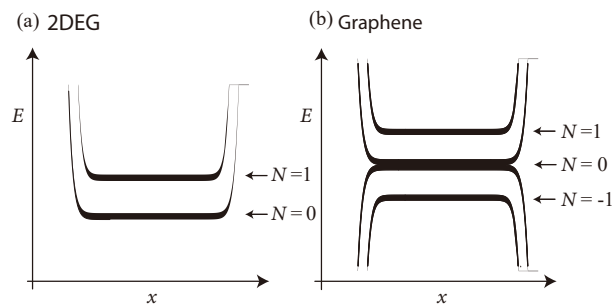


Figure 52: Energy spectrum against the real-space position x along the width for a finite sample is schematically compared between the ordinary QHE system (a) and graphene QHE system (b).

Edge states in graphene in magnetic fields are beginning to be observed with STM as in Ref.[93], which evokes a nanoscale magnetometer (superconducting quantum interference

device; SQUID-on-tip) for the imaging the edge currents, where the topological component of the current is resolved.

12.6 Electric polarisation and topological numbers

Let us mention an aspect of topological properties in QHE systems that is general enough but can be clearly conceived in terms of graphene QHE. As we have seen, topological states, of which the QHE is a canonical example, carry topological numbers, in place of the order parameters in systems having spontaneously broken symmetries. Chern numbers characterising QHE systems become versatile if we consider lattice structures (or periodic potentials) as we have described in Section “Hofstadter spectrum”. [47]

The topological numbers in this problem are determined by a Diophantine equation for integers, [19]

$$r = t_r p + s_r q \equiv t_r p \pmod{q}, \quad (54)$$

where r labels the energy gaps from below, t_r is the QHE topological (Chern) number. Curiously, in addition to the usual QHE topological number, we can note that there exists a second topological number, s_r , appearing in the Diophantine equation. This has long been known, but its physical meaning was revealed only recently by Středa and coworkers, where the second topological number is shown to represent an electric polarisation [94].

Lattice structure, which exerts drastic effects on topological numbers, as in honeycomb lattice in graphene, also affects the second topological number. In the case of graphene, we can show that the polarisation quantum number behaves in a characteristic way in graphene. [95] To derive this we can exploit an adiabatic continuity between the topological numbers for square and honeycomb lattices as Hatsugai and coworkers have earlier shown [70], with which we can establish a correspondence between the topological numbers for the two lattices. With this, graphene is shown to be a “half-flux simulator” (an adiabatic realisation of square lattice with half flux quantum per unit cell). If we now apply this to the polarisation topological number in graphene in magnetic fields, we can show that $s_r = 1$ for a wide energy region (that encompasses the two van Hove singularities), while $s_r = 0$ or 2 outside the vH energies, as shown in Fig.53. The second quantum number can be observable if the density of electrons or the polarisation itself can be measured.

In another context other than QHE, the electric polarisation for crystals can be, and actually should be, formulated in quantum mechanics in terms of Berry’s curvature as pointed out by King-Smith and Vanderbilt. [96] We first note that, in defining the polarisation, the shift of the centre of gravity of the total charge can be ill-defined for an infinite crystal. Instead, the polarisation (or its change, $\Delta \mathbf{P}$, when a parameter that characterises the system is adiabatically varied) is expressed as an integral of a Berry’s curvature as

$$\Delta P_\alpha = -\frac{ie}{(2\pi)^3} \sum_n \int_{\text{BZ}} d\mathbf{k} \int_0^1 d\lambda \left(\left\langle \frac{\partial u_{\mathbf{k}n}}{\partial k_\alpha} \middle| \frac{\partial u_{\mathbf{k}n}}{\partial \lambda} \right\rangle - \left\langle \frac{\partial u_{\mathbf{k}n}}{\partial \lambda} \middle| \frac{\partial u_{\mathbf{k}n}}{\partial k_\alpha} \right\rangle \right), \quad (55)$$

where $u_{\mathbf{k}n}$ is a Bloch wavefunction with n the band index, and the bookkeeping λ describes the adiabatic change ($\lambda = 0 \rightarrow 1$). For a 1D system, we can cast this, with Stokes’s theorem, into

$$\Delta P = -\frac{e}{2\pi} \sum_n \left(i \oint_C \langle u_{\mathbf{k}n} | \frac{\partial}{\partial \mathbf{w}} | u_{\mathbf{k}n} \rangle \right) \cdot d\mathbf{w}, \quad (56)$$

where we have denoted $\mathbf{w} \equiv (\lambda, k_\alpha)$ with k_α being the wavenumber along the real-space axis for the polarisation measurement. The curvature (the quantity in the brackets above) is defined in a two-dimensional parameter space of (λ, k_α) . The line integral along a path C is for $\mathbf{w} = (0, \pi) \rightarrow (1, -\pi) \rightarrow (0, -\pi) \rightarrow (0, \pi)$. Thus the polarisation Chern number s_r in the TKNN formula and the King-Smith and Vanderbilt formula for polarisation share the property that both involve Berry's connection expressed as wavenumber-derivatives of Bloch wavefunctions, although the former has to do with 2D systems while the latter has to do with a physical quantity along a specific spatial direction.

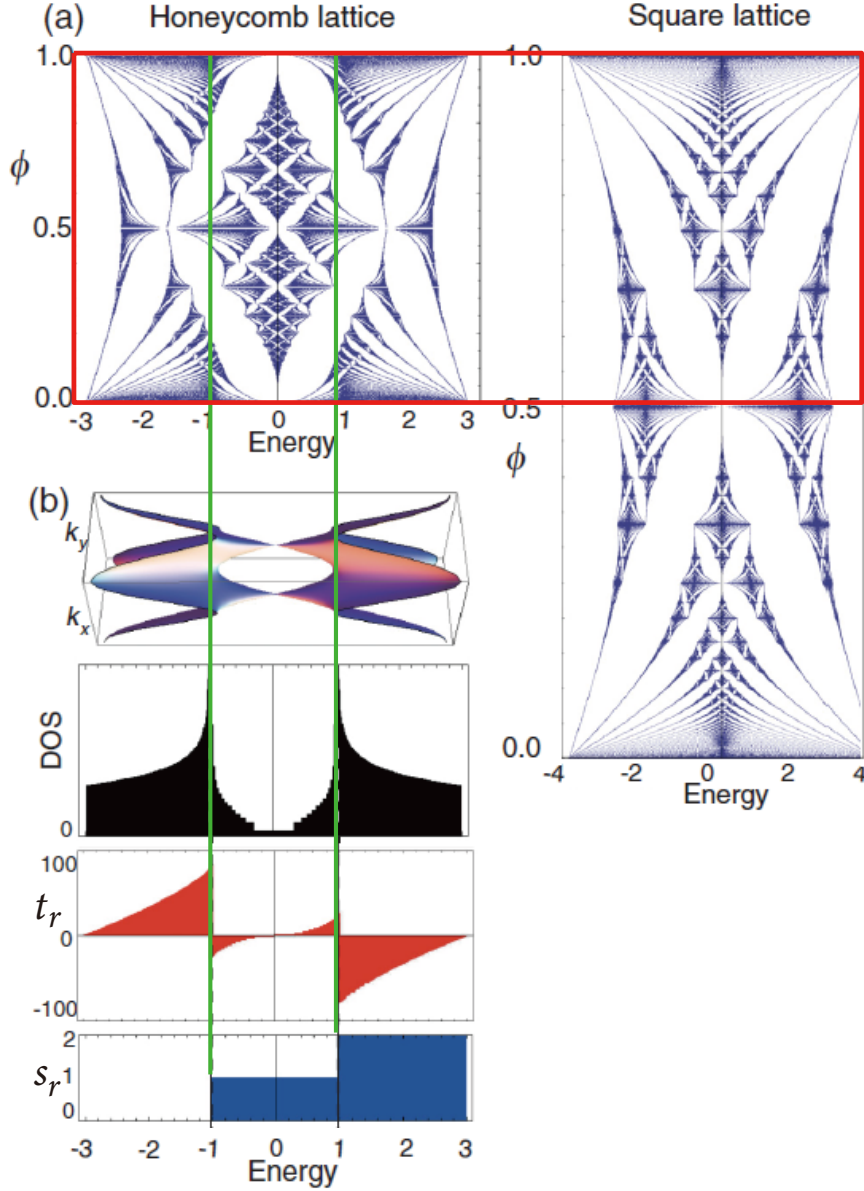


Figure 53: (a) Hofstadter butterfly (one-particle energy spectrum vs magnetic field) for the tight-binding model on honeycomb (left panel) or square (right) lattices. The magnetic field is represented by the magnetic flux ϕ per unit cell in units of the flux quantum $\Phi_0 \equiv h/e$. To indicate the correspondence, $1/q \leftrightarrow 1/2 + 1/(2q)$, between the two lattices, the energy scale is expanded and shifted on the right as marked with a red rectangle. (b) For the honeycomb lattice, the band dispersion (with the energy as a horizontal axis), density of states $D(E)$, the TKNN Chern number t , and the polarisation topological number s are plotted against energy, here for a weak $\phi = \delta (= 1/107)$. Vertical lines mark the van-Hove singularities. After H. Aoki and Y. Hatsugai, Phys. Rev. B **90**, 045206 (2014).

13 QHE in light-matter coupled systems — Floquet topological insulator

13.1 Floquet formalism in general

Nonequilibrium physics has recently flourished into a rich and unique field in condensed-matter physics. This not only enabled us to explore the regimes which are not attainable in equilibrium, but has also provided versatile physical concepts. One prime example, in topological physics, is the Floquet topological insulator as initiated by Oka and Aoki.[97] This evokes a time-periodic modulation (typically laser illumination) to put a system into nonequilibrium. When one deals with quantum states in a time-periodic modulation (such as a laser light), the theoretical starting point is the Floquet formalism for time-periodic external fields. This is based on Floquet's theorem,[99] which is actually much older than Bloch's theorem for spatially periodic potentials — the former dates back to 1883, while the latter conceived in 1928 is much more recent.

The Floquet theory is a theoretical approach to treat periodically driven systems, which can encompass strong external fields such as intense laser. It originates from Floquet's theorem, also known as Hill's theorem in the context of differential equations [100]. As mentioned, the well-known Bloch's theorem for a spatially periodic system is a spatial analogue of Floquet's theorem, and there is a nice parallelism between the two. Due to the periodicity of external fields, the time-dependent problem can be mapped onto a *time-independent* eigenvalue problem. Floquet topological insulator[97] is indeed a remarkable ground for utilising the Floquet formalism, where a control of the topology of quantum systems by external time-periodic modifications, i.e., an application of a circularly-polarised light to graphene (and other multi-band systems), to make the system into a topological quantum Hall insulator, thus providing a prime example of engineering of topological properties.

Floquet's theorem is a general statement about the solution of an ordinary differential equation with a time-periodic potential. In terms of the time-dependent Schrödinger equation,

$$i\frac{d}{dt}\Psi(t) = H(t)\Psi(t), \quad (57)$$

where $\Psi(t)$ is the wave function, and the Hamiltonian $H(t)$ is assumed to be periodic in time t with period \mathcal{T} , $H(t + \mathcal{T}) = H(t)$, the Floquet theorem dictates that the solutions should have a form

$$\Psi_\alpha(t) = e^{-i\varepsilon_\alpha t}\Phi_\alpha(t). \quad (58)$$

Here α labels the eigenfunction, $\Phi_\alpha(t) = \Phi_\alpha(t + \mathcal{T})$ is a periodic function of t , and the real quantity ε_α is called the quasienergy, which is unique up to multiples of the frequency $\Omega \equiv 2\pi/\mathcal{T}$. So we can immediately see that Ψ and ε are temporal counterparts of Bloch's wavefunction and the crystal momentum which is unique up to multiples of $2\pi/a$, the size of the reciprocal vector.

Since the modification is time-periodic, we can readily Fourier-expand the Schrödinger equation on the time axis as

$$\sum_n (H_{mn} - n\Omega\delta_{mn})\Phi_\alpha^n = \varepsilon_\alpha\Phi_\alpha^m. \quad (59)$$

Here, we have Fourier-expanded the wavefunction as $\Phi_\alpha(t) = \sum_n e^{-in\Omega t} \Phi_\alpha^n$ with Φ_α^n called the n th Floquet mode, and

$$H_{mn} \equiv \frac{1}{T} \int_0^T dt e^{i(m-n)\Omega t} H(t) \quad (60)$$

is the Floquet matrix form of the Hamiltonian. Thus the quasienergy ε_α corresponds to the eigenvalues of the infinite dimensional Floquet matrix $H_{mn} - n\Omega\delta_{mn}$. If ε_α is an eigenvalue, the same holds for $\varepsilon_\alpha + n\Omega$ for an arbitrary integer n , and we can impose a condition, $-\frac{\Omega}{2} < \varepsilon_\alpha \leq \frac{\Omega}{2}$, and end up with a ladder of energies with a spacing Ω , just as we have a ladder of Bloch bands within the first Brillouin zone.

As a consequence of the Floquet theorem, the time-dependent Schrödinger equation is mapped onto a time-independent problem, but a price to pay is we have now to solve an infinite-dimensional matrix eigenvalue problem with a new degree of freedom, the Floquet index n . Technically, we have to deal with the problem, which is non-equilibrium and ac-modulated, by combining Keldysh Green's function formalism for non-equilibrium and the Floquet formalism for the ac modulation, into a method dubbed Floquet Green's function. Since the Floquet formalism has to do with nonequilibrium physics, we have also to note that there are both transient quantum states just after the external field is switched on, followed by subsequent nonequilibrium steady states (sometimes called "NESS"). This occurs e.g. when the system during laser excitation is subject to dissipation due to a heat bath, in which case the balance between pumping and relaxation determines the relaxation dynamics, which can be treated with Floquet Green's function. For many-body systems, incidentally, we can formulate the Floquet-DMFT (DMFT: dynamical mean-field theory) by combining the nonequilibrium DMFT and the Floquet method, which is out of the scope here.[98]

Now, let's describe the Floquet topological insulator, following Refs[97, 101]. With laser illumination, transport properties, such as the Hall conductivity, can still be treated with the Kubo formula if we evoke the Floquet states. You might imagine that quantum topological quantities like Berry's curvature that dominates the QHE, defined originally for systems in equilibrium, would become ill-defined in non-equilibrium. This, however, is not the case — the only thing we have to do, for the Floquet steady states, is just define and calculate the curvature by replacing the usual wavefunction with the Floquet wavefunctions. Thus the conductivity tensor σ_{ab} in magnetic fields in an intense ac field \mathbf{A}_{ac} is expressed as

$$\begin{aligned} \sigma_{ab}(\mathbf{A}_{ac}) = & i \int \frac{d\mathbf{k}}{(2\pi)^2} \sum_{\alpha, \beta \neq \alpha} \frac{[f_\beta(\mathbf{k}) - f_\alpha(\mathbf{k})]}{\varepsilon_\beta(\mathbf{k}) - \varepsilon_\alpha(\mathbf{k})} \\ & \times \frac{\langle\langle \Phi_\alpha(\mathbf{k}) | J_b | \Phi_\beta(\mathbf{k}) \rangle\rangle \langle\langle \Phi_\beta(\mathbf{k}) | J_a | \Phi_\alpha(\mathbf{k}) \rangle\rangle}{\varepsilon_\beta(\mathbf{k}) - \varepsilon_\alpha(\mathbf{k}) + i\eta}, \end{aligned} \quad (61)$$

where $f_\alpha(\mathbf{k})$ is the distribution function in the nonequilibrium for the α -th Floquet state, \mathbf{J} is the current operator, and η a positive infinitesimal. There, the energy is replaced with the Floquet quasi-energy, and the inner product $\langle\langle \cdot \rangle\rangle$ includes the time average.

The Hall conductivity then becomes a TKNN-type formula,

$$\sigma_{xy}(\mathbf{A}_{ac}) = e^2 \int \frac{d\mathbf{k}}{(2\pi)^d} \sum_\alpha f_\alpha(\mathbf{k}) \left[\nabla_{\mathbf{k}} \times \mathcal{A}_\alpha(\mathbf{k}) \right]_z, \quad (62)$$

where the gauge field $\mathcal{A}_\alpha(\mathbf{k}) \equiv -i \langle\langle \Phi_\alpha(\mathbf{k}) | \nabla_{\mathbf{k}} | \Phi_\alpha(\mathbf{k}) \rangle\rangle$ is defined in terms of the Floquet state Φ . Note that the occupation $f_\alpha(\mathbf{k})$, which differs from the equilibrium Fermi-Dirac distribution,

depends on the original band index i and the Floquet index m , and depends on e.g. how the heat bath is attached to the system.

13.2 Floquet formalism for graphene — Floquet topological insulator

The above is a general framework. Now let us apply this to graphene, which leads us to the Floquet topological insulator (FTI),[97] as symbolically depicted in Fig.54.

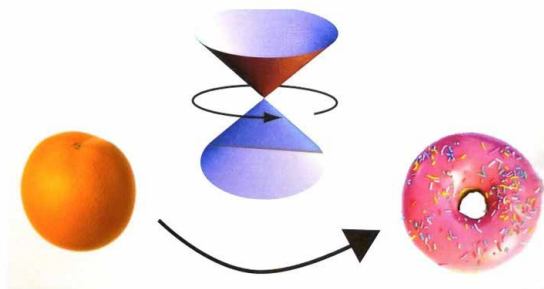


Figure 54: A schematic picture for an illumination of a circularly-polarised light changing the topology of the quantum states in a Dirac system. Top panel represents a Dirac cone in a circular laser, while the bottom one symbolises a change of the topology. Figure courtesy of ETH Quantum Optics group.

For graphene, which has Dirac electrons with electron and hole branches, each matrix element in the Floquet Hamiltonian becomes a 2×2 matrix. Namely, the Hamiltonian is $H(t) = \tau_z v [k_x + A_{ac}^x(t)] \sigma_x + v [k_y + A_{ac}^y(t)] \sigma_y$, where $\tau_z = \pm 1$ labels the valleys (K and K' points in graphene), v is the velocity (set to $v = 1$ here), and σ_i the Pauli matrices. A circularly-polarised laser has the vector potential $(A_{ac}^x, A_{ac}^y) = A(\cos \Omega t, \sin \Omega t)$, where $A \equiv F/\Omega$ with F being the field strength. With Fourier transformed Floquet states $|\Phi(t)\rangle = \sum_m e^{-im\Omega t} |u_\alpha^m\rangle$, the Floquet equation becomes

$$\sum_n H^{mn} |u_\alpha^n\rangle = (\varepsilon_\alpha + m\Omega) |u_\alpha^m\rangle, \quad (63)$$

where, for graphene, we have $H^{mm} = \begin{pmatrix} 0 & k_x - ik_y \\ k_x + ik_y & 0 \end{pmatrix}$ for the diagonal elements, while the off-diagonal elements depend on τ_z , i.e., $H^{mm+1} = \begin{pmatrix} 0 & A \\ 0 & 0 \end{pmatrix}$, $H^{mm-1} = \begin{pmatrix} 0 & 0 \\ A & 0 \end{pmatrix}$ for K point ($\tau_z = 1$), so that we have

where $k \equiv k_x - ik_y$, $\bar{k} \equiv k_x + ik_y$. For K' point ($\tau_z = -1$), on the other hand, $H^{mm+1} = \begin{pmatrix} 0 & 0 \\ -A & 0 \end{pmatrix}$, $H^{mm-1} = \begin{pmatrix} 0 & -A \\ 0 & 0 \end{pmatrix}$.

When an ac field (such as laser) is applied to the Dirac system, we have thus a series of Floquet branches replicated from the original Dirac bands. This is just a two-band version of the Floquet bands, but a unique and essential effect of the circularly-polarised light is that this turns the system into a topological system, just as in QHE, where the topological nature is characterised by Chern number. Consequently, a topological gap opens at every $\varepsilon = \text{integer} \times (\Omega/2)$ in the quasi-energy band structure (Fig. 57(d)), as also seen in the density of states in Fig. 57(e). The gap at $\varepsilon = \pm\Omega/2$ is the largest, which is related to one-photon assisted transport and exists also in a linearly-polarised light. More importantly, the circularly-polarised

$$H^K = \begin{bmatrix} \ddots & & & & & & \\ & \ddots & & & & & \\ & & \begin{array}{c|c|c|c|c} m=+1 & 0 & -1 & & \\ \hline \Omega & k & 0 & A & 0 & 0 \\ \hline \bar{k} & \Omega & 0 & 0 & 0 & 0 \\ \hline 0 & 0 & 0 & k & 0 & A \\ \hline A & 0 & \bar{k} & 0 & 0 & 0 \\ \hline 0 & 0 & 0 & 0 & -\Omega & k \\ \hline 0 & 0 & A & 0 & \bar{k} & -\Omega \\ \hline & & & & & \ddots \\ & & & & & \ddots \end{array} & & & & \end{bmatrix}$$

case has a gap opening right at the Dirac point, $\mathbf{k} = 0$, $\varepsilon = 0$. The quasi-energy around the point is $\varepsilon_\alpha = \tilde{\varepsilon}_i + m\Omega$ with $\tilde{\varepsilon}_1 = (\sqrt{4A^2 + \Omega^2} + \Omega)/2$, $\tilde{\varepsilon}_2 = (-\sqrt{4A^2 + \Omega^2} + \Omega)/2$. Here we label the states with $\alpha = (i, m)$, where i is the original band index while m the Floquet index. The $\alpha = (1, -1)$, $(2, 0)$ bands are descendants of the original Dirac bands, and the dynamical gap 2κ between them is

$$2\kappa = \sqrt{4A^2 + \Omega^2} - \Omega. \quad (64)$$

The dynamical gap first grows quadratically with A like $2\kappa \sim 2A^2/\Omega$, followed by an asymptote $2\kappa \sim 2A - \Omega$.

To be precise, the quasi-energy is a sum of the dynamical phase and the Aharonov-Anandan (AA) phase (a nonadiabatic extension of Berry's phase)[103] as

$$\varepsilon_\alpha = \langle\langle \Phi_\alpha | H(t) | \Phi_\alpha \rangle\rangle + \gamma_\alpha^{\text{AA}}/T, \quad (65)$$

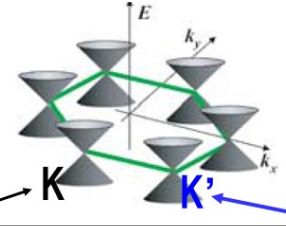
where the AA phase is given by $\gamma_\alpha^{\text{AA}} \equiv T \langle\langle \Phi_\alpha | i\partial_t | \Phi_\alpha \rangle\rangle = \pm\pi \{ [4(A/\Omega)^2 + 1]^{-1/2} - 1 \}$. In Berry's curvature for the Floquet state in Fig. 57(b), we can see a conspicuous peak at $\mathbf{k} = 0$,

$$[\nabla_{\mathbf{k}} \times \mathcal{A}_\alpha(\mathbf{k})]_z \sim \pm \frac{1}{2} \kappa (k^2 + \kappa^2)^{-3/2}, \quad (66)$$

where \pm corresponds to $\alpha = (1, m), (2, m)$.

Now, in graphene we have two valleys, K (with $\tau_z = +1$) and K' ($\tau_z = -1$), and we can show that both valleys contribute to the FTI Hall conductivity with the same sign and add up, i.e., τ_z does not appear in the Berry's curvature in the above expression. The reason for this is that, if we look at the structure of the Hamiltonian for each of the two valleys as in Fig.55, the vector potential representing the circularly-polarised light enters into the expression in such a way that the chirality does not affect the Chern density.

You might have wondered: why an ac field (laser) can produce a dc response (dc Hall current)? This is exactly due to the geometric phase: the ac field changes the system into a Chern insulator, which naturally accommodates the Hall current (\propto Chern number), despite the absence of static external magnetic field. Indeed, right after the proposal by Oka and Aoki,[97]



$H^K = v(\sigma_x k_x + \sigma_y k_y)$ $= v \begin{pmatrix} 0 & (k_x - ik_y) \\ (k_x + ik_y) & 0 \end{pmatrix}$	$H^{K'} = v(-\sigma_x k_x + \sigma_y k_y)$ $= v \begin{pmatrix} 0 & -(k_x + ik_y) \\ -(k_x - ik_y) & 0 \end{pmatrix}$
$\Downarrow \mathbf{k} \rightarrow (\mathbf{k} + e\mathbf{A}_{ac}),$ for a right CPL $\mathbf{A}_{ac} = A_R(\mathbf{x} + i\mathbf{y}) + \text{hc}$	
$H^{K/v} =$ $\begin{bmatrix} 0 & (k_x - ik_y) + 2eA_R \\ (k_x + ik_y) + 2eA_R^\dagger & 0 \end{bmatrix}$	$H^{K'/v} =$ $\begin{bmatrix} 0 & -(k_x + ik_y) - 2eA_R^\dagger \\ -(k_x - ik_y) - 2eA_R & 0 \end{bmatrix}$

Figure 55: For each of the valley K and valley K' , we write down the Hamiltonian in 2×2 forms. When a circularly-polarised light is illuminated, we replace the momentum as $\mathbf{k} \rightarrow (\mathbf{k} + e\mathbf{A}_{ac})$, where $\mathbf{A}_{ac} = A_R(\mathbf{x} + i\mathbf{y}) + \text{h.c.}$ (for a right polarisation here). We can show that H^K and $H^{K'}$ give the same Chern density.

Kitagawa et al[104] have shown that the effective Floquet Hamiltonian for the honeycomb lattice in a circularly-polarised light is, to the leading (second) order in the high-frequency ($1/\Omega$) expansion, is exactly coincides with Haldane's celebrated model[105] for the anomalous QHE (i.e., QHE in zero external magnetic field), as shown in Fig.56. The second-order processes correspond to the photon absorption/emission twice between the original Dirac band and the first ($n = \pm 1$) Floquet bands. Thus the FTI shares Class A (unitary) in Fig.1 with QHE and AQHE. The emergence of the Floquet topological insulator explained above is summarised in Fig.57. If we change the right-circularly polarisation into the left-circularly polarisation, the Hall response changes sign.

The topological phases naturally depend strongly on the frequency and intensity of applied laser field. For the honeycomb lattice driven by circularly-polarised light, Fig.58 is a theoretical result for the Chern numbers against the frequency ω and the amplitude A of the laser.[106] Various values of the topological number appear, with the phase diagram becoming more intricate as ω is decreased, where many Floquet subbands become superposed with band anticrossing.

Since the FTI is a non-equilibrium state, we have to take care of the non-equilibrium (i.e., non-thermal) distributions which differ from the equilibrium Fermi-Dirac distribution. Then the FTI Hall conductivity is somewhat blurred from the QHE quantised values. This depends on the situation: whether (i) the system is isolated (as in cold-atom systems), in which case the Hall conductance significantly deviates from the quantised values, or (ii) the system is coupled

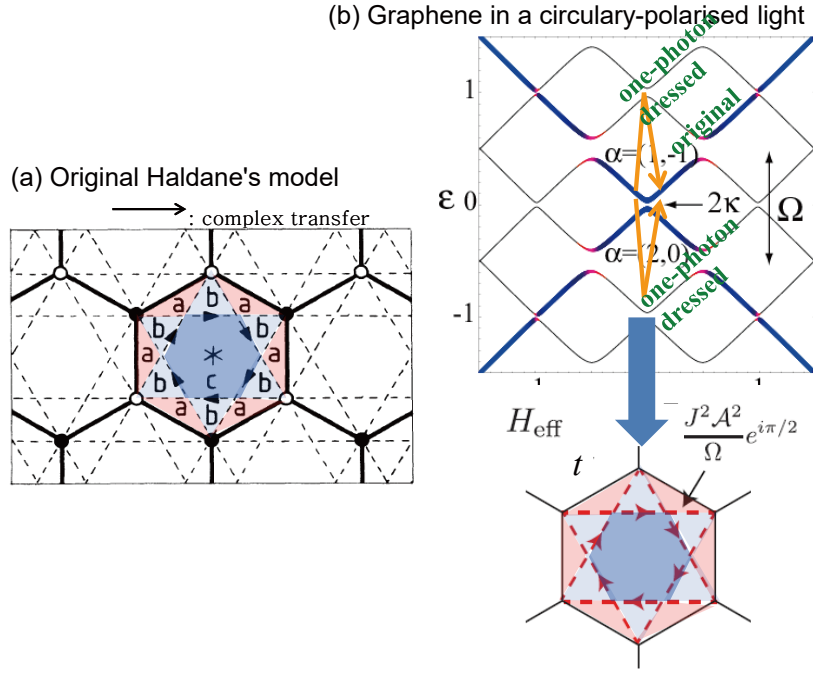


Figure 56: (a) The original Haldane’s model for the anomalous QHE. Dashed lines represent second-neighbour complex hopping (with a positive phase along the arrow, negative in the opposite direction). This may be viewed as coming from magnetic flux penetrating the unit hexagon directed out of the plane (in the portions of the hexagon marked in red) or into the plane (blue), with the total magnetic flux being zero. (b) Graphene in a circularly-polarised light has a series of Floquet subbands comprising Dirac cones separated by the laser frequency Ω . From the second-order processes between the original band and the one-photon dressed bands (double orange arrows) emerge the effective Floquet Hamiltonian that exactly coincides with the Haldane’s model.

to a reservoir (in usual solid-state systems), in which case the Hall conductance is (a) closer to the quantised values for the driving frequency $\Omega \gg W$ with W being the electronic band width, or (b) rather deviates for $\Omega \sim W$, where the situation is determined by the competition between the reservoir-induced cooling and the photocarrier excitations.[102]

Experimentally, the detection of the Floquet topological insulator was first observed on the surface of a 3D topological insulator (Bi_2Se_3) by Gedik’s group.[107] The 3D topological insulator has a topological surface (2D) state that has a Dirac dispersion. When they have looked at the bulk energy spectrum with ARPES, the gap opening is observed when a circularly-polarised light is illuminated on the surface. Time evolution of the gaps were even observed with time-resolved ARPES. The next detection of FTI came from photonics, which has an interesting analogy with electronic systems. Namely, Rechtsman’s group[108] has constructed a honeycomb array of spiral photonic guides, where they succeeded in observing a photonic analogy of the Floquet topological insulator. There, the drive by an external circularly-polarised light is mimicked by the spiral structure, and the topological nature of the resulting photonic state is

confirmed by detecting topological photonic edge states. The third experimental observation of FTI was done in the cold-atom physics.[109] Namely, Esslinger's group in ETH Zürich has used a cold-atom system on a honeycomb optical lattice, which was shaken in a circular motion. The topological state was detected as a Hall drift of the cold atom system, and they have even obtained the AQHE phase diagram of the Haldane's model by tuning the phase dominating the Hamiltonian with linear \leftrightarrow circular motions.

Finally came an experimental realisation[110] of the FTI in graphene itself, which the original theoretical proposal [97] had in mind. McIver and coworkers in MPI Hamburg had an experimental setup for graphene, where a graphene sample with four terminals is optically driven by an ultrafast mid-infrared circularly polarised laser in femtosecond pulse forms. The excited Hall current (perpendicular to an applied electric field in the four-terminal) is then led via a microstrip transmission line to a photoconductive switch for current detection. The obtained result shows a clear plateau structure in the Hall conductivity and associated gap openings.

Thus, for the quantum Hall effects, we have now three examples: (i) the original QHE system, (ii) the spin Hall effect in topological insulators for a Dirac system with a spin-orbit coupling,[59] and (iii) the Floquet topological insulator (Fig.59).

Talking of the photonic FTI, there is an entirely different avenue for electromagnetic waves for QHE-like states. This was initiated theoretically by Haldane and coworkers,[111] which was subsequently confirmed experimentally by Wang and coworkers.[112] A photonic analogue of quantum spin-Hall effect (QSHE) has also been explored in photonic crystals. By manipulating honeycomb photonic crystals, it is possible to have a photonic Hamiltonian from the $k \cdot p$ formalism in an appropriate photonic basis, which has the same form as the HgTe quantum wells which is the birth place of QSHE.[60]

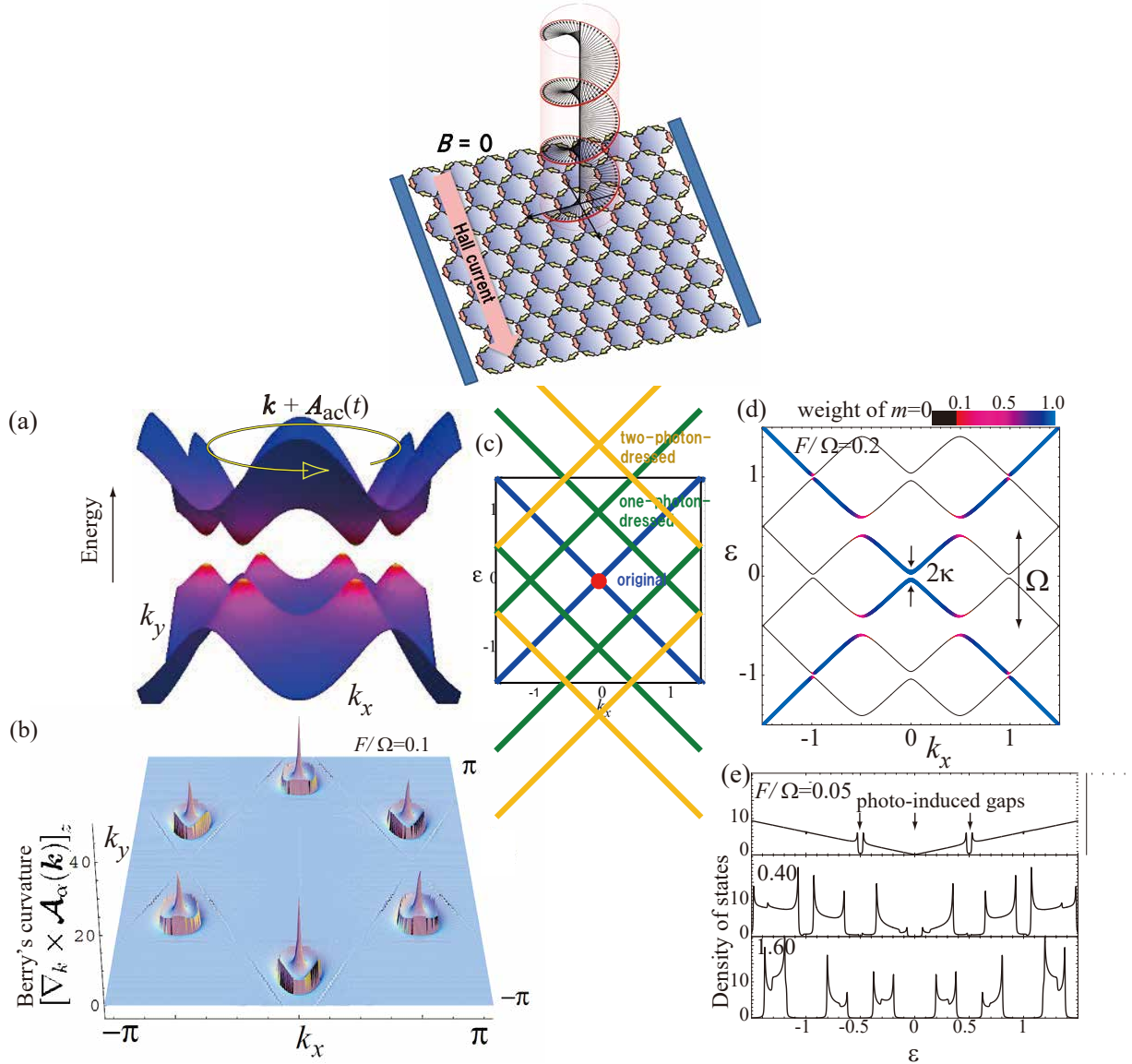


Figure 57: Top inset: Floquet topological insulator, which arises when graphene is illuminated by a circularly-polarised laser is schematically shown. Blue bars stand for electrodes for Hall effect measurement. (a) Band dispersion, with topological gaps arising, when each electron's momentum follows a trajectory $\mathbf{k} + \mathbf{A}_{ac}(t)$ in a circularly-polarised light is schematically shown. (b) The photo-induced Berry's curvature $[\nabla_{\mathbf{k}} \times \mathcal{A}_{\alpha}(\mathbf{k})]_z$ for $\alpha = (1, m)$ for $F/\Omega = 0.2$, $\Omega/v = 1$. (c) A series of Floquet subbands generated from the original Dirac cone is schematically shown against k_x (measured from each Dirac point), for which level anticrossing will give the next panel. (d) The Floquet quasi-energy (black curves) plotted against k_x with $k_y = 0$ for $F/\Omega = 0.2$. The colour coding represents the weight of the static ($m = 0$) component. (e) Density of states for various field strengths F . After T. Oka and H. Aoki, Phys. Rev. B **79**, 081406(R) (2009).

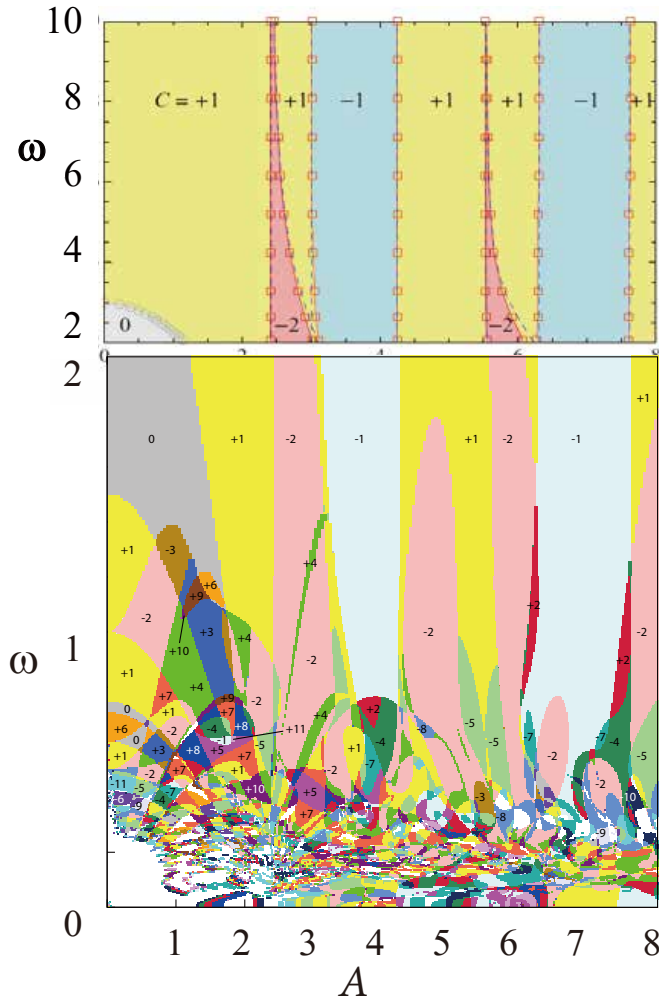


Figure 58: Topological phase diagram against the frequency ω and the amplitude A of the laser for a honeycomb lattice illuminated by a circularly-polarised laser. Top (bottom) panel is for $\omega > 2$ ($\omega < 2$). After T. Mikami et al, Phys. Rev. B **93**, 144307 (2016).

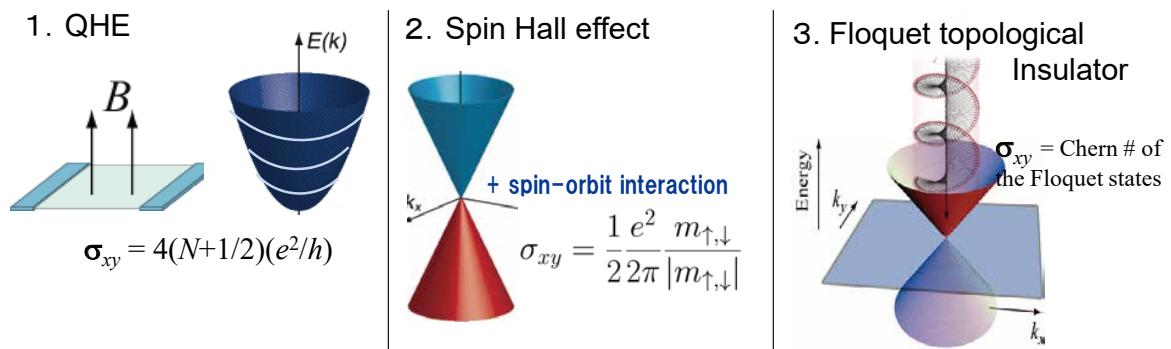


Figure 59: Three examples of quantum Hall effects: (Left) the original QHE system, (middle) the spin Hall effect in topological insulators for a Dirac system with a spin-orbit coupling, and (right) the Floquet topological insulator.

14 Summary

To summarise the chapter, we have surveyed the quantum Hall effect, primarily in a perspective of topological systems. So we have started from the classification of topological systems by generic symmetries to show a rich variety of topological systems which were kicked off by the integer quantum Hall effect. Then we have surveyed theoretical reasoning and various experimental results. Due to the bulk-edge correspondence for topological systems, edge states are among the essential feature in QHE. We then looked at how QHE contributes not only to the resistance standard, but to the determination of the fine-structure constant and definition of the new SI. We have also looked into QHE in periodic systems with fractal energy spectra and QHE in three dimensions. Then we delve into the anomalous quantum Hall effect and spin quantum Hall effect as relatives of the IQHE, and also touched upon integer vs fractional quantum Hall effects. Then we elaborated QHE in graphene as a novel arena, both for monolayer and bilayer graphenes. We have included optical properties, and an analogy between QHE and superconductivity. For the bilayer graphene, we have explored the twisted bilayer graphene which harbour rich physics. Last but not least, the final section looks into QHE in light-matter coupled systems, where Floquet topological insulator is described both theoretically and experimentally as a prime example of nonequilibrium realisation of topological states.

These perspectives give a widened horizon of the condensed-matter physics, and we can envision further developments into diverse directions.

References

- [1] A.P. Schnyder, S. Ryu, A. Furusaki, and A.W.W. Ludwig, Phys. Rev. B **78**, 195125 (2008); S. Ryu et al, New J. Phys. **12**, 065010 (2010); M.Z. Hasan and C.L. Kane, Rev. of Mod. Phys. **82**, 3045 (2010).
- [2] G. Landwehr, Festkörperprobleme **26** (1986) 17.
- [3] H. Aoki, Rep. Progr. Phys. **50**, 655 (1987).
- [4] T. Chakraborty and P. Pietiläinen: *The Fractional quantum Hall effect* (Springer, 1988).
- [5] R. E. Prange and S. M. Girvin (ed): *The Quantum Hall effect*, 2nd edn (Springer, New York, 1990).
- [6] S. Das Sarma and A. Pinczuk (editors): *Perspective in Quantum Hall Effects* (John Wiley, New York, 1997).
- [7] D. Yoshioka: *The Quantum Hall Effect* (Springer, 2002).
- [8] T. Ando, A. B. Fowler and F. Stern, Rev. Mod. Phys. **54**, 437 (1982).
- [9] T. Ando and Y. Uemura, J. Phys. Soc. Jpn **36**, 959 (1974); T. Ando, *ibid* **36**, 1521 (1974); *ibid* **37**, 1233 (1974); T. Ando, Y. Matsumoto and Y. Uemura, J. Phys. Soc. Jpn **39**, 279 (1975).

- [10] T. Igarashi, J. Wakabayashi and S. Kawaji, J. Phys. Soc. Jpn 38, 1549 (1975); S. Kawaji and J. Wakabayashi, in *Physics in High Magnetic Fields*, ed. by S. Chikazumi and N. Miura (Springer, 1981) p.284; S. Kawaji, Proc. Jpn Acad. B **84**, 199 (2008).
- [11] K. von Klitzing, G. Dorda and M. Pepper, Phys. Rev. Lett. **45**, 494 (1980).
- [12] R. Fletcher, Semicond. Sci. Technol. **14**, R1 (1999).
- [13] A. Tsukazaki et al, Phys. Rev. B **78**, 233308 (2008).
- [14] H. Aoki and T. Ando, Solid State Commun. **38**, 1079 (1981) [reprinted in *ibid* **88**, 951 (1993)].
- [15] H. Aoki and H. Kamimura, Solid State Commun. **21**, 45 (1977); H. Kamimura and H. Aoki: *Physics of Interacting Electrons in Disordered Systems* (Oxford University Press, Oxford, 1989).
- [16] L. D. Landau, E. M. Lifshitz and L. P. Pitaevskii, *Electrodynamics of continuous media* 2nd ed (Pergamon, 1984), section 22.
- [17] P. Středa, J. Phys. C **15**, L718 (1982); A. Widom, Phys. Lett. **90A**, 474 (1982).
- [18] R. B. Laughlin, Phys. Rev. B **23**, 5632 (1981).
- [19] D. J. Thouless, M. Kohmoto, P. Nightingale and M. den Nijs, Phys. Rev. Lett. **49**, 405 (1982).
- [20] H. Aoki and T. Ando, Phys. Rev. Lett. **57**, 3093 (1986). See also Y. Huo and R.N. Bhatt, Phys. Rev. Lett. **68**, 13775 (1992); K. Yang and R.N. Bhatt, Phys. Rev. B **59**, 8144 (1999).
- [21] A.M.M. Pruisken, in R. E. Prange and S. M. Girvin (ed): *The Quantum Hall effect*, 2nd edn (Springer, New York, 1990), p.117.
- [22] For a review, see E. Fradkin: Field Theoretic Aspects of Condensed Matter Physics: An Overview, in T. Chakraborty et al (editors), *Encyclopedia of Condensed Matter Physics*, 2nd edition (Elsevier, 2023).
- [23] H. Aoki and T. Ando, Phys. Rev. Lett. **54**, 831 (1985); T. Ando and H. Aoki, J. Phys. Soc. Jpn **54**, 2238 (1985).
- [24] J.T. Chalker and P.D. Coddington, J. Phys. C **21**, 2665 (1988).
- [25] B. Kramer, T. Ohtsuki and S. Kettmann, Phys. Rep. **417**, 211 (2005).
- [26] B. Huckestein, Rev. Mod. Phys. **67**, 357 (1995).
- [27] S. Kivelson et al, Phys. Rev. B **46**, 2223 (1992).
- [28] H. Aoki, J. Phys. C **16**, L205 (1983).
- [29] T. Terao, T. Nakayama and H. Aoki, Phys. Rev. B **54**, 10350 (1996).

- [30] T. Morimoto, Y. Avishai and H. Aoki, Phys. Rev. B **82**, 081404(R) (2010)].
- [31] B. I. Halperin, Phys. Rev. B **25**, 2185 (1982).
- [32] Y. Hatsugai, J. Phys.: Condens. Matter **9**, 2507 (1997); Y. Hatsugai: Bulk-Edge Correspondence, in T. Chakraborty et al (editors), *Encyclopedia of Condensed Matter Physics*, 2nd edition (Elsevier, 2023).
- [33] M. Koshino et al, Phys. Rev. Lett. **86**, 1062 (2001); Phys. Rev. B **65**, 045310 (2002); Phys. Rev. B **66**, 081301(R) (2002).
- [34] M. Büttiker, in *Nanostructured systems*, ed. by M. Reed (Academic Press, New York, 1992), p.191.
- [35] P.F. Fontein, et al, Phys. Rev. B **43**, 12090 (1991).
- [36] R. Knott et al, Semicond. Sci. Tech. **10**, 117 (1995).
- [37] M. Morgenstern, in *Scanning Probe Microscopy*, edited by S. Kalinin and A. Gruwermann (Springer, New York, 2007).
- [38] Y.Y. Wei, et al, Phys. Rev. Lett. **81**, 1674 (1998).
- [39] K. Lai, et al, Phys. Rev. Lett. **107**, 176809 (2011).
- [40] K. Ikushima et al, Phys. Rev. Lett. **93**, 146804 (2004).
- [41] K. Hashimoto et al, Phys. Rev. Lett. **101**, 256802 (2008).
- [42] T. Kinoshita, Prog. theoret. phys. suppl. **167**, 62 (2007).
- [43] P. J. Mohr, B. N. Taylor and D. B. Newell, Rev. Mod. Phys. **80**, 633 (2008).
- [44] G. Nachtwei, Physica E **4**, 79 (1999).
- [45] R.G. Mani et al, Nature **420**, 646 (2002). See also A.V. Andreev et al, Phys. Rev. Lett. **91**, 056803 (2003).
- [46] P. A. Maksym et al, J. Phys.: Condens. Matter **12**, R299 (2000).
- [47] G.H. Wannier, Rev. Mod. Phys. **34**, 645 (1962); D. R. Hofstadter, Phys. Rev. B **14**, 2239 (1976).
- [48] M. C. Geisler et al, Phys. Rev. Lett. **92**, 256801 (2004).
- [49] M. Aidelsburger et al, Phys. Rev. Lett. **111**, 185301 (2013).
- [50] H. Miyake et al, Phys. Rev. Lett. **111**, 185302 (2013).
- [51] N. Goldman, J. Beugnon, and F. Gerbier, Phys. Rev. Lett. **108**, 255303 (2012).
- [52] C.R. Dean et al, Nature **497**, 598 (2013).

- [53] X. Lu et al, Proc. Nat. Academy Sci. **118**, e2100006118 (2021).
- [54] J.E. Avron, R. Seiler, and B. Simon, Phys. Rev. Lett. **51**, 51 (1983); B.I. Halperin, Jpn. J. Appl. Phys. Suppl. **26**, 1913 (1987).
- [55] M. Koshino et al, Phys. Rev. Lett. **86**, 1062 (2001); Phys. Rev. B **65**, 045310 (2002); Phys. Rev. B **67**, 195336 (2003).
- [56] M. Koshino et al, Phys. Rev. B **65**, 205311 (2002) and refs therein.
- [57] M. König, H. Buhmann, L. W. Molenkamp, T. Hughes, C.-X. Liu, X.-L. Qi and S.-C. Zhang, J. Phys. Soc. Jpn **77**, 031007 (2008) .
- [58] S. Murakami, Prog. Theor. Phys. Suppl. **176**, 279 (2008).
- [59] C. L. Kane and E. J. Mele, Phys. Rev. Lett. **95**, 226801 (2005).
- [60] B.A. Bernevig et al, Phys. Rev. Lett. **96**, 106802 (2006); Science **314**, 1757 (2006); M. König et al, Science **318**, 766 (2007).
- [61] W. Pan et al, Phys. Rev. Lett. **88**, 176802 (2002).
- [62] S. Kivelson, D-H Lee and S-C Zhang, Phys. Rev. B **46**, 2223 (1992).
- [63] K. S. Novoselov et al, Nature **438**, 197 (2005).
- [64] A. K. Geim and K. S. Novoselof, Nature Materials **6**, 183 (2007).
- [65] A. H. Castro Neto et al, Rev. Mod. Phys. **81**, 109 (2009).
- [66] Y. Hatsugai and H. Aoki in H. Aoki and M.S. Dresselhaus (eds.): *Physics of Graphene* (Springer, 2014), Ch.7, pp. 213-250.
- [67] A. H. MacDonald, Phys. Rev. B **28**, 2235 (1983).
- [68] Y. Zheng and T. Ando, Phys. Rev. B **65**, 245420 (2002).
- [69] V. P. Gusynin and S. Sharapov, Phys. Rev. Lett. **95**, 146801 (2005).
- [70] Y. Hatsugai et al, Phys. Rev. B **74**, 205414 (2006).
- [71] T. Kawarabayashi et al, Phys. Rev. B **83**, 153414 (2011); Phys. Rev. Lett. **103**, 156804 (2009).
- [72] N. Tajima et al, J. Phys. Soc. Jpn. **75**, 051010 (2006); Phys. Rev. Lett. **102**, 176403 (2009); Phys. Rev. B **88**, 075315 (2013).
- [73] H. Aoki, Appl. Phys. Lett. **48**, 559 (1986).
- [74] T. Morimoto et al, Phys. Rev. B **78**, 073406 (2008).

- [75] F. Wendler and E. Malic, *Sci. Rep.* **5**, 12646 (2015); M. Mittendorff et al, *Nature Phys.* **11**, 75 (2015); C. Faugeras, M. Orlita and M. Potemski, *J. Raman Spectroscopy* **49**, 146 (2018); B. Benhamou-Bui et al, *APL Photon.* **8**, 116106 (2023); M.O. Goerbig, arXiv:2307.05116.
- [76] M. Orlita et al, *Nature Phys.* **10**, 233 (2014).
- [77] T. Morimoto, Y. Hatsugai, and H. Aoki, *Phys. Rev. Lett.* **103**, 116803 (2009).
- [78] Y. Ikebe et al, *Phys. Rev. Lett.* **104**, 256802 (2010).
- [79] R. Shimano et al, *Nature Commun.* **4**, 1841 (2013).
- [80] S. Kitamura and H. Aoki, *Commun. Phys.* **5**, 174 (2022).
- [81] E. McCann and V.I. Falco, *Phys. Rev. Lett.* **96**, 086805 (2006).
- [82] Y. Cao et al, *Nature* **556**, 43 (2018).
- [83] M. Koshino et al, *Phys. Rev. X* **8**, 031087 (2018).
- [84] H.C. Po et al, *Phys Rev. B* **99**, 195455 (2019).
- [85] Y. Cao et al, *Nature* **556**, 80 (2018).
- [86] P. Moon and M. Koshino, *Phys. Rev. B* **85**, 195458 (2012).
- [87] H. Aoki, M. Ando and H. Matsumura, *Phys. Rev. B* **54**, R17296 (1996).
- [88] X. Lu et al, *Nature* **574**, 653 (2019).
- [89] A. Uri et al, *Nature* **581**, 47 (2020).
- [90] For reviews of bilayer graphene, see e.g. E.Y. Andrei and A.H. MacDonald, *Nature Mat.* **19**, 1265 (2020).
- [91] Y. Ito et al, *Phys. Chem. Chem. Phys.* **20**, 6024 (2018).
- [92] M. Koshino and H. Aoki, *Phys. Rev. B* **93**, 041412(R) (2016).
- [93] A. Uri et al, *Nature Phys.* **16**, 164 (2020).
- [94] P. Středa, *Phys. Rev. B* **74**, 113306 (2006); P. Středa et al, *Phys. Rev. B* **76**, 085310 (2007); *Phys. Rev. Lett.* **100**, 146804 (2008).
- [95] H. Aoki and Y. Hatsugai, *Phys. Rev. B* **90**, 045206 (2014).
- [96] R.D. King-Smith and D. Vanderbilt, *Phys. Rev. B* **47**, 1651 (1993); R. Resta, *Rev. Mod. Phys.* **66**, 899 (1994).
- [97] T. Oka and H. Aoki, *Phys. Rev. B* **79**, 081406(R) (2009) [erratum: *Phys. Rev. B* **79**, 169901(E) (2009)].

- [98] H. Aoki et al, Rev. Mod. Phys. **86**, 779 (2014).
- [99] G. Floquet, Ann. Sci. Ec. Normale Super. **12**, 47 (1883).
- [100] G.W. Hill, Acta Math. **8**, 1 (1886).
- [101] T. Oka and H. Aoki, J. Phys.: Conf. Ser. **334**, 012060 (2011).
- [102] H. Dehghani, T. Oka, and A. Mitra, Phys. Rev. B **91**, 155422 (2015).
- [103] Y. Aharonov and J. Anandan, Phys. Rev. Lett. **58**, 1593 (1987).
- [104] T. Kitagawa et al, Phys. Rev. B **84**, 235108 (2011).
- [105] F.D.M. Haldane, Phys. Rev. Lett. **61**, 2015 (1988).
- [106] T. Mikami et al, Phys. Rev. B **93**, 144307 (2016).
- [107] Y. H. Wang, H. Steinberg, P. Jarillo-Herrero, and N. Gedik, Science **342**, 453 (2013); see also F. Mahmood et al, Nature Phys. **12**, 306 (2016).
- [108] M.C. Rechtsman et al, Nature **496**, 196 (2013); see also J. Guglielmon et al, Phys. Rev. A **97**, 031801(R) (2018); T. Ozawa et al, Rev. Mod. Phys. **91**, 015006 (2019).
- [109] G. Jotzu et al, Nature **515**, 237 (2014).
- [110] J. W. McIver et al, Nature Phys. **16**, 38 (2020).
- [111] F.D.M. Haldane and S. Raghu, Phys. Rev. Lett. **100**, 013904 (2008); S. Raghu and F.D.M. Haldane, Phys. Rev. A **78**, 033834 (2008).
- [112] Z. Wang et al, Nature **461**, 772 (2009).

Further Reading

- Aoki H (1987) Reports on Progress in Physics 50: 655.
- Aoki H and Dresselhaus MS (eds.) (2014): *Physics of Graphene*. Springer.
- Chakraborty T and Pietiläinen P (1988) The Fractional Quantum Hall Effect. Springer.
- Das Sarma S and Pinczuk A (eds.) (1997) Perspective in Quantum Hall Effects. New York: Wiley.
- Zyuan Francis Ezawa (2013): *Quantum Hall Effects* 3rd Ed. World Scientific.
- Landwehr G (1986) Festkörperprobleme 26: 17.
- Prange RE and Girvin SM (eds.) (1990) The Quantum Hall Effect, 2nd edn. New York: Springer.
- Yoshioka D (2002) The Quantum Hall Effect. Springer.